STUDIES ON THE FLUID MECHANICS AND MASS TRANSFER IN NEURAL DRUG DELIVERY

A Dissertation

Presented to the Faculty of the Graduate School

of Cornell University

In Partial Fulfillment of the Requirements for the Degree of

Doctor of Philosophy

by

Peng Wang

May 2011

STUDIES ON THE FLUID MECHANICS AND MASS TRANSFER IN NEURAL DRUG DELIVERY

Peng Wang, Ph. D.

Cornell University 2011

There are many promising treatments for neurological disorders. The work in this dissertation is aimed at addressing some of the issues associated with delivery of drugs to the brain. A major focus of this work is the study of transport phenomena of therapeutic agents through neural tissues. First, we carry out a theoretical analysis to investigate the fluid mechanics in the perivascular space (PVS). Our calculations indicate that peristaltic motion of the blood vessel walls can facilitate fluid and solute transport in the PVS. We then consider the impact of ultrasound exposure on neural drug delivery. We find that under certain conditions two acoustic waves can coexist and one of them has an extremely large penetration depth. We make a third analysis on the retro-convection-enhanced drug delivery (R-CED). The model is used to predict the pressure distribution, the fluid flow pattern, and the drug concentration profile in R-CED. The effectiveness of R-CED to achieve a large treatment volume is called into question. We make a fourth analysis to describe nanoparticle transport in the brain. We explicitly take the hydrodynamic interactions between the nanoparticles, the carrying fluid, and the brain tissue into account. We devote the fifth analysis to the solid mechanics involved in cerebral microhemorrhage. The steady-state and the time-dependent behaviors of the displacement vectors are examined. Then, we describe the design and fabrication of a microfluidic probe with a capacitive pressure sensor integrated at its tip. Such a device should be able to monitor the tip

pressure in convection-enhanced drug delivery (CED) and serve as an indicator of the onset of serious backflow problems or other failures. Finally, we present the fabrication and characterization of a micromachined dissolved oxygen sensor based on solid polymer electrolyte. The small size of the whole device and the simplicity of the fabrication process make these devices promising for medical uses. Single devices are shown to have decent performances in terms of long term stability, reliability, hysteresis, linearity, and sensitivity. Variations among different devices are characterized and correlated and methods for reducing such variations are proposed.

BIOGRAPHICAL SKETCH

Peng Wang was born and raised in the city of Tianjin, China. After finishing high school education, he was luck to get the opportunity to enter Tsinghua University, China, in 2002. There he was introduced to the field of chemical engineering and became interested and animated in the subject. In 2006, he received his Bachelor's degree and chose Cornell University to pursue a PhD degree in chemical engineering. Over the years, he worked hard and was able to make original contributions to the field under the guidance of his advisor Bill Olbricht.

ACKNOWLEDGMENTS

I am grateful for having the opportunity to study under the guidance of three excellent advisors - Bill Olbricht, Chris Schaffer, and Abraham Stroock. Former research group members Keith Neeves and Conor Foley were my great mentors and friends. During the time when I was a novice in the lab, they were extremely patient to answer a great deal of stupid questions. George Lewis has become my good friend since our first collaboration on the study of ultrasound-assisted neural drug delivery. My Chinese friend Zichao Yang always helps me without any hesitation when I am in trouble. Nathanael Rosidi is a wonderful collaborator. Prof. Daniel is very generous to give me a spot in the office of her research group. And there I got to know one of my best friends – Sudhir Prabhu. Finally, I am always indebted to my beloved parents. Thank you, all.

Portions of this work were carried out at the Cornell NanoScale Facility, a member of the National Nanotechnology Infrastructure Network, which is supported by the National Science Foundation (Grant ECS-0335765).

TABLE OF CONTENTS

LIST OF FIGURES

LIST OF TABLES

CHAPTER 1

INTRODUCTION

Neural drug delivery has been an intensive topic of research in recent years due to its importance in clinical medicine. Many promising treatments for brain diseases exist, but the efficacies of these therapies are often limited by the difficulty of delivering drugs to the afflicted area in the brain due to the presence of the blood brain barrier (BBB). The BBB is a separation between the circulating blood and the brain extracellular matrix. Tight junctions formed between endothelial cells prevent systemically administered drugs from going across the blood vessel walls and entering the brain extracellular space. One of the solutions toward better therapeutic strategies is to gain deeper understandings of the transport phenomena occurring in the brain. The work presented in this dissertation is mainly concerned with the fluid mechanics and mass transfer issues involved in brain drug delivery.

Chapter 2 of this dissertation deals with the fluid mechanics in the perivascular space (PVS). PVS within the brain is an important pathway for interstitial fluid (ISF) and solute transport. Fluid flows in the PVS can affect these transport processes and have significant impacts on physiology. We carry out a theoretical analysis to investigate the fluid flows in the PVS. With certain assumptions and approximations, we are able to find an analytical solution to the problem. We discuss the physical meanings of the solution and particularly examine the consequences of the induced fluid flow in the context of convection-enhanced delivery (CED). We conclude that peristaltic motions of the blood vessel walls can facilitate fluid and solute transport in the PVS.

In chapter 3, we carry out a theoretical analysis on ultrasound assisted brain drug

delivery. The brain tissue is modeled as a fluid-saturated poroelastic medium. Using a perturbation approach, we are able to linearize the governing equations and obtain an analytical solution. Low-power ultrasound propagates in the medium as mechanical waves, but dissipates due to the frictional forces between the fluid phase and the solid phase. The important variables regarding to drug delivery are the penetration depth and the amplitude of the ultrasound. The dependencies of these two variables on tissue properties and operating conditions (e.g. frequency, power) are discussed in detail. We have two major findings. The first is that low-power ultrasound can enhance drug penetration into the brain tissue by inducing local fluid mixing. The second is that under certain conditions two acoustic waves can coexist and one of them has an extremely large penetration depth.

In chapter 4, we carry out a theoretical analysis on retro-convection-enhanced drug delivery (R-CED). R-CED is an emerging technique to overcome the blood brain barrier (BBB). It creates a pressure difference between the blood stream and the extracellular fluid by withdrawing fluid out of the brain. This pressure difference generates a convective flow across the blood vessel wall and partially opens the BBB. In this chapter, we develope a mathematical model to understand the fluid mechanics and mass transfer in the interstitium of brain tissue involved in R-CED. Analytical and numerical solutions are obtained. The model is used to predict the pressure distribution, the fluid flow pattern, and the drug concentration profile. Three kinds of microdialysis membranes used in R-CED protocols are analyzed in detail. While fluid flow is found to be independent of the choice of membranes, mass transfer is found to be highly dependent on the choice of membranes. Sensitivity analysis over a wide range of parameter values is carried out. Although R-CED is efficacious in generating fluid flows in the brain tissue, it seems that it does not lead to a large treatment volume and needs to be re-examined and re-evaluated experimentally.

In chapter 5, we carry out a theoretical analysis on nanoparticle transport in the brain. The convection-enhanced distribution of small molecules in the brain is relatively well-understood from previous studies. The given assumption is that the hydrodynamic interactions between the small molecules and the carrying fluid are negligible. However, this assumption is no longer valid when applied to nanoparticles. Previous CED experiments have shown that the distribution and transport of nanoparicles in the brain is different from small molecules. In this chapter, we present a simple mathematical model to describe the transport behavior of nanoparticles in CED. This model explicitly takes the hydrodynamic interactions between the nanoparticles, the carrying fluid, and the brain tissue into account. Using this model, we are able to show how the volume of distribution is dependent on the sizes and the surface properties of the infused nanoparticles. In particular, the volume of distribution is sensitive on the surface properties of these nanoparticles.

Chapter 6 addresses a different issue with the brain. It deals with cerebral microhemorrhage. There are few effective treatments or preventative strategies for hemorrhagic microvascular lesions. Clinical evidence has revealed that microhemorrhage plays an important role in several brain dysfunctions such as elderly dementia. The lack of good animal models has greatly impeded our understanding on this subject. However, advances in modern optical techniques have allowed researchers to induce single-vessel hemorrhages in the cortex of rodents. Observations from these animal models provide us with an excellent opportunity to study the progression of hemorrhage related diseases and evaluate the effectiveness of potential therapeutics. In this chapter, we present mathematical models, derived from both fundamental considerations and empirical correlations, to describe the statics and the dynamics in cerebral microhemorrhage and compare the models with the experimental data.

In chapter 7, we describe the design and fabrication of a microfluidic probe with an

integrated capacitive pressure sensor. Several researchers have created microfluidic probes for use in CED. These devices can reduce backflow and minimize the initial tissue damage due to insertion. An integrated pressure sensor at the probe tip will be beneficial if it can be added by microfabrication techniques because pressure drops are often good indicators of the onset of serious backflow problems or other failures. Such a device should be able to monitor the tip pressure rather than an upstream pressure because, more often than not, it is desirable that the pressure reading only reflects flow through the tissue rather than flow through the syringe, needle, and tissue. Detailed designs and fabrication processes are presented in this chapter. The difficulties and problems encountered in the actual fabrication trials are also analyzed.

In the last chapter, we describe the fabrication and characterization of silicon microprobes to measure dissolved oxygen levels. The sensors are prepared by overlaying platinum thin film electrodes with a solid state proton conductive matrix (PCM) coating. The platinum thin film electrodes are fabricated on silicon substrates by standard photolithographic techniques while the PCM coating is achieved by drop-casting methods. The size and materials of the device make it potentially suitable for medical implantation. The devices are tested in deionized water (DI water), phosphate buffered saline (PBS), and bovine blood serum (BBS). Through linear sweep voltammetry (LSV), single devices are shown to have decent performances in terms of long term stability, reliability, hysteresis, linearity, and sensitivity. Variations among different devices are characterized and correlated. The simplicity and cost effectiveness of the fabrication and packaging procedures and the decent in vitro performances of these devices make them good candidates as miniaturized, disposable, and implantable dissolved oxygen sensors for biological and biomedical use.

CHAPTER 2

FLUID MECHANICS IN THE PERIVASCULAR SPACE

2.1 Introduction

Many promising therapeutic compounds for the treatment of neural disorders do not readily cross the blood-brain barrier when they are administered systemically. As a result, some alternative methods have been developed to deliver compounds locally to neural tissue. Convection-enhanced delivery (CED) is a novel method for in which compounds are infused directly into the brain parenchyma through a needle or cannula that is inserted into the brain through a small hole in the skull (Bobo et al., 1994). The infusion establishes a pressure gradient in the tissue, which induces a flow of infused fluid in the radial direction away from the tip of the needle. Convection enhances the transport rate of compounds compared with diffusion, especially near the needle or cannula where convective forces are dominant. A variety of compounds have been delivered using CED in preclinical and clinical studies, including small molecules, chemotherapeutics, proteins, viral vectors, and drug-containing liposomes and other nanoparticles.

The results of studies in animals and humans show that controlling the spatial distribution of infused compounds is a critical challenge in CED. Heterogeneities in neural tissue structures lead to corresponding spatial variations in tissue hydraulic conductivity, which can cause fluid to flow preferentially in certain directions or along certain paths. It has long been known that tracer compounds and other solutes are transported preferentially along perivascular spaces in the cerebral cortex. The perivascular spaces are extensions of the subarachnoid space that resemble

thin annular regions outside blood vessels that penetrate the cortex. The perivascular spaces may serve as preferred conduits for flow of cerebral spinal fluid, and they may provide paths for drainage of excess fluid associated with cerebral edema. During CED therapy, preferential flow of infused fluid along the perivascular spaces could affect the overall spatial distribution of therapeutic compounds and could provide a route for infused compounds to escape the tissue volume targeted for therapy.

The hydraulic conductivity of the perivascular spaces presumably is greater than that of white or gray matter. However, there is evidence that suggests that pulsations of the blood vessel associated with the heartbeat may help propel infused material through the perivascular space. Hadaczek et al (2006) studied the distribution of liposomes infused during CED in rats. When the animal's heart rate and blood pressure were artificially lowered during CED, which presumably lowered the frequency and amplitude of blood vessel pulsations, the volume of distribution of infused liposomes was also reduced. They called the transport enhancement associated with blood vessel pulsation "perivascular pumping."

Fluid flows induced by peristalsis have been extensively studied in the literature. A classical review can be found in Jaffrin and Shapiro (1971). For mathematical tractability and simplicity most researchers have taken the peristaltic waves as an infinite train of sinusoids. When the ratio of the wave amplitude to the mean half-width of the flow channel is assumed to be small, a perturbation analysis can be developed with this ratio as the small parameter, and semi-numerical solutions can be obtained. When the ratio of the wavelength to the half-width of the channel is assumed to be large, lubrication approximations can be applied and analytical solutions can be obtained in some circumstances. Alternatively, computational fluid dynamics can be used to solve directly the Navier-Stokes equations with complex boundary geometry and boundary conditions and with arbitrary peristaltic waveforms (Bilston et al. 2003).

Much of the work in this area has been aimed at understanding biological and physiological processes. For example, Shapiro et al. (1969) applied a model of peristalsis to the ureter and used the model to investigate the physiological implications of reflux and fluid bolus trapping phenomena. Mishra and Rao (2004) modeled fluid flow in the gastrointestinal tract by studying the peristaltic transport in a channel with a porous peripheral layer. Bilston et al. (2003) carried out a detailed numerical analysis of cerebrospinal fluid flow along the PVS in the spinal cord. Schley et al. (2006) constructed a mathematical model to test the hypothesis that perivascular drainage of interstitial fluids and solutes out of the brain tissue was driven by pulsations of blood vessel walls.

In this chapter, we develop a model of fluid flow in the cerebral perivascular space induced by peristaltic motion of the blood vessel walls and show how the peristaltic flow interacts with the local flow associated with a CED infusion. Our goals are to show how various physiological parameters, especially those whose values are uncertain and difficult to estimate, affect fluid transport and to develop a result that could be used to account for perivascular transport in numerical simulations of CED infusions.

2.2 Mathematical Model

The perivascular space (PVS) is modeled as a thin, annular, fluid-filled porous medium surrounding a blood vessel (Figure 2.1). We choose a cylindrical coordinate system such that the z axis is coincident with the blood vessel centerline. To simplify

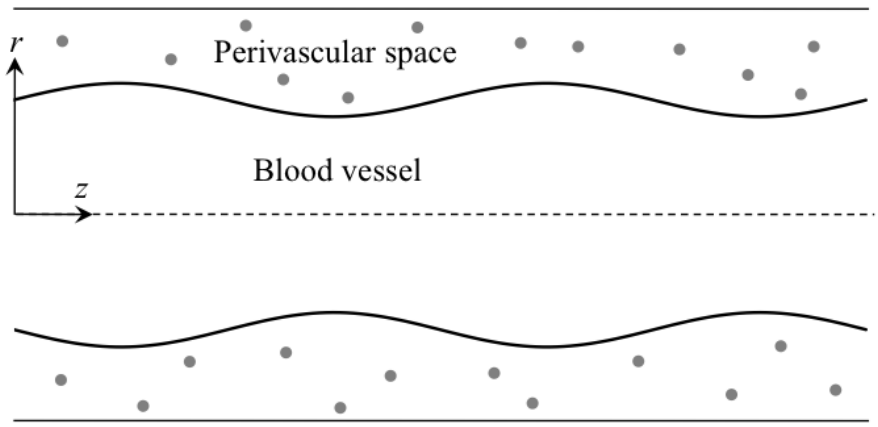

Figure 2.1: Geometry of the problem.

the analysis, we assume that both the inner and outer walls of the PVS are impermeable to fluid. The outer wall of the annulus is fixed at $r = R_2$. The location of the inner wall of the annulus, which corresponds to the blood vessel inner wall, is given by *h(t,z)*, the radial coordinate of the point with an axial coordinate *z* on the inner wall at time *t*. To introduce peristalsis, we assume the blood vessel oscillates according to $h(t,z) = R_1 + b\sin\left(2\pi\left(z - ct\right)/\lambda\right)$, which represents a sinusoidal peristaltic wave with mean radius R_1, half amplitude *b*, wavelength λ, and wave speed *c* travelling in the +*z* direction. The frequency of this wave is $f = c/\lambda$. The porous medium representing the PVS is assumed to have constant porosity ϕ and Darcy permeability κ. The fluid that saturates the PVS is assumed to be Newtonian and incompressible and have constant viscosity μ and density ρ.

In an inertial reference frame in which the porous medium moves with velocity $\underline{v_m}$, the governing equation is the generalized Brinkman-extended Darcy equation (Brinkman, 1947; Nield and Bejan, 1998; Edelman, 1999)

$$\rho\left(\frac{\partial \underline{v}}{\partial t}+\underline{v}\cdot\underline{\nabla}\underline{v}\right)=-\underline{\nabla}p-\frac{\phi\mu}{\kappa}\left(\underline{v}-\underline{v_m}\right). \quad (2.1)$$

Equation (2.1) is valid in any inertial reference frame (as opposed to the original Brinkman-extended Darcy equation which is only valid when the porous medium is stationary in the chosen reference frame).

The equation of continuity is

$$\underline{\nabla}\cdot\underline{v}=0. \qquad (2.2)$$

Coordinate transformations often are useful in solving peristalsis-related problems (see, for example, Shapiro et al., 1969). Instead of working in the laboratory frame Σ in which the porous medium (the PVS) is stationary and the peristaltic wave is traveling, we switch to the wave frame Σ' in which the peristaltic wave appears stationary and the porous medium is traveling. The coordinate transformations are $r'=r,\theta'=\theta,z'=z-ct,t'=t$, and the corresponding velocity transformations are $v_r'=v_r,v_\theta'=v_\theta,v_z'=v_z-c$. An immediate advantage of working in the wave frame Σ' is that the wave form on the inner wall in Σ' is expressed as $h(t',z')=R_1+b\sin\left(2\pi z'/\lambda\right)$, which is independent of time. Another advantage of working in Σ' is that the periodic motion of the fluid in Σ is transformed into a steady-state flow in Σ' (Shapiro et al., 1969).

Axisymmetry of the problem dictates that $v'_{\theta'}=0$ and $\frac{\partial}{\partial\theta'}=0$. The simplified equations in Σ' are as follows:

r' component $$\rho\left[v_{r'}'\frac{\partial v_r'}{\partial r'}+v_{z'}'\frac{\partial v_{r'}'}{\partial z'}\right]=-\frac{\partial p'}{\partial r'}-\frac{\phi\mu}{\kappa}v_{r'}' \quad (2.3)$$

z' component $$\rho\left[v_{r'}'\frac{\partial v_{z'}'}{\partial r'}+v_{z'}'\frac{\partial v_{z'}'}{\partial z'}\right]=-\frac{\partial p'}{\partial z'}-\frac{\phi\mu}{\kappa}v_{z'}'-\frac{\phi\mu c}{\kappa} \quad (2.4)$$

Next we impose the lubrication approximation. This approximation is usually applied to thin

film flows in empty spaces, rather than spaces filled by a porous medium.

Table 2.1: Values for the parameters used in the model.

Parameter	Symbol	Value	Reference
Inner radius	R_1	1×10^{-5} m	Lightfoot, 1973.
Outer radius	R_2	1.1×10^{-5} m	Ichimura et al., 1991.
Wave amplitude	b	5×10^{-7} m 2.5×10^{-7} m (baseline) 1.25×10^{-7} m	Bilston et al., 2003.
Wave speed	c	1 m·s^{-1}	Gladdish et al., 2005; Hoeks et al., 1999; Lightfoot 1973.
Wave frequency	f	5 Hz	Hadaczek et al., 2006.
Viscosity	μ	9×10^{-4} Pa·s	Bloomfield, 1998.
Hydraulic permeability	K	2×10^{-12} m^4·N^{-1}·s^{-1} 2×10^{-11} m^4·N^{-1}·s^{-1} (baseline) 2×10^{-10} m^4·N^{-1}·s^{-1}	Neeves et al., 2006; Smith and Humphrey, 2007.
Porosity	ϕ	0.2	Sarntinoranont et al., 2003; Sarntinoranont et al., 2006.

However, it can be shown that under the conditions $\mathrm{Re} = \rho c\kappa / \mu\lambda \ll 1$ and $\beta = R_2 / \lambda \ll 1$ (which can be verified with numbers from Table 2.1), the governing

equations can be simplified to

$$\frac{\partial p'}{\partial r'} = 0 \text{ and} \qquad (2.5)$$

$$\frac{\partial p'}{\partial z'} = -\frac{\phi\mu}{\kappa} v_{z'}' - \frac{\phi\mu c}{\kappa}. \qquad (2.6)$$

Equation (2.5) leads to

$$p' = p'(z') \qquad (2.7)$$

Equation (2.6) leads to

$$v_{z'}'(z') = -\frac{\kappa}{\phi\mu}\frac{dp'}{dz'} - c \qquad (2.8)$$

In the wave frame Σ', the volumetric flow rate is a constant, which means that

$Q' = \int_{h(z')}^{R_2} v_{z'}' \cdot 2\pi r' dr'$ is independent of z'. Substituting (2.8) into the expression for the flow rate and carrying out the integration gives

$$Q' = \pi\left[R_2^2 - h^2(z')\right]\left(-\frac{\kappa}{\phi\mu}\frac{dp'}{dz'} - c\right). \qquad (2.9)$$

Solving (2.9) for the pressure gradient gives,

$$\frac{dp'}{dz'} = -\frac{\phi\mu}{\kappa}\left\{\frac{Q'}{\pi\left[R_2^2 - h^2(z')\right]} + c\right\}. \qquad (2.10)$$

Since $h(z')$ is a periodic function of z' with period λ, (2.10) shows that dp'/dz' is also a periodic function of z' with a period of λ. The integral of dp'/dz' with respect to z' on any interval with length λ should be a constant $\Delta p_\lambda'$ independent of the starting point of the interval. Some straightforward calculations give the following result for $\Delta p_\lambda'$:

$$\Delta p_\lambda ' = \frac{\phi c \mu \lambda}{\kappa}\left\{ -\frac{Q'}{4\pi c R_2^2}\left[\frac{1}{\sqrt{\left(1-\frac{R_1}{R_2}\right)^2 - \left(\frac{b}{R_2}\right)^2}} + \frac{1}{\sqrt{\left(1+\frac{R_1}{R_2}\right)^2 - \left(\frac{b}{R_2}\right)^2}} \right] - 1 \right\}. \quad (2.11)$$

In the laboratory frame Σ, the pressure change per wavelength $\Delta p_\lambda = \Delta p_\lambda '$. The volumetric flow rate at time *t* across a cross-section at *z* is

$Q(t,z) = 2\pi \int_{h(t,z)}^{R_2} \phi v_z r dr = 2\pi\phi \int_{h(t,z)}^{R_2} \left(v'_{z'}(z') + c \right) r dr = \frac{1}{2}\phi Q' + \pi\phi c\left(R_2^2 - h^2\right)$, where

$h = h(t,z) = R_1 + b\sin\left(\frac{2\pi}{\lambda}(z-ct)\right)$. Substituting these results in (2.11) and solving for $Q(t,z)$ gives

$$Q(t,z) = -\frac{2\pi\phi c R_2^2\left(\frac{\kappa \Delta p_\lambda}{\phi c \mu \lambda} + 1\right)}{\frac{1}{\sqrt{\left(1-\frac{R_1}{R_2}\right)^2 - \left(\frac{b}{R_2}\right)^2}} + \frac{1}{\sqrt{\left(1+\frac{R_1}{R_2}\right)^2 - \left(\frac{b}{R_2}\right)^2}}} + \pi\phi c\left(R_2^2 - h^2\right) \quad (2.12)$$

A time-averaged flow rate can be defined as $\overline{Q}(z) = \frac{1}{T}\int_0^T Q(t,z)\,dt$. After a short calculation, we find that the volumetric flow rate is independent of *z* and given by

$$\overline{Q} = \pi\phi c R_2^2 \left\{ \frac{2\left(-\frac{\kappa \Delta p_\lambda}{\varepsilon c \mu \lambda} - 1\right)}{\frac{1}{\sqrt{\left(1-\frac{R_1}{R_2}\right)^2 - \left(\frac{b}{R_2}\right)^2}} + \frac{1}{\sqrt{\left(1+\frac{R_1}{R_2}\right)^2 - \left(\frac{b}{R_2}\right)^2}}} + 1 - \left(\frac{R_1}{R_2}\right)^2 - \frac{1}{2}\left(\frac{b}{R_2}\right)^2 \right\}. \quad (2.13)$$

2.3 Results and Discussion

At first glance, the lubrication approximation has reduced the nonlinear governing equations to a linear form, and it is tempting to solve the problem by using the superposition principle, i.e. the total volumetric flow rate is the sum of contributions from the pressure gradient and the peristaltic movement of the boundary. In the wave frame Σ' the reduced governing equation is inhomogenous (equation (2.6)), while in the laboratory frame Σ the boundary is moving. These complications make the superposition principle inapplicable in either reference frame. In fact, the pressure gradient and the peristaltic wave are coupled in the solution.

To illustrate this point, it is helpful to consider the special case where b/R_2 is very small. In this case, a Taylors expansion in b/R_2 of the right side of (2.13) gives to second order in b/R_2:

$$\overline{Q} \approx \pi\phi c R_2^2 \left\{ \left[1-\left(\frac{R_1}{R_2}\right)^2 - \frac{1+3\left(\frac{R_1}{R_2}\right)^2}{2\left(1-\left(\frac{R_1}{R_2}\right)^2\right)}\left(\frac{b}{R_2}\right)^2 \right] \left(-\frac{\kappa\Delta p_\lambda}{\phi c\mu\lambda}-1\right) + 1-\left(\frac{R_1}{R_2}\right)^2 - \frac{1}{2}\left(\frac{b}{R_2}\right)^2 \right\}. \quad (2.14)$$

Equation (2.14) can be rewritten as

$$\overline{Q} \approx \pi\phi c R_2^2 \left\{ \left(1-\left(\frac{R_1}{R_2}\right)^2\right)\left(-\frac{\kappa\Delta p_\lambda}{\phi c\mu\lambda}\right) + \frac{2\left(\frac{R_1}{R_2}\right)^2}{1-\left(\frac{R_1}{R_2}\right)^2}\left(\frac{b}{R_2}\right)^2 + \frac{1+3\left(\frac{R_1}{R_2}\right)^2}{2\left(1-\left(\frac{R_1}{R_2}\right)^2\right)}\left(\frac{b}{R_2}\right)^2 \frac{\kappa\Delta p_\lambda}{\phi c\mu\lambda} \right\}. \quad (2.15)$$

The first term on the right hand side of equation (2.15) comes from the pressure gradient (set b=0 in equation (2.15)). This term is the flow rate for pressure-driven flow through an annulus filled with the porous medium. The second term comes from peristaltic wave with very small

amplitude (set Δp_λ =0 in equation (2.13) and Taylor expand with respect to b/R_2). The third term represents the coupling between the pressure gradient and the peristaltic wave. This coupling term is not necessarily small compared to the second term since we didn't impose any restrictions on the magnitude of Δp_λ . But under the condition that b/R_2 is small, this coupling term is always small compared to the first term, regardless of the magnitude of Δp_λ .

It is interesting to compare these results with those obtained by Bilston et al. (2003) who carried out fluid dynamic simulations to model numerically fluid flow in the PVS in the spinal cord. They assumed that the PVS within the spinal cord was an empty space (as opposed to a porous medium). From equation (2.13), we see that in our model the flow rate has a linear dependence on the pressure gradient, which was also reported by Bilston et al (2003). In the absence of a pressure gradient and for small wave amplitudes, the flow rate is

$$\frac{2\left(\frac{R_1}{R_2}\right)^2}{1-\left(\frac{R_1}{R_2}\right)^2}\left(\frac{b}{R_2}\right)^2 \cdot \pi c R_2^2 .$$

This flow rate is proportional to the wave speed, which was also reported by Bilston et al (2003). However, this flow rate is proportional to the square of the wave amplitude, rather than the linear relationship reported by Bilston et al (2003). Our model predicts that there is a critical adverse pressure gradient at which the flow rate drops to zero. For example, using the values $b = 1.25\times10^{-7}$ m and $K = 2\times10^{-10}$ $\mathrm{m^4\cdot N^{-1}\cdot s^{-1}}$ from Table 2.1, we find $\bar{Q}$ in equation (2.13) is zero for a pressure gradient of 9.4×10^{6} $\mathrm{Pa\cdot m^{-1}}$. A larger *b* value and/or a smaller *K* value will give a larger critical adverse pressure gradient value. Bilston et al (2003) reported this pressure gradient value as 1.4×10^{7} $\mathrm{Pa\cdot m^{-1}}$.

Schley et al. (2006) proposed a mathematical model to explain the reverse perivascular

transport of amyloid-β out of the brain. It can be shown that in our model, the time averaged displacement of a tracer particle is always positive regardless of the initial position of the particle, which means that there is no reverse transport anywhere in the PVS. Mathematically, reverse transport can only happen when $\underline{\nabla} \times \underline{v} \neq \underline{0}$. Yet, it is well-known that Darcy's flow is always irrotational. In our model the PVS within the brain is modeled as a porous medium (partially filled with and supported by cells), and we chose 1 μm (Ichimura et al, 1991) as the width of the PVS (although its value depends on the size of the blood vessel). We use equation (2.1) to study the bulk fluid flow in this porous medium. The boundary layer flow cannot be studied by equation (2.1) because terms that are important in the boundary layer (i.e. fluidic viscous term) are not included in equation (1) (Deen, 1998). The thickness of this boundary layer is on the order of $\sqrt{\kappa}$, which is 42 nm for $K = 2\times10^{-12}$ $m^4N^{-1}s^{-1}$ and 420 nm for $K = 2\times10^{-10}$ $m^4N^{-1}s^{-1}$. Since the thickness of this layer is comparable to the pore size of the porous medium, it is feasible to model this layer as non-porous space and use Navier-Stokes equation to study the details in this layer. In fact, this is what Schley et al. (2006) did when they modeled the PVS as an empty annulus space with a width of 100-150 nm. Hence, there are no contradictions between our model and their model.

As mentioned in the introduction, we are particularly interested in the combined effects of the peristaltic motion of the blood vessel wall and CED treatment. In CED, drugs are infused directly into the brain tissue through a needle or catheter implanted deep inside the brain. Owing to the elasticity of brain tissue, the tissue during the infusion retracts from the high pressure at the needle outlet and forms a fluid-filled cavity at the tip of the needle. Infused fluid flows from the cavity into the surrounding tissue. The macroscopic (on the length scale of the brain) pressure field due to a single point source corresponding to the outlet of the needle was found to be (Neeves et al., 2006)

$$P(R) = \frac{P_o \cdot a}{R}, \quad (2.16)$$

where P_o is the pressure in a fluid-filled cavity of radius a at the needle tip and R is the distance from the source. A typical value for P_o is 7 kPa and a typical value for a is 13 μm (Neeves et al., 2006).

At location R the microscopic (on the length scale of a single blood vessel) pressure gradient in the radial direction, with respect to the location of the source, is

$$\frac{dP}{dR} = -\frac{P_o \cdot a}{R^2} \quad (2.17)$$

The interaction between the peristaltic motion of the blood vessel wall and the CED infusion pressure gradient in (2.17) depends on the orientation of the blood vessel under investigation. For example, if the blood vessel at location R is oriented perpendicular to the radial direction, the external pressure gradient generated by CED will have little influence on the pressure gradient in the PVS in the blood vessel direction. The opposite limit is the case in which the blood vessel under investigation at location R is oriented in the radial direction and the peristaltic wave travels in the outward radial direction. In this case, the pressure change per wavelength Δp_λ in equation (13) can be calculated as $-P_o \cdot a \cdot \lambda / R^2$, which translates into

$$\overline{Q}(R) = \pi\phi c R_2^2 \left\{ \frac{2\left(\frac{\kappa P_o a}{\phi c \mu R^2} - 1\right)}{\frac{1}{\sqrt{\left(1-\frac{R_1}{R_2}\right)^2 - \left(\frac{b}{R_2}\right)^2}} + \frac{1}{\sqrt{\left(1+\frac{R_1}{R_2}\right)^2 - \left(\frac{b}{R_2}\right)^2}}} + 1 - \left(\frac{R_1}{R_2}\right)^2 - \frac{1}{2}\left(\frac{b}{R_2}\right)^2 \right\} \quad (2.18)$$

This result shows that $\overline{Q}$ depends on the location R of the blood vessel under investigation. To compare the effects of CED therapy in the presence and in the absence of peristalsis of blood vessel walls, we define the following dimensionless number

$$PW(R)=\frac{\overline{Q}(R)-\overline{Q}(R)\big|_{b=0}}{\overline{Q}(R)}\times 100\%\,,\ (2.19)$$

where *PW* stands for "peristaltic wave". This number characterizes the fractional contribution to fluid flow from the peristaltic wave. It can be shown that *PW* is always non-negative.

At present, we lack experimental data for exact comparisons with theoretical predictions. Hence, we turn to a sensitivity analysis on the parameters involved in the model, especially *b* and *K*, because there are significant uncertainties in their values. Figure 2.2 shows values of *PW*(%) as a function of distance *R* from the infusion needle for three different values of *K* and *b* fixed at its baseline value of 0.25 μm. Figure 2.3 shows values of *PW*(%) as a function of distance *R* for three different values of *b* and *K* fixed at its baseline value of 2×10^{-12} $m^4 \cdot N^{-1} \cdot s^{-1}$. The figures show

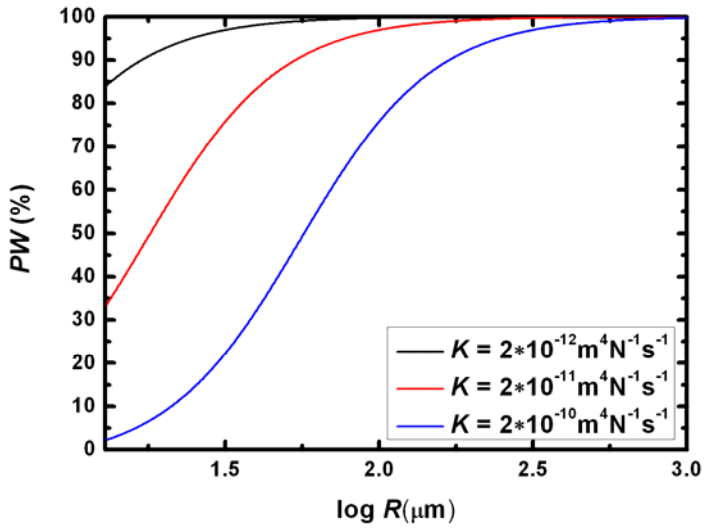

Figure 2.2: *PW*(%) versus log(*R*(μm)) for three different *K* values with baseline *b* value.

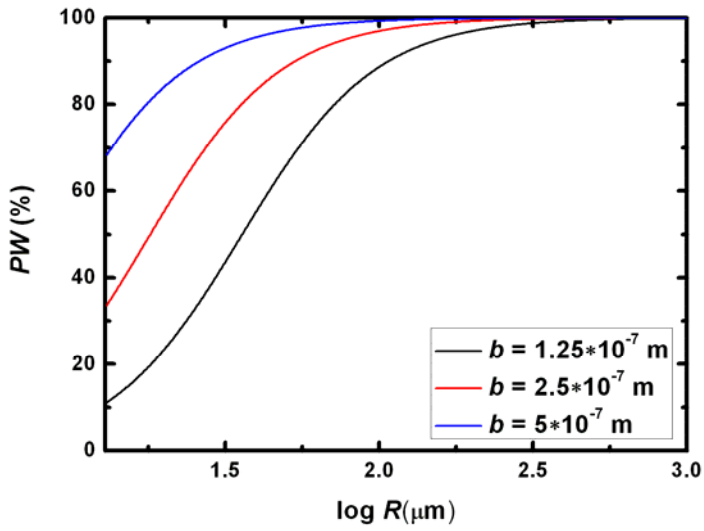

Figure 2.3: *PW*(%) versus log(*R*(μm)) for three different *b* values with baseline *K* value.

that whether fluid transport in the PVS is predominantly driven by CED or by the peristaltic wave depends on location *R* and the particular parameter values of *b* and *K*. In all cases depicted in Figure 2.2 and 2.3, at sufficiently large distances from the CED infusion source (~1000 μm) the main contribution to fluid transport comes from the peristaltic wave. Note that if the blood vessel is oriented perpendicular to the radial direction, the fractional contribution provided by the peristaltic wave is always zero with respect to the fluid transport in the radial direction. Near the infusion source, whether the peristaltic wave is important or not depends on the particular choice of parameter values. In some cases, the peristaltic wave makes a significant fractional contribution to fluid transport near the infusion source. For example *PW*(%) is as large as 80% near $R = a$ for $b = 2.5\times10^{-7}$ m and $K = 2\times10^{-12}$ $m^4 \cdot N^{-1} \cdot s^{-1}$. It seems reasonable that a lower value of the hydraulic permeability *K* should result in an increased fractional contribution from the peristaltic wave, which is indicated in Figure 2.2. *b* is the half amplitude of the wave. Also, it seems reasonable that a thicker PVS, corresponding to a larger the value of *b*, should result in an

increased fractional contribution from the peristaltic, which is indicated in Figure 2.3. The values of b among the cases in Figure 2.3 differ from each other by a factor of 2, while the values of K among the cases in Figure 2.2 differ from each other by a factor of 10. This suggests that system is much more sensitive to the value of b than to the value of K. In the previous discussion, we see that under certain conditions the system is additive (See equation (2.15)). The sensitivity of PW to the values of b and K can be understood by noticing that the CED pressure driven flow rate (the first term on the right hand side of equation (2.15)) is proportional to K while the peristaltic wave driven flow rate (the second term on the right hand side of equation (2.15)) is proportional to b^2.

CHAPTER 3

ULTRASOUND ASSISTED DRUG DELIVERY

3.1 Introduction

Ultrasound has a long history of use in medicine for diagnostic imaging applications (Lindner et al., 2004; Moore et al., 2004). As an imaging tool, it has been widely employed and valued for its real time applications, low cost, simplicity, and safety. Recently, there have been considerable efforts to deveop therapeutic uses of ultrasound. As a matter of fact, applications of ultrasound as a method of therapy came earlier than diagnostic ultrasound (Ng and Liu, 2002). As early as the 1930s and 1940s in Europe, therapeutic ultrasound was used as irradiation source for generating heat. Current therapeutic applications of ultrasound, either by itself or in combination with drugs, span a spectrum, including the treatment of diabetes, stroke, cancer, cardiovascular diseases, infections, osteoporosis, thrombosis, glaucoma, nerve damage, skin wounds and bone fractures.

In particular, ultrasound can be utilized to enhance the delivery and effect of therapeutic drugs. In one of the earliest such studies, Fellinger and Schmidt (1954) reported the successful use of ultrasound in combination with hydrocortisone for the treatment of polyarthritis. The most extensively studied example is the use of ultrasound to enhance transdermal drug delivery (Lavon and Kost, 2004; Mitragotri, 2004). This technique of driving drug molecules across the percutaneous barrier is called ‘phonophoresis’ (Tyle and Agrawala, 1989). More recently, Lewis et al. (2007, 2009) have focused on the application of ultrasound in the enhancement of local drug delivery, especially to neurological tissues.

Local delivery of therapeutics often allows higher doses to be delivered without side effects that restrict dose levels in systemic delivery. Local delivery can be combined with controlled release to provide sustained high concentrations of drug in the immediate vicinity of affected tissue (Gueri et al., 2004; Panyam and Labhasetwar, 2003; Westphal et al., 2003). Local delivery is especially important in treating brain disorders, because most therapeutics administered intravenously do not cross the blood-brain barrier.

Transport enhancement by ultrasound can be explained by a variety of thermal and non-thermal mechanisms among which acoustic cavitation and bubble-assisted microstreaming are the most popular ones (Guzman et al., 2002; Keyhani et al., 2001). Studies in vitro and in vivo with animal models have revealed that acoustic cavitation and bubble-assisted microstreaming, if not well controlled, can cause tissue damage (Adam et al, 2010; Speed, 2001; Wells, 1977). There are few reports on the therapeutic use of low power ultrasound in the absence of cavitation and bubble-assisted microstreaming. Low power ultrasound may provide the potential benefits of prolonged treatment time without tissue damage and simpler electronic controls that eliminate the need of using short pulses to mitigate tissue damage.

In this chapter, we present a theoretical analysis on the fluid and solid mechanics in a poroelastic medium induced by low power ultrasound. The goal is to understand from a mathematical and physical point of view, how and to what extent low power ultrasound can affect or enhance drug transport in soft tissues. We start with basic mass and momentum conservation equations together with appropriate constitutive equations. Linearization of the governing equations leads to plane wave solutions of the problem. Numerical analysis with parameter values relevant to brain tissues are carried out. We propose that low power ultrasound can enhance transport through its local mixing effect. We have also discovered an interesting and important phenomenon when the mechanical properties of brain tissue under high frequencies

are varied as input parameters.

3.2 Mathematical Model

We treat brain tissue as a fluid-saturated poroelastic network (Basser, P., 1992; Edelman, I.Y., 1999; Netti et al., 1997).

Mass conservation for the fluid and the solid phases are written as

$$\frac{\partial}{\partial t}\left(\phi\rho_f\right)+\underline{\nabla}\cdot\left(\phi\rho_f\underline{v_f}\right)=0 \quad (3.1)$$

$$\frac{\partial}{\partial t}\left[\left(1-\phi\right)\rho_s\right]+\underline{\nabla}\cdot\left[\left(1-\phi\right)\rho_s\underline{v_s}\right]=0 \quad (3.2)$$

where ϕ is the porosity, ρ_f is the density of the fluid phase, $\underline{v_f}$ is the velocity in the fluid phase, ρ_s is the density of the solid phase, and $\underline{v_s}$ is the velocity in the solid phase.

Momentum conservation for the fluid and the solid phases are written as

$$\phi\rho_f\left(\frac{\partial}{\partial t}+\underline{v_f}\cdot\underline{\nabla}\right)\underline{v_f}=\phi\underline{\nabla}\cdot\underline{\underline{\sigma_f}}-\underline{\prod} \quad (3.3)$$

$$\left(1-\phi\right)\rho_s\left(\frac{\partial}{\partial t}+\underline{v_s}\cdot\underline{\nabla}\right)\underline{v_s}=\left(1-\phi\right)\underline{\nabla}\cdot\underline{\underline{\sigma_s}}+\underline{\prod} \quad (3.4)$$

where $\underline{\underline{\sigma_f}}$ is the total stress in the fluid phase, $\underline{\underline{\sigma_s}}$ is the total stress in the solid phase, and $\underline{\prod}$ is the sum of forces exerted by the two phases upon each other.

The densities of the fluid and solid phases are written as

$$\rho_f=\rho_{f0}\left[1+\beta_f\left(p_f-p_{f0}\right)\right] \quad (3.5)$$

$$\rho_s=const. \quad (3.6)$$

where p_f is the pressure in the fluid phase, ρ_{f0} is the reference fluid density, p_{f0} is the

reference fluid pressure, and β_f is the compressibility of the fluid.

Stress-strain relations for the fluid and the solid phase are written as

$$\underline{\underline{\sigma}}_f = -p_f \underline{\underline{I}} \quad (3.7)$$

where $\underline{\underline{I}}$ is the unit tensor, and

$$\underline{\underline{\sigma}}_s = 2G\underline{\underline{\varepsilon}}_s + \lambda\left(Tr\underline{\underline{\varepsilon}}_s\right)\underline{\underline{I}} \quad (3.8)$$

where G and λ are Lame constants for the solid phase.

The strain tensor $\underline{\underline{\varepsilon}}_s$ satisfies

$$\left(\frac{\partial}{\partial t} + \underline{v}_s \cdot \underline{\nabla}\right)\underline{\underline{\varepsilon}}_s = \frac{1}{2}\left[\underline{\nabla}\underline{v}_s + \left(\underline{\nabla}\underline{v}_s\right)^T\right] \quad (3.9)$$

Furthermore, we can write

$$\underline{\prod} = \phi^2\Phi\left(\underline{v}_f - \underline{v}_s\right) \quad (3.10)$$

where Φ is the friction coefficient or the inverse of the hydraulic permeability.

We can linearize this set of equations by the following procedure.

At equilibrium and in the absence of any external stimuli (e.g. ultrasound),

$$\Phi = \Phi_0, \phi = \phi_0, p_f = p_0, \underline{v}_f = \underline{0}, \underline{v}_s = \underline{0}, \underline{\underline{\varepsilon}}_s = \underline{\underline{0}}$$

where Φ_0, ϕ_0 and p_0 are constants.

In the presence of external stimuli (e.g. ultrasound), we can decompose the dynamic variables into two components: an equilibrium component and a perturbed component,

$$\Phi = \Phi_0 + \Phi', \phi = \phi_0 + \phi', p_f = p_0 + p_f', \underline{v}_f = \underline{0} + \underline{v}_f', \underline{v}_s = \underline{0} + \underline{v}_s', \underline{\underline{\varepsilon}}_s = \underline{\underline{0}} + \underline{\underline{\varepsilon}}_s' \quad (3.11)$$

Here, we take $p_{f0} = p_0$ in equation (3.5), where p_0 is the atmospheric pressure. In the case of low power input into the system by the ultrasound, we can assume that the primed variables are

small, and we will keep them to the first order as an approximation. Rewriting the governing equations in terms of the primed variables leads to the following set of equations:

$$\phi_0 \beta_f \frac{\partial p_f'}{\partial t} + \frac{\partial \phi'}{\partial t} + \phi_0 \underline{\nabla} \cdot \underline{v_f}' = 0 \quad (3.12)$$

$$-\frac{\partial \phi'}{\partial t} + (1-\phi_0) \underline{\nabla} \cdot \underline{v_s}' = 0 \quad (3.13)$$

$$\rho_{f0} \frac{\partial}{\partial t} \underline{v_f}' + \underline{\nabla} p_f' + \phi_0 \Phi_0 \left(\underline{v_f}' - \underline{v_s}' \right) = \underline{0} \quad (3.14)$$

$$(1-\phi_0) \rho_s \frac{\partial}{\partial t} \underline{v_s}' - (1-\phi_0) \underline{\nabla} \cdot \left[2G \underline{\underline{\varepsilon_s}}' + \lambda \left(Tr \underline{\underline{\varepsilon_s}}' \right) \underline{\underline{I}} \right] - \phi_0^2 \Phi_0 \left(\underline{v_f}' - \underline{v_s}' \right) = \underline{0} \quad (3.15)$$

$$\frac{\partial}{\partial t} \underline{\underline{\varepsilon_s}}' = \frac{1}{2} \left[\underline{\nabla} \underline{v_s}' + \left(\underline{\nabla} \underline{v_s}' \right)^T \right] \quad (3.16)$$

For simplicity, we will focus on the case where the dynamic variables only depend on the *x* coordinate (i.e. no *y* and *z* coordinate dependence). In this case, we write plane wave solutions for any primed variable in the form $f'(x,t) = f' \cdot e^{i(kx-\omega t)}$, where *f'*, *k* and ω are constants (We use the same symbol *f'* after factoring out $e^{i(kx-\omega t)}$ as long as there is no ambiguity.) The differential equations (3.12)-(3.16) are then transformed into a set of linear algebraic equations. After eliminating $\underline{v_f}', \underline{v_s}'$ and $\underline{\underline{\varepsilon_s}}'$, we obtain

$$-k^2 p_f' + \left(\omega^2 \rho_{f0} \beta_f + i\omega \phi_0 \Phi_0 \beta_f \right) p_f' + \left(\frac{\omega^2 \rho_{f0}}{\phi_0} + \frac{i\omega \Phi_0}{1-\phi_0} \right) \phi' = 0 \quad (3.17)$$

$$-k^2 \phi' + \frac{i\omega \phi_0^2 \Phi_0 \beta_f}{K_v} p_f' + \left[\frac{\omega^2 \rho_s}{K_v} + \frac{i\omega \phi_0 \Phi_0}{K_v (1-\phi_0)} \right] \phi' = 0 \quad (3.18)$$

where $K_v = 2G + \lambda$.

If a non-trivial solution for equations (3.17) and (3.18) exists, k^2 must be an eigenvalue of the following matrix

$$\begin{bmatrix} \omega^2\rho_{f0}\beta_f + i\omega\phi_0\Phi_0\beta_f & \dfrac{\omega^2\rho_{f0}}{\phi_0} + \dfrac{i\omega\Phi_0}{1-\phi_0} \\ \dfrac{i\omega{\phi_0}^2\Phi_0\beta_f}{K_v} & \dfrac{\omega^2\rho_s}{K_v} + \dfrac{i\omega\phi_0\Phi_0}{K_v(1-\phi_0)} \end{bmatrix} \quad (3.19)$$

In general, there are four k values to be determined by matrix (3.19). It can be shown that there is at least one and at most two k values that are physically allowed and physically independent (See Appendix A).

We choose to set up a Cartesian coordinate system such that the ultrasound excitation source is positioned at the origin and the ultrasound propagation direction is the $+x$ direction (Note that the physics is independent of the choice and set up of coordinate system). Energy conservation requires that the ultrasound cannot amplify itself during propagation. Therefore, the physically allowed k value must have a positive real part and a positive imaginary part. A positive real part indicates that the ultrasound propagates in the $+x$ direction, and a positive imaginary part indicates that the ultrasound decays as it propagates. We substitute such a k value obtained from matrix (3.19) back into equations (3.17) and (3.18), and solve for the primed variables to obtain

$$p_f' = \left(\frac{\omega^2\rho_{f0}}{\phi_0} + \frac{i\omega\Phi_0}{1-\phi_0} \right) \cdot A \quad (3.20)$$

$$m' = \left(k^2 - \omega^2\rho_{f0}\beta_f - i\omega\phi_0\Phi_0\beta_f \right) \cdot A \quad (3.21)$$

$$v_f{}'_x = \left(\frac{i\omega\Phi_0\beta_f\phi_0}{1-\phi_0} + \frac{k^2}{\phi_0} \right) \cdot \frac{\omega A}{k} \quad (3.22)$$

$$v_s{}'_x = -\left(k^2 - \omega^2\rho_{f0}\beta_f - i\omega\phi_0\Phi_0\beta_f \right) \cdot \frac{\omega A}{k(1-\phi_0)} \quad (3.23)$$

where A is an unknown constant.

To determine the constant A, we use the energy conservation condition.

The mean rate of energy dissipation per unit volume is

$$R(x)=\frac{\phi^2\Phi}{T}\int_0^T\left\{\mathrm{Re}\left[v_{fx}(x,t)-v_{sx}(x,t)\right]\right\}^2 dt \quad (3.24)$$

where $T=\frac{2\pi}{\omega}$.

In the context of the perturbation approximation,

$$R(x)=\frac{{\phi_0}^2\Phi_0}{T}\int_0^T\left\{\mathrm{Re}\left[{v_f}'_x(x,t)-{v_s}'_x(x,t)\right]\right\}^2 dt$$
$$=\frac{{\phi_0}^2\Phi_0}{2}\left|{v_f}'_x(x,t)-{v_s}'_x(x,t)\right|^2$$
$$=\frac{{\phi_0}^2\Phi_0}{2}\left|\left({v_f}'_x-{v_s}'_x\right)e^{i(kx-\omega t)}\right|^2$$
$$=\frac{{\phi_0}^2\Phi_0}{2}\left|{v_f}'_x-{v_s}'_x\right|^2 e^{-2(\mathrm{Im}k)x} \quad (3.25)$$

where $|\square|$ denotes the modulus of a complex number.

Substituting equations (3.22) and (3.23) into equation (3.25) gives

$$R(x)=\frac{\Phi_0\omega^2|A|^2}{2|k|^2(1-\phi_0)^2}\left|\phi_0\omega^2\rho_{f0}\beta_f+k^2\right|^2 e^{-2(\mathrm{Im}k)x} \quad (3.26)$$

Energy conservation requires

$$\Omega=\int_0^{+\infty}R(x)\,dx=\frac{\Phi_0\omega^2|A|^2}{4(\mathrm{Im}k)|k|^2(1-\phi_0)^2}\left|\phi_0\omega^2\rho_{f0}\beta_f+k^2\right|^2 \quad (3.27)$$

where Ω is the power input per unit area by the ultrasound excitation source.

Solving equation (27) for $|A|$ gives

$$|A|=\frac{2|k|(1-\phi_0)}{\omega\left|\phi_0\omega^2\rho_{f0}\beta_f+k^2\right|}\sqrt{\frac{(\mathrm{Im}k)\Omega}{\Phi_0}} \quad (3.28)$$

3.3 Results and Discussion

In principle, the eigenvalues of matrix (3.19) and, thus, *k* can be obtained in closed forms. However, the mathematical formula would be rather lengthy and not very helpful in providing physical insights into the problem. Instead, we will discuss some special cases in which the eigenvalues of matrix (3.19) can be solved in simple forms.

Special case 1: $\Phi_0 = 0$ or $\omega \to \infty$. Either $\Phi_0 = 0$ or $\omega \to \infty$ will give the solution $k_1^2 = \omega^2 \rho_{f0} \beta_f$, $k_2^2 = \omega^2 \rho_s / K_v$. When the frequency of the ultrasound is high enough, the equations of motion become non-dispersive and uncoupled. The first solution corresponds to the acoustic wave propagating in the fluid phase, and the second solution corresponds to the acoustic wave propagating in the solid phase.

Special case 2: $\Phi_0 \to \infty$. The two solutions are $k_1^2 = 0$ and

$$k_2^2 = i\left(\omega \phi_0 \Phi_0 \beta_f + \frac{\omega \phi_0 \Phi_0}{K_v (1 - \phi_0)} \right).$$

From $k_1^2 = 0$, we have $v_f{}'_x(x,t) / v_s{}'_x(x,t) \to 1$. This does not correspond to a plane wave but a net in-phase oscillation of the solid phase with the fluid phase. From

$$k_2^2 = i\left(\omega \phi_0 \Phi_0 \beta_f + \frac{\omega \phi_0 \Phi_0}{K_v (1 - \phi_0)} \right),$$

We have $\dfrac{v_f{}'_x}{v_s{}'_x} \to -\dfrac{1 - \phi_0}{\phi_0}\left(K_v \beta_f + 1 \right)$.

The fact that $\mathrm{Im}\, k_2 \to \infty$ implies that the penetration depth $(1/\mathrm{Im}\, k_2)$ of this wave approaches zero. This is due to an infinite friction coefficient and a 180° out-of-phase behavior of the fluid

velocity and the solid velocity.

Special case 3: Φ_0 is very small but non-zero. The two solutions are

$$k_1^2 = \omega^2 \rho_{f0} \beta_f + \frac{i\omega\phi_0 \beta_f^2}{\beta_f - \frac{1}{K_v}} \Phi_0 ,\ k_2^2 = \frac{\omega^2 \rho_s}{K_v} + \frac{i\omega\phi_0 \left(K_v \beta_f \phi_0 - 1 \right)}{\left(1 - \phi_0 \right) \left(\beta_f - \frac{1}{K_v} \right)} \Phi_0 .$$

It is interesting to notice that when $\beta_f \approx 1/K_v$ (the fluid and the solid phase have similar "compressibility"), the Φ_0 correction terms are no longer small and the movement of the fluid and the solid phase are strongly coupled despite of a small friction coefficient.

In general, the eigenvalues of matrix (3.19) cannot be obtained in a simple form and numerical solutions are needed. For the purpose of a numerical study, we need the values of the various parameters appearing in the equations. As mentioned in the introduction, we use brain tissue as a model system (although the above mathematical model is applicable to other soft tissues that can be described as a poroelastic network). We summarize in Table 3.1 the nominal values to be used for those parameters. With these numbers substituted in matrix (3.19), we get one and only one physically allowed *k* value of $1.8 \times 10^4 + 1.7 \times 10^4 i$ m^{-1} (the other one represents a wave propagating and increasing without bound in the +*x* direction).

Acoustic cavitation occurs when the fluid pressure falls blow its vapor pressure. Therefore, the critical power input at which acoustic cavitation occurs can be calculated by setting the lowest fluid pressure point during one period to the vapor pressure of that fluid. Water vapor pressure at 37℃ is 6.27×10^3 Pa. We set $\left| p_f ' \right|$ in equation (20) to be $1.01 \times 10^5 - 6.27 \times 10^3 = 9.47 \times 10^4$ Pa, and get $\left| A \right| = 2.4 \times 10^{-14}$ m^2. From equations (21), (22), (23) and (27), we get $\left| m ' \right| = 7.9 \times 10^{-6}$, $\left| v_f '_x \right| = 2.1 \times 10^{-2}$ m·s^{-1}, $\left| v_s '_x \right| = 2.5 \times 10^{-3}$ m·s^{-1}, and $\Omega = 1.6 \times 10^2$ W·m^{-2}.

Table 3.1: Nominal values for the parameters.

Parameter	Symbol	Value	References
Ultrasound angular frequency	ω	6.28×10^{6} rad·s^{-1}	Lewis et al., 2007.
Porosity	ϕ_0	0.2	Sarntinoranont et al., 2003; Sarntinoranont et al., 2006.
Inverse hydraulic permeability	Φ_0	5×10^{11} N·s·m^{-4}	Neeves et al., 2006; Smith and Humphrey 2007.
Mechanical modulus	K_v	2.4×10^{9} Pa	Lippert, Rang and Grimm, 2004.
Solid density	ρ_s	1×10^{3} kg·m^{-3}	N/A
Fluid density	ρ_{f0}	1×10^{3} kg·m^{-3}	N/A
Fluid compressibility	β_f	4.6×10^{-10} Pa^{-1}	Fine and Millero, 1973.

First, we need to check whether the general assumption in Biot's theory of poroelasticity is satisfied with the parameter values listed in Table 1 since our theory is based on Biot's theory. The inverse of the real and the imaginary part of k is about 60 μm, which is the characteristic length over which dynamic variables could have significant changes. The pore sizes of brain tissues have been estimated to be between 38 and 64 nm (Thorne and Nicholson, 2006), which are much smaller than 60 μm. Therefore, the general assumption in Biot's theory is satisfied and we are allowed not only to use continuum mechanics, but also ignore acoustical scattering.

We also need to clarify several points concerning the constitutive equations used in the

model. First, in equation (3.7), we have neglected the internal fluid viscous term. The ratio of such a term to the medium force term scales as

$$\frac{\left|\mu_f \frac{\underline{\underline{v_f}}}{|k|^2}\right|}{\left|\phi\Phi\left(\underline{v_f}-\underline{v_s}\right)\right|} \sim \frac{\mu_f}{\phi_0\Phi_0|k|^2} << 1,$$

where μ_f is the viscosity of the fluid. Therefore, the internal fluid viscous term can be dropped with confidence. Second, we took the Lame constants *G* and λ in equation (3.8) to be real numbers, which means that the stress and the strain of the solid phase are in phase with respect to each other. We assume that the solid phase is pure elastic and non-dispersive and lump the dispersive effects into the friction between the fluid and the solid phase. In general, the magnitudes of *G* and λ depend on the frequencies of the harmonic excitations. Third, we took the friction coefficient Φ_0 to be a real number, which means that the frictional force between the fluid and the solid phase is in-phase with the velocity difference. This is not true for very high frequency oscillations. In our case, the frequency is low enough to guarantee the in-phase behavior (Biot, 1956a; Biot, 1956b; Johnson et al., 1987). In general, the magnitude of Φ_0 depends on the frequencies of the harmonic excitations. In our case, the frequency is low enough to guarantee that Φ_0 can be treated as independent of the frequency (Johnson et al., 1987). Fourth, the dimensionless group $\rho_{f0}\left|v_f{}'_x - v_s{}'_x\right| / \sqrt{\mu_f \Phi_0}$ is much less than 1, indicating that the flow is in the Darcy regime and the Forchheimer generalization is not needed (Nield and Bejan, 1998).

To study the fluid transfer in the medium, we define two variables as follows:

$$M_0(x) = \sqrt{\frac{1}{T}\int_0^T \left[\mathrm{Re}\, v_{fx}(x,t)\right]^2 dt}$$

and

$$M_1(x) = \sqrt{\frac{1}{T}\int_0^T \left[\frac{\partial \operatorname{Re} v_{fx}(x,t)}{\partial x}\right]^2 dt}\,.$$

The first variable $M_0(x)$ is the root mean square of the fluid velocity averaged over time. It reflects how fast the transient motion of the fluid phase is. The second variable $M_1(x)$ is the root mean square of the fluid velocity gradient averaged over time. It reflects how abrupt are changes in velocity, which is likely to correlate with the extent of convective mixing of solutes. Notice that a net translation of the fluid (plug flow) does not contribute to convective mixing within the fluid. With some straightforward algebra, we can show that $M_0(x) = \left|v_f{}'_x\right| e^{-(\operatorname{Im} k)x}/\sqrt{2}$ and $M_1(x) = \left|k v_f{}'_x\right| e^{-(\operatorname{Im} k)x}/\sqrt{2}$. At the characteristic length $x = 1/\operatorname{Im} k$, the numerical value for M_0 is 5.5×10^{-3} m·s^{-1} and that for M_1 is 1.4×10^{2} s^{-1}. The inverse of M_1 (7.1 ms) has the dimension of time and can be considered as the characteristic time for local convective mixing.

To study the heat transfer in the medium, we define a local Nusselt number

$$Nu(x) = \frac{1}{\alpha}\int_0^T \left\{\operatorname{Re}\left[v_{fx}(x,t)\right]\right\}^2 dt = \frac{T\left|v_f{}'_x\right|^2}{2\alpha} e^{-2(\operatorname{Im} k)x},$$

where α is the thermal diffusivity of brain tissue (typically 1.4×10^{-7} m^2·s^{-1}, see Elwassif et al., 2006). Heat is generated in the medium due to dissipation of mechanical energy carried by the ultrasound. $Nu(x)$ decays exponentially and has a maximal value of 1.6×10^{-3} at the origin. Therefore, we can conclude that heat transfer in the medium is everywhere dominated by conduction. Since the heating source term $R(x)$ decays exponentially, it is expected that temperatures near the origin (ultrasound excitation source) will rise much faster than those far away from the origin when the ultrasound is applied to the medium. The localized heat generation might be able to be used to kill malignant cells in hyperthermia therapy. The increase in temperature will also increase the diffusion coefficients of the drug molecules and thus

enhance diffusional transport into soft tissues.

To study the mass transfer in the medium, we define a local Peclet number

$$Pe(x) = \frac{1}{D}\int_0^T \left\{\mathrm{Re}\left[v_{fx}(x,t)\right]\right\}^2 dt = \frac{T\left|v_f{}'_x\right|^2}{2D} e^{-2(\mathrm{Im}\,k)x},$$

where D is the diffusion coefficient of the drug molecule (typically 1×10^{-11} $\mathrm{m^2\cdot s^{-1}}$, see Morrison et al., 1994). At x = 90 μm, Pe = 1. Therefore, mass transfer is dominated by convection within the 90 μm of the origin and by diffusion beyond 90 μm. The concentration profile for drug molecules is expected to have a convective plateau extending 90 μm into the tissue followed by a diffusive tail extending to infinity. Convection and diffusion are not isolated processes and are quite often strongly coupled to each other in determining the overall mass transfer behavior of the system. It is well known that agitation can reduce the amount of time needed for mixing or homogenization. The dimensionless variable $Pe(x)$ can be used to quantify the effects of fluid agitation on mass transfer in the porous medium. It characterizes the relative importance of local convective fluidic mixing to pure solute diffusion in solute transport. In this sense, $D(1+Pe(x))$ can be considered as a local effective diffusion coefficient. At the characteristic length $x = 1/\mathrm{Im}\,k$, $Pe(x)$ takes a value of 3.0.

Next, we examine how the frequency of the excitation source will affect transport. For this purpose, we sweep the frequency from 0.5 MHz to 10 MHz (which corresponds to an angular frequency from 3.14 MHz to 62.8 MHz) in our numerical calculations. It should be noted that the Lame constants of brain tissue are frequency-dependent. However, using the data presented by Lippert et al. (2004), we have found that the value of K_v is roughly constant in the frequency range specified above (although the respective values of G and λ change significantly). The results of this frequency-sweeping study are illustrated in Figure 3.1 – 3.4. In the plots, the indices

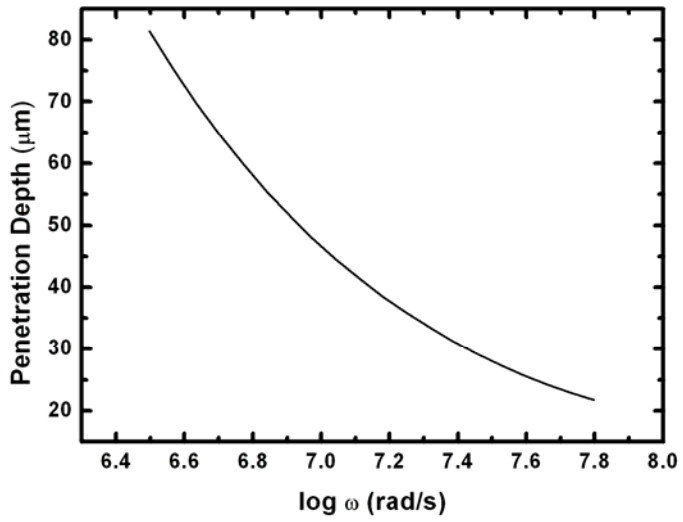

Figure 3.1: Frequency-sweeping results for penetration depth.

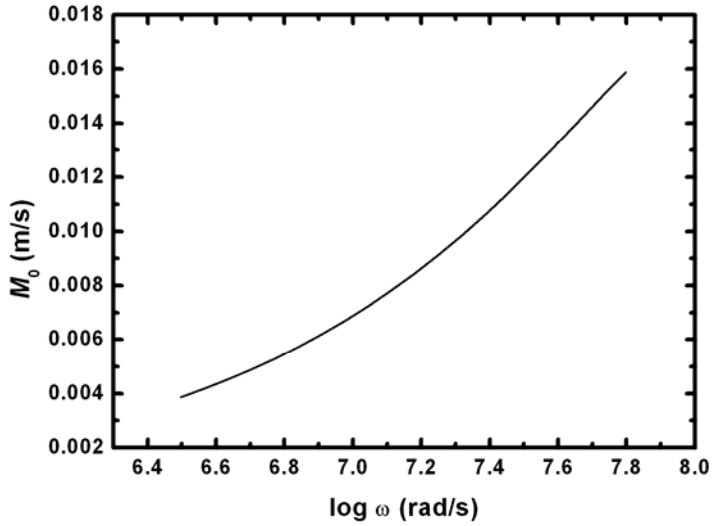

Figure 3.2: Frequency-sweeping results for M_0.

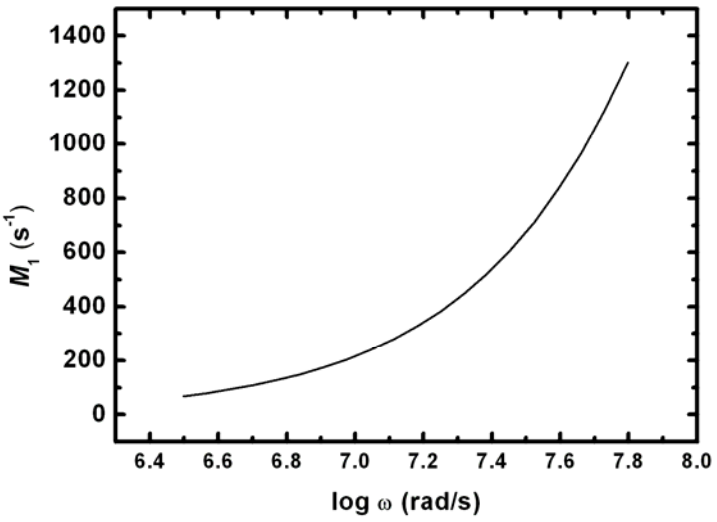

Figure 3.3: Frequency-sweeping results for M_1.

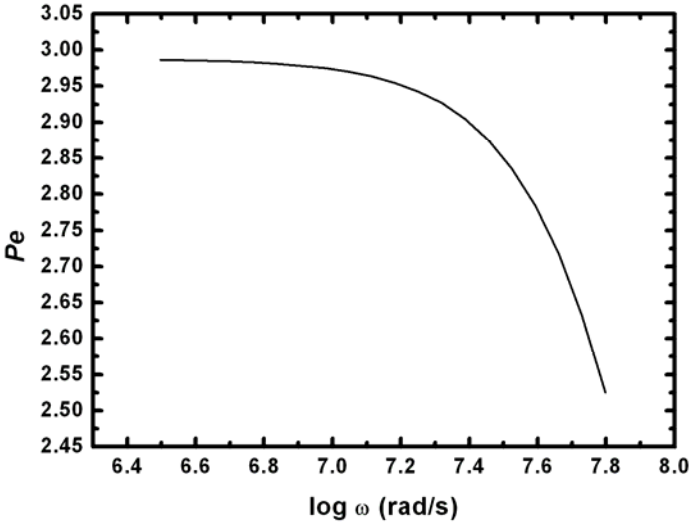

Figure 3.4: Frequency-sweeping results for *Pe*.

M_0, M_1, and *Pe* are the values of the functions $M_0(x)$, $M_1(x)$, and $Pe(x)$ taken at $x = 1/\operatorname{Im} k$.

When the frequency is increased, the penetration depth, defined as 1/Imk, increases monotonically. Both M_0 and M_1 increase with frequency. But Pe decreases with frequency, especially in the 4 MHz to 10 MHz range. This is because higher frequency leads to shorter period. Although the movement of the fluid becomes faster and more violent, it lasts for a shorter amount of time. It turns out that the shorter period counters the benefits of faster and more violent movement and leads to reduced local convective mixing.

Finally, we discuss an important numerical phenomenon that we have observed in our calculations: the emergence of a second pressure wave under certain circumstances. The discussion can be traced back to the high frequency properties of brain tissue. Many researchers have attempted to measure the mechanical moduli of brain tissue below 400 Hz using a variety of techniques, with different loading rates, strain limits, and various species. However, the published results have shown a great degree of disparity (Lippert et al., 2004). The differences between reported values from different studies can be as large as two orders of magnitude. We have only found one paper reporting high frequency properties of brain tissue (Lippert et al., 2004). Thus, it seems possible that the actual values of the mechanical moduli of brain tissue might be two orders of magnitude larger or smaller than those reported in Lippert et al. (2004). When K_v takes a nominal value of 2.4×10^9 Pa, there is one and only one physically allowed pressure wave, which decays as it propagates into tissue. This remains the case for increasing values of K_v until K_v reaches a value around $1.1\times10^{10}\,Pa$. At that value, a second physically allowed pressure wave emerges. Mathematically, this happens because when K_v reaches 1.1×10^{10} Pa, the number of eigenvalues of matrix (3.19) falling into the upper half of the complex plane changes from one to two. The previously physically forbidden wave, which grows as it propagates, becomes physically allowed due to a change of sign in Imk for that wave. The transition point of K_v is not very far away from its nominal value. The emergence of a

second physically allowed pressure wave has profound consequences in transport. To demonstrate these consequences, we set K_v at 1.1×10^{10} Pa and 2.4×10^{11} Pa, which is a reasonable upper limit set by experimental data and experimental variations. Then, we solve numerically for the wavelength $2\pi/\mathrm{Re}\,k$, penetration depth $1/\mathrm{Im}\,k$, Ω, M_0, M_1, and *Pe* (M_0, M_1, and *Pe* are calculated at $x = 1/\mathrm{Im}\,k$), while imposing the aforementioned critical conditions for acoustic cavitation to occur. The results are summarized and compared in Table 3.2.

Table 3.2: Comparison of the wavelength $2\pi/\mathrm{Re}\,k$, penetration depth $1/\mathrm{Im}\,k$, Ω, M_0, M_1, and *Pe*.

K_v / Pa	Wavelength / m	Penetration depth / m	Ω / W·m^{-2}	M_0 / m·s^{-1}	M_1 / s^{-1}	*Pe*
2.4×10^{9}	3.5×10^{-4}	5.8×10^{-5}	1.6×10^{2}	5.5×10^{-3}	1.4×10^{2}	3.0
1.1×10^{10}	2.9×10^{-3}	11	7.2×10^{5}	7.5×10^{-3}	14	5.6
2.4×10^{11}	1.4×10^{-2}	0.38	1.2×10^{5}	3.2×10^{-2}	14	1.0×10^{2}

The first question is: if there are two physically allowed waves, which one will be excited preferentially? The most general solution should be a linear combination of the two waves. However, if $\mathrm{Im}\,k_1 \ll \mathrm{Im}\,k_2$, then on a length scale much greater than $1/\mathrm{Im}\,k_1$, the contribution from the k_1 wave to the general solution is negligible due to its exponential decay. In our case, it's always true that $\mathrm{Im}\,k_1 \ll \mathrm{Im}\,k_2$ when there are two physically allowed waves. Clinically, the more important length scale for brain tissue would be millimeters, where the second wave dominates. The penetration depth of the second wave is much larger than that of the first wave. Additional numerical calculations reveal that the movements of the fluid and the solid phase for the second wave are closer to synchronous than those in the first wave in the sense that the

velocity difference between the two phases in the second wave is much smaller, which allows the wave to propagate further due to reduced friction. In the presence of the second wave, the maximum power input without inducing acoustic cavitation becomes much larger. This can be attributed to the fact that the second wave can carry the mechanical energy much deeper into the medium and thus alleviate local depressurization, which is the cause of acoustic cavitation. It is interesting to note that the intensity levels of ultrasound currently used for therapeutic purposes lie in the range of 5×10^{3} - 3×10^{4} $W\cdot m^{-2}$. The large penetration depth and the large *Pe* number associated with the second wave indicate that mass transport in brain tissue exposed to ultrasound is dominated everywhere by local convection induced by the ultrasound. Due to the importance and profound clinical implications associated with the emergence of the second wave, we urge that more accurate and more extensive experimental studies should be carried out to ascertain mechanical properties of brain tissue under high frequencies.

CHAPTER 4

A COMPUTATIONAL STUDY ON RETRO-CONVECTION-ENHANCED DRUG DELIVERY

4.1 Introduction

It is well-known that blood brain barrier (BBB) can prevent intravenously administered drug from leaving the blood stream and crossing the vascular walls to penetrate into the brain tissue. The potency of most drugs inside the cerebral extracellular space is seriously limited by a variety of physiological barriers, including rapid clearance (Groothuis et al., 2007), non-specific binding, biotransformation (Saltzman et al., 1991), and high intratumor pressure (Chen et al., 1999).

Various approaches have been developed to overcome or circumvent the BBB. Guerin et al. (2004) provided a comprehensive review on local drug delivery by biodegradable polymers implanted in the resection cavity after brain tumor surgery. Rapoport et al. (2000) conducted experiments on osmotic opening of the BBB by intracarotid infusion of a hypertonic arabinose or mannitol solution. Bobo et al. (1994) pioneered convection-enhanced delivery (CED) of large as well as small molecules into the brain by direct intracerebral infusion. Recently, an alternative technique has been invented to overcome the BBB. This method utilizes the inverse procedure of a CED protocol and is thus called R-CED. In R-CED, interstitial fluid (ISF) is withdrawn out of the brain by an inserted needle. The reduction of the ISF pressure generates a significant transendothelial pressure gradient and leads to a significant increase in the bulk flow across the capillary wall into the interstitial space. This bulk flow may lead to an enhanced uptake of

systemically administered therapeutic agents. Currently, there are two ways to reduce the ISF pressure. DiResta et al. (2000) connected a vacuum source to the surgically inserted needle to remove ISF mechanically. Huynh et al. (2007) introduced an implanted microdialysis probe in replace of an ordinary needle to extract fluid from the tissue by using a polymeric osmolyte.

The fluid flow and the mass transfer in the brain tissue have been modeled extensively in the literature for CED (Baxter et al., 1989; Morrison et al., 1994). However, there are few reports on the mathematical modeling of R-CED. In this chapter, we develop a mathematical model to describe the fluid mechanics and mass transfer involved in R-CED. The goal is to use the model to produce quantitative predictions on how relevant physiological parameters can affect drug transport and distribution, what the potentials R-CED have, and how effective R-CED can be. Hopefully, the answers to these questions can help us in the evaluation of R-CED and the creation of better therapeutic strategies.

4.2 Mathematical Model

We assume, for simplicity and mathematical tractability, that the region of brain tissue under investigation is a homogenous, isotropic, rigid, and porous medium (Neeves et al., 2006). We further assume that the fluid flow is in the steady state.

Darcy's law relating the velocity and the pressure gradient is written as

$$\phi \underline{v} = -K \underline{\nabla} p_i \quad (4.1)$$

where ϕ is the tissue porosity, $\underline{v}$ is the fluid velocity, K is the tissue hydraulic permeability, and p_i is the interstitial pressure.

The differential conservation of water (Starling's law) is written as

$$\underline{\nabla} \cdot \left(\phi \underline{v} \right) = L_p s \left(p_0 - p_i \right) \quad (4.2)$$

where L_p is the capillary hydraulic permeability, s is the capillary area per tissue volume, and p_0 is the effective Starling pressure.

Equations (4.1) and (4.2) are closed with respect to $\underline{v}$ and p_i.

The interstitial mass transfer is governed by the mass conservation equation (Baxter et al., 1989; Morrison et al., 1994)

$$\phi\frac{\partial c}{\partial t} = \underline{\nabla}\cdot\left(\phi D\underline{\nabla}c\right) - \underline{\nabla}\cdot\left(\phi c\underline{v}\right) + p_{Ca}sPe_{mv}\cdot\frac{c_0 e^{Pe_{mv}} - c}{e^{Pe_{mv}} - 1} - k_{\mathrm{d}}c \quad (4.3)$$

where c is the interstitial concentration, D is the diffusion coefficient, p_{Ca} is the capillary permeability, c_0 is the plasma concentration of the therapeutic agent under investigation, k_d is the degradation rate constant, and Pe_{mv} is a microvasculature Peclet number defined as

$$Pe_{mv} = \frac{L_p s\left(p_0 - p_i\right)\left(1-\sigma\right)}{p_{Ca}s} \quad (4.4)$$

where σ is the reflection coefficient. Pe_{mv} characterizes the ratio of convective to diffusive flux across the capillary wall.

4.3 Analytical and Numerical Solutions

4.3.1 Analytical Solutions with Spherical Symmetry

In this subsection, we develop an analytical solution for a simple case. This not only provides insights into a special case but also serve the purpose of validating our computer simulation codes for later use. Assume spherical symmetry and position the fluid withdrawal needle at $r = 0$. The boundary conditions for equations (4.1) and (4.2) are

At $r \to \infty$, $p_i \to p_0$ (4.5)

At $r = \zeta$, $4\pi\zeta^2 \phi v_r = Q$ (4.6)

where ζ is radius of the needle, and Q is the volumetric flow rate (For fluid infusion, Q is positive. For fluid withdrawal, Q is negative).

Given these boundary conditions, the analytical expressions for the interstitial pressure and the fluid velocity are found to be (Morrison et al., 1994)

$$p_i = p_0 + \frac{Qe^{\alpha}}{4\pi K(1+\alpha)} \cdot \frac{e^{-\frac{\alpha}{\zeta} \cdot r}}{r} \quad (4.7)$$

$$v_r = \frac{Qe^{\alpha}}{4\pi\phi(1+\alpha)} \left(\frac{1}{r^2} + \frac{\alpha}{\zeta r} \right) e^{-\frac{\alpha}{\zeta} \cdot r} \quad (4.8)$$

where $\alpha = \zeta \sqrt{\frac{L_p s}{K}}$.

In the limit $\alpha \to 0$, equations (4.7) and (4.8) can be simplified to

$$p_i = p_0 + \frac{Q}{4\pi K r} \quad (4.9)$$

$$v_r = \frac{Q}{4\pi\phi r^2} \quad (4.10)$$

The mass transfer equation (4.3) can be written as

$$\phi \frac{\partial c}{\partial t} = \phi D \frac{1}{r^2} \frac{\partial}{\partial r} \left(r^2 \frac{\partial c}{\partial r} \right) - \phi \frac{1}{r^2} \frac{\partial}{\partial r} \left(r^2 c v_r \right) + p_{Ca} s Pe_{mv} \cdot \frac{c_0 e^{Pe_{mv}} - c}{e^{Pe_{mv}} - 1} - k_d c \quad (4.11)$$

or

$$\phi \frac{\partial \tilde{c}}{\partial t} = \phi D \frac{1}{r^2} \frac{\partial}{\partial r} \left(r^2 \frac{\partial \tilde{c}}{\partial r} \right) - \phi \frac{1}{r^2} \frac{\partial}{\partial r} \left(r^2 \tilde{c} v_r \right) + p_{Ca} s Pe_{mv} \cdot \frac{e^{Pe_{mv}} - \tilde{c}}{e^{Pe_{mv}} - 1} - k_d \tilde{c} \quad (4.12)$$

where $\tilde{c} = \frac{c}{c_0}$.

To get an analytical solution, we further assume that $D = 0, k_d = 0, Pe_{mv} \to \infty$. Then we have

Table 4.1: Parameter values used to test the computer simulation codes.

Parameter	Symbol	Value	Reference
Capillary hydraulic permeability	L_p	7.1×10^{-14} $m^3\cdot N^{-1}\cdot s^{-1}$	Neeves et al., 2006; Samtinoranont et al., 2006.
Tissue hydraulic permeability	K	2×10^{-12} $m^4\cdot N^{-1}\cdot s^{-1}$	Samtinoranont et al., 2003; Samtinoranont et al., 2006.
Capillary permeability	p_{Ca}	1×10^{-14} $m\cdot s^{-1}$	Artificial.
Capillary area per tissue volume	s	1×10^{4} m^{-1}	Neeves et al., 2006; Rapoport et al., 2000; Samtinoranont et al., 2006.
Reflection coefficient	σ	0.95	Rapoport et al., 2000.
Tissue porosity	ϕ	0.2	Smith et al., 2007; Zwillinger et al., 2006.
Probe tip radius	ζ	3×10^{-5} m	Artificial.
Diffusion coefficient	D	0	Artificial.
Volumetric fluid flow rate	Q	-1.6×10^{-12} $m^3\cdot s^{-1}$	$0.1\mu L\cdot min^{-1}$ fluid withdrawal rate.
Degradation rate constant	k_d	0	Artificial.

$$\phi\frac{\partial c}{\partial t}=-\phi\frac{1}{r^2}\frac{\partial}{\partial r}\left(r^2cv_r\right)+L_ps\left(p_0-p_i\right)\left(1-\sigma\right)c_0 \quad (4.13)$$

Plug equations (4.7) and (4.8) into equation (4.13). After some straightforward algebra, we get

$$\frac{\partial\tilde{c}}{\partial t}=-\frac{Q}{4\pi\phi r^2}\frac{\partial\tilde{c}}{\partial r}-\frac{L_ps\left(1-\sigma\right)Q}{4\pi\phi Kr} \quad (4.14)$$

where $\tilde{c} = \frac{c}{c_0}$.

Equation (4.14) is a quasi-linear partial differential equation and can be solved explicitly by the method of characteristics (Saltzman et al., 1991). The solution compatible with zero initial concentration and zero concentration gradient at the origin and at infinity is

$$\tilde{c} = \int_{-t}^{0} \frac{L_p s(1-\sigma)(-Q)}{4\pi\phi K\left(r^3 + \frac{3Qw}{4\pi\phi}\right)^{\frac{1}{3}}} dw \quad (4.15)$$

4.3.2 Validation of Computer Simulation Codes

Equation (4.12) with p_i and v_r given by equations (4.7) and (4.8) can be numerically integrated by a solver in MATLAB 7.0.4. In order to test our computer simulation codes, we choose a set of parameter values listed in Table 4.1 so that we can directly compare the numerical results with those calculated from equation (4.15). In our simulation codes, we have imposed the initial condition of zero concentration and the boundary conditions of zero concentration gradient at $r = \zeta$ and at infinity. Numerical simulations for the dimensionless concentration $\tilde{c}$ were carried out. The results from simulations are found to match the analytical solutions with an error of 3% within r = 0.3 cm and up to t = 20 min (See Figure 4.1) and an error of 5% up to t = 60 min.

4.3.3 Numerical Simulations with Axisymmetry

In a more practical and more patient-friendly R-CED procedure, the fluid is removed by a

microdialysis tube (Huynh et al., 2007). Usually, the length of the tube is large compared to its radius. For such a situation, axisymmetry is a better

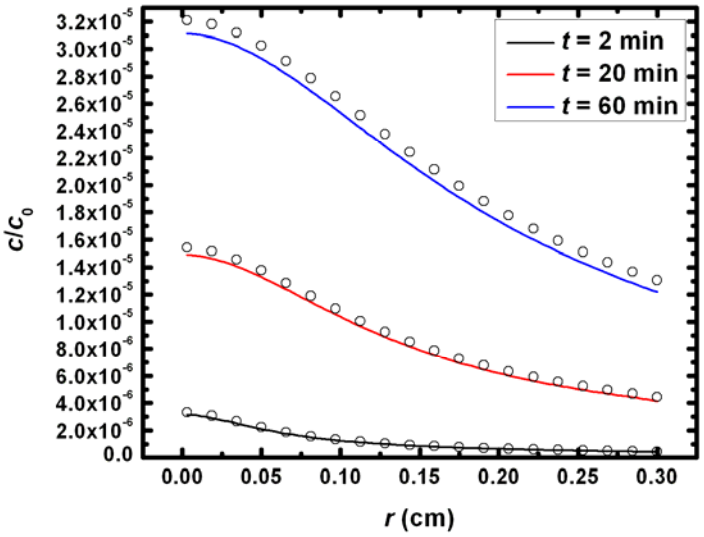

Figure 4.1: Comparison of analytical solutions and numerical solutions of the dimensionless concentration. Dots represent numerical solutions while circles represent analytical solutions.

approximation than spherical symmetry. However, it's impossible to get an analytical solution for the concentration with axisymmetry. Due to the similarities between spherical symmetry and axisymmetry, we only need to slightly modify the computer simulation codes to accommodate the symmetry of the problem and still have confidence in the validity of the codes. In a cylindrical coordinate system, we position the axis of the microdialysis tube on the line $r = 0$. For the axisymmetric case, the analogs of equations (4.7), (4.8) and (4.12) are

$$p_i = p_0 + \frac{Q}{2\pi K \alpha K_1(\alpha)} \cdot K_0\left(\frac{\alpha}{\zeta} r\right) \quad (4.16)$$

where $K_q(\cdot)$ is the second kind modified Bessel function of order q, Q is the flow rate per unit

length along the z direction and ζ is the outer radius of the microdialysis tube.

$$v_r = \frac{Q}{2\pi\phi\zeta K_1(\alpha)} \cdot K_1\left(\frac{\alpha}{\zeta} r\right) \quad (4.17)$$

$$\phi\frac{\partial \tilde{c}}{\partial t} = \phi D \frac{1}{r}\frac{\partial}{\partial r}\left(r\frac{\partial \tilde{c}}{\partial r}\right) - \phi\frac{1}{r}\frac{\partial}{\partial r}\left(r\tilde{c}v_r\right) + p_{Ca}sPe_{mv} \cdot \frac{e^{Pe_{mv}} - \tilde{c}}{e^{Pe_{mv}} - 1} - k_d\tilde{c} \quad (4.18)$$

At infinity, there is no convective flux, no diffusive flux, and thus no net flux. At the surface of the microdialysis probe, the boundary condition is complicated and depends on the property of the dialysis membrane. If the membrane is completely permeable to the drug molecules (Note that the membrane should always be impermeable to the dialysate), the total flux across the membrane under high withdrawal flow rate is equal to the convective flux, i.e. the diffusive flux is negligible. If the membrane is impermeable to the drug molecules, the total flux is zero. If the membrane is semipermeable to the drug molecules (By "semipermeable", we mean that the drug molecules are able to pass through the membrane, but there is some mass transfer resistance across the membrane), the boundary conditions depends on the mass transfer inside the micordialysis tube. In the following we discuss these three boundary conditions separately.

① Completely Permeable Membrane

Zero diffusive flux leads to the boundary condition of

At $r = \zeta$, $\frac{\partial c}{\partial r} = 0$ (4.19)

or

At $r = \zeta$, $\frac{\partial \tilde{c}}{\partial r} = 0$ (4.20)

② Impermeable Membrane

Zero total flux leads to the boundary condition of

Table 4.2: Parameter values used to simulate the case with axisymmetry.

Parameter	Symbol	Value	Reference
Capillary hydraulic conductivity	L_p	7.1×10^{-14} $m^3\cdot N^{-1}\cdot s^{-1}$	Neeves et al., 2006; Samtinoranont et al., 2006
Tissue hydraulic conductivity	K	2×10^{-12} $m^4\cdot N^{-1}\cdot s^{-1}$	Samtinoranont et al., 2003; Samtinoranont et al., 2006
Capillary permeability	p_{Ca}	1.1×10^{-11} $m\cdot s^{-1}$	Neeves et al., 2006
Capillary area per tissue volume	s	1×10^{4} m^{-1}	Neeves et al., 2006; Rapoport et al., 2000; Samtinoranont et al., 2006
Reflection coefficient	σ	0.95	Rapoport et al., 2000
Tissue porosity	ϕ	0.2	Smith et al., 2007; Zwillinger et al., 2006
Outer radius of the microdialysis tube	ζ	2.5×10^{-4} m	Morrison et al., 1994
Diffusion coefficient	D	1×10^{-11} $m^2\cdot s^{-1}$	Neeves et al., 2006
Flow rate per unit length along the z direction	Q	-8×10^{-10} $m^2\cdot s^{-1}$	$0.1\mu L\cdot min^{-1}$ fluid withdrawal rate for a 0.2-cm long microdialysis membrane
Degradation rate	k_d	0	No degradation

At $r = \zeta$, $D\frac{\partial c}{\partial r} - cv_r = 0$ (4.21)

or

At $r = \zeta$, $D\frac{\partial \tilde{c}}{\partial r} - \tilde{c}v_r = 0$ (4.22)

③ Semipermeable Membrane

In general, it's very difficult to specify an appropriate boundary condition for a semipermeable membrane. To simplify the problem, we impose the following boundary conditions,

At $r = \zeta$, $D\frac{\partial c}{\partial r} - cv_r = -fcv_r$ (4.23)

or

At $r = \zeta$, $D\frac{\partial \tilde{c}}{\partial r} - \tilde{c}v_r = -f\tilde{c}v_r$ (4.24)

Here $0 \le f \le 1$. $f = 0$ corresponds to impermeable membrane and $f = 1$ corresponds to completely permeable membrane. In the following calculations, we take *f* to be 0.5 for a semipermeable membrane for demonstrational purposes.

We use the parameter values listed in Table 4.2 to solve for $\tilde{c}$ as a function of *t* and *r* (Figure 4.2 – 4.4) for the three types of membranes.

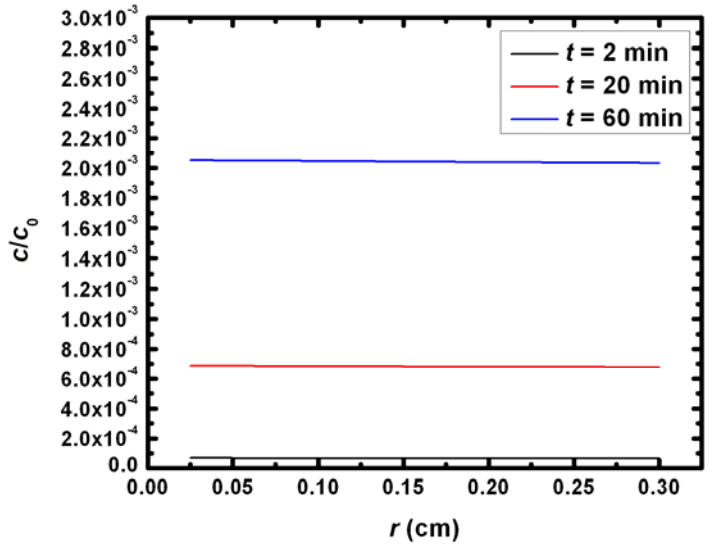

Figure 4.2: Dimensionless concentration profile for completely permeable membrane.

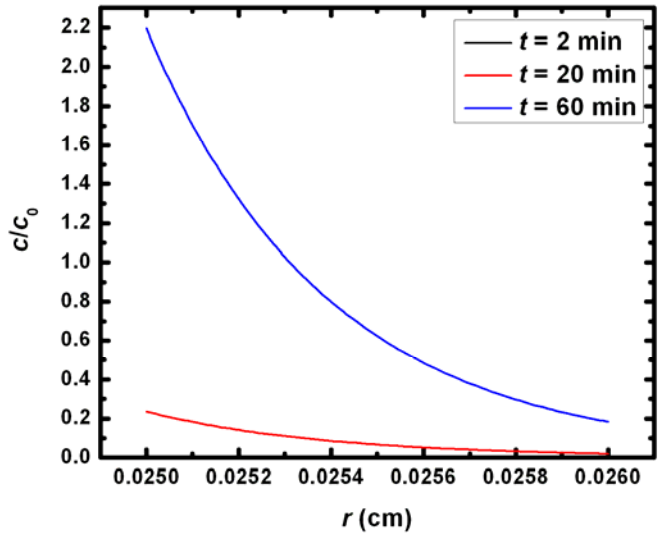

Figure 4.3: Dimensionless concentration profile for impermeable membrane.

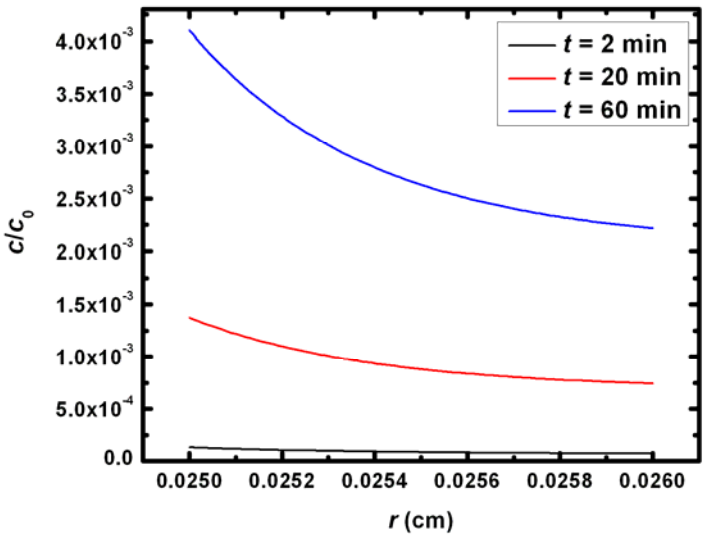

Figure 4.4: Dimensionless concentration profile for semipermeable membrane.

4.4 Sensitivity Analysis

At the current stage, we still lack experimental data for direct comparison with theoretical predictions. Yet the mathematical model can be used to carry out a sensitivity analysis on the various parameters involved. The utility of sensitivity analysis lies in the fact that a system is sometimes more sensitive to change in one parameter than another. Tissue properties such as capillary permeability and reflection coefficient can vary, depending on physiological conditions, e.g. healthy tissue or malignant tumor. The pharmacodynamics such as diffusion and elimination can vary, depending on the properties of the drug molecules, e.g. molecular size, surface coating. We choose p_{Ca}, σ, D, k_d, K, and Q as the varied parameters and plot the dimensionless concentration profile for an impermeable membrane at a single time point t = 60 min (Figure 4.5 – 4.10).

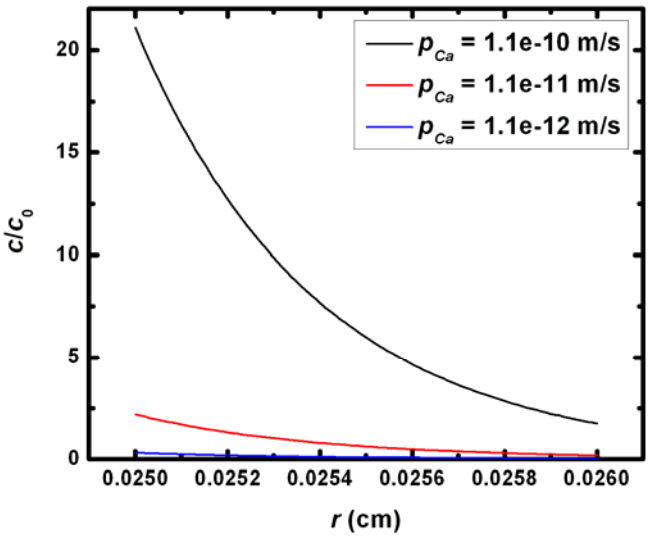

Figure 4.5: Dimensionless concentration profile at t = 60 min for different values of capillary permeability p_{Ca}. Baseline values are listed in Table 4.2.

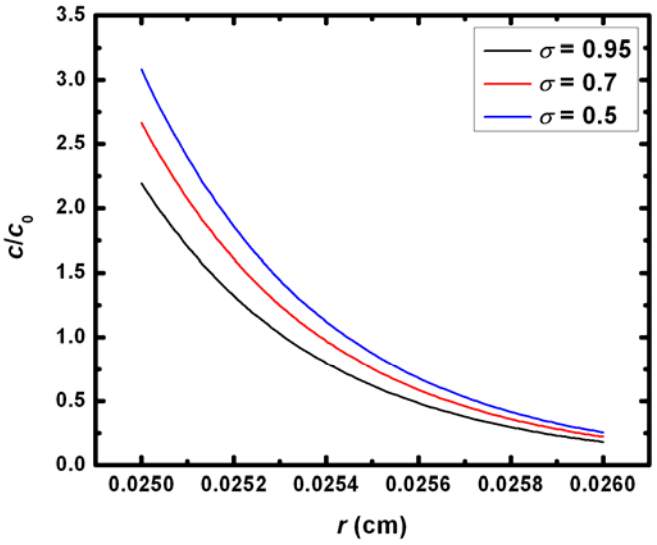

Figure 4.6: Dimensionless concentration profile at t = 60 min for different values of reflection coefficient σ. Baseline values are listed in Table 4.2.

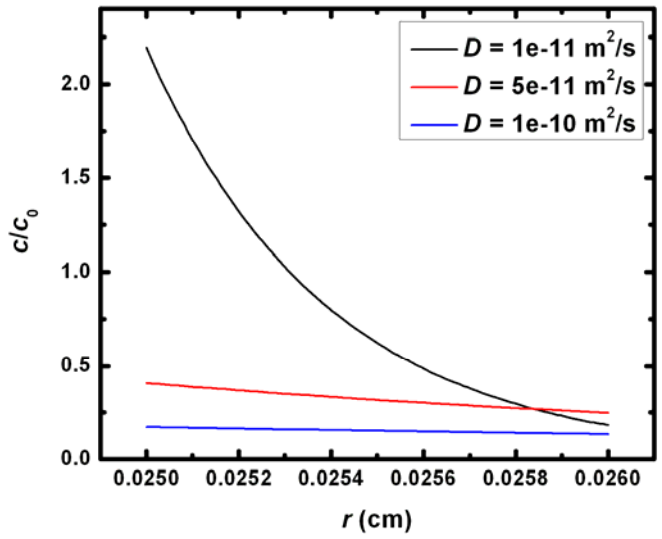

Figure 4.7: Dimensionless concentration profile at t = 60 min for different values of diffusion coefficient D. Baseline values are listed in Table 4.2.

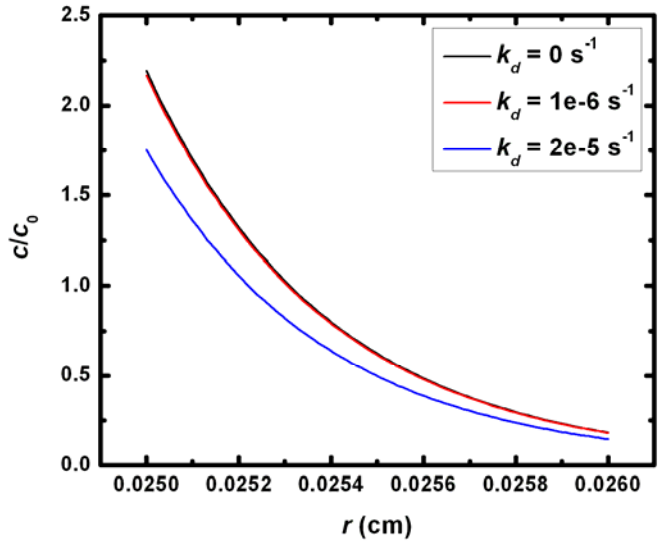

Figure 4.8: Dimensionless concentration profile at t = 60 min for different values of degradation rate constant k_d. Baseline values are listed in Table 4.2.

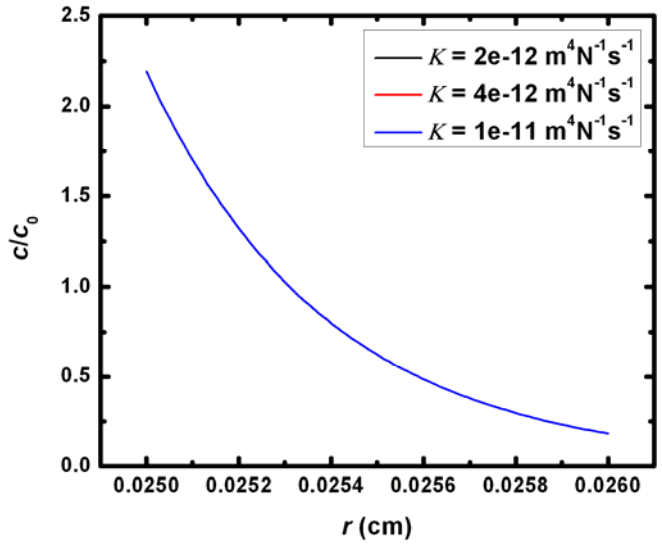

Figure 4.9: Dimensionless concentration profile at t = 60 min for different values of tissue hydraulic conductivity K. Baseline values are listed in Table 4.2.

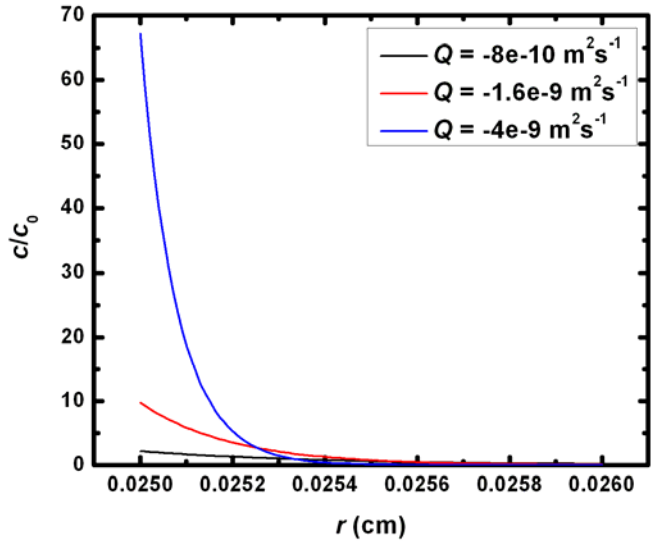

Figure 4.10: Dimensionless concentration profile at t = 60 min for different values of fluid withdrawal rate Q. Baseline values are listed in Table 4.2.

4.5 Results and Discussion

First, let us have a quick look at the fluid flow issues involved in this problem. Pressure and velocity distributions in the interstitium calculated from equations (4.16) and (4.17) for three different fluid withdrawal rates with baseline parameter values listed in Table 4.2 are shown in Figure 4.11 – 4.12. For any given position, the effective pressure p_0-p_i as well as the magnitude of the fluid velocity $-v_r$ is directly proportional to the fluid withdrawal rate. From Figure 4.11 – 4.12 we can see that for the nominal fluid withdrawal rate of 0.1 μL/min, the effective pressure is 200 Pa at r = 0.3 cm and the interstitial fluid velocity is 1.6×10^{-5} cm/s, which are not insignificant. The pressure and velocity distributions are independent of the drug properties, especially whether the drug molecules can pass through the microdialysis membranes or not. The fluid mechanics in R-CED is similar to that in CED, governed by Darcy's

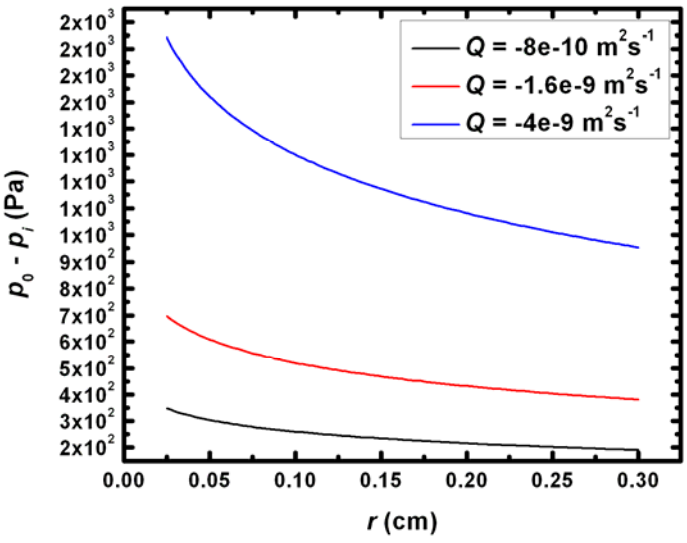

Figure 4.11: Distribution of interstitial pressure.

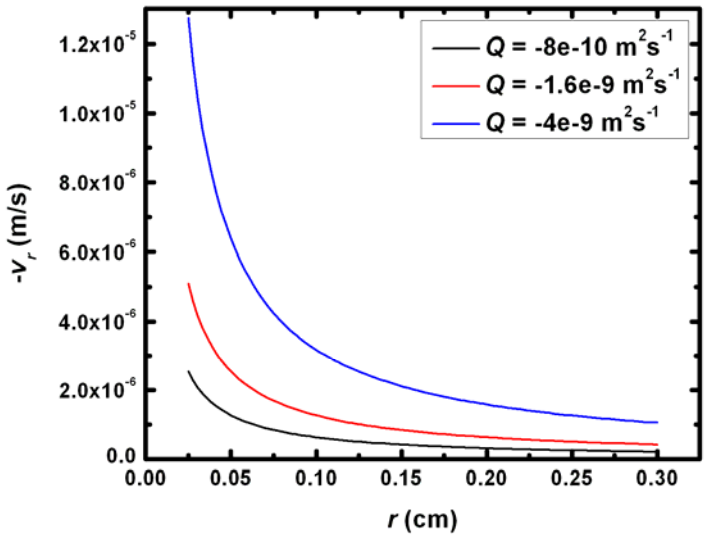

Figure 4.12: Distribution of interstitial velocity.

law and Starling's law.

Now let us turn to the mass transfer issues. The microdialysis membrane separates the ISF and the dialysate solution. Water is allowed to pass freely across the membrane. If the membrane is completely permeable to the drug molecules, we can get a rather homogeneous drug distribution up to 0.3 cm away from the probe (Figure 4.2). But the concentration in the interstitium is only several thousandths of that in the blood since most of the drug molecules are drained away by the probe and get wasted. If the membrane is impermeable to the drug molecules, the drug molecules accumulate near the probe and the concentration quickly builds up (Figure 4.3). If the membrane is semipermeable, the situation sits in between as expected (Figure 4.4). The concentration profiles are indirect reflections of the permeability of the microdialysis membranes.

Since an impermeable membrane is most favorable for drug delivery purposes, we make a detailed sensitivity analysis for this type of membrane. We examine the concentration profiles

at a single time point of t = 60 min (Figure 4.5 – 4.10). All trends observed are consistent with intuitive arguments. An increase in capillary permeability or a decrease in reflection coefficient tends to increase the drug concentration in the intersitium. Smaller diffusion coefficients tend to sharpen the concentration profile. In Figure 4.7, notice that the benefit of having a larger diffusion coefficient is that the distribution of the drug molecules is more uniform, but the penalty is that the absolute value of the concentration becomes smaller. A small degradation rate constant has almost no effect on drug distribution while a large degradation rate constant lowers the interstitial drug concentration to certain extent. Higher fluid withdrawal rates tend to accumulate more drug molecules near the probe tip. It is a little bit surprising that drug distribution is rather insensitive to the value of tissue hydraulic permeability since all three curves in Figure 4.9 actually overlap each other. In R-CED, the resistivity to fluid flow by capillary walls and interstitial structures are connected in parallel and the resistivity is dominated by capillary walls. Therefore tissue hydraulic permeability becomes much less important.

Finally, we would like to compare R-CED with CED in detail. In a CED protocol, drug containing fluid is directly infused into brain tissue through an inserted catheter. The drug delivery source is located at a single point corresponding to the tip of the infusion catheter. Since drug molecules do not have to pass across the capillary walls, the BBB is circumvented. Under high infusion rate, forced convection of ISF in the interstitium is the dominant drug distribution mechanism near the infusion point. Compared to diffusion, convection has been shown to be able to significantly increase the drug distribution volume. An eminent and long-existing problem associated with CED is the so-called “backflow” problem. Brain tissue is a poroelastic medium. Since there is usually no contact stress between the infusion catheter and the tissue at the infusion point, the adjacent tissue is free to move away from the catheter during infusion. This movement of the tissue is the cause of reflux of infused solution along the catheter-tissue

interface and the phenomena is called backflow. This is the cause of many treatment induced complications in CED. Backflow leads to poor control over the fate of infused drugs which often end up in healthy tissue. An immediate advantage of the R-CED therapy is that the backflow problem does not exist in R-CED. The direction of the fluid velocity is opposite to that in CED. The fluid is sucked toward the microdialysis probe. As a result, tissue adjacent to the probe surface tends to move toward that surface and be kept in intimate contact with that surface. However, drug molecules do need to pass the BBB in R-CED although to some extent the BBB is weakened by pressure gradients across the capillary walls. Also notice that the drug delivery source is provided by efflux of fluid from the blood vessels into the interstitium and is thus continuously distributed within the tissue. We have already seen that mass transfer pathways and mechanisms are quite different in CED and R-CED. From previous discussions, we have seen that R-CED is effective in generating convections in the interstitium, no less effective than CED. But effective fluid flow does not necessarily translate into effective mass transfer. In R-CED, the drug concentration profile depends on the choice of microdialysis membranes. For a completely permeable membrane, the drug distribution is uniform all the time over a large distance but stays at a fairly low level in the interstitium. This immediately raises concerns on drug toxicities in the blood. For a completely impermeable membrane, there is a sharp change in the interstitial drug concentration near the fluid withdrawal point. Although the drug concentration might even exceed that in the blood near the withdrawal point, the affected volume is rather small, which can be attributed to low tissue hydraulic permeability, low capillary hydraulic permeability, and high reflection coefficient. There are uncertainties in the values of these parameters. Previous tissue hydraulic permeability measurements are mainly based on a CED-like methodology, which may underestimate tissue hydraulic permeability due to backflows. Capillary hydraulic permeability and/or reflection coefficient may change when there is significant bulk flow across capillary

walls (e.g. change of pore size, significant disruption of endothelial cells). These uncertainties are associated with the fundamental mechanical properties of brain tissues and deserve to be studied both experimentally and theoretically in further details.

CHAPTER 5

NANOPARTICLE TRANSPORT IN THE BRAIN

5.1 Introduction

Delivery of high-molecular-weight therapeutic compounds and nanoparticle drug carriers into a clinically relevant volume of tissue is of particular challenge in the central nervous system (CNS) due to the presence of the blood brain barrier (BBB). It has been demonstrated in small animal studies that intrathecal, intraventricular, intravascular, and acute parenchymal injections can distribute nanoparticles to limited volumes in the brain tissue (Mannes et al., 1998; Muldoon et al., 1995; Oldendorf et al., 1974). Intravascular delivery has the simplest procedure and is the least invasive delivery approach. Nevertheless, this method fails to deliver into the brain, because channels in the BBB are so small that even the passage of small macromolecules is inhibited, let alone nanoparticles. Additionally, this technique does not target a specific region of the brain. The effectiveness of intrathecally and intraventricularly injected therapeutic agents is limited by diffusion. It has been reported that small molecules such as sucrose can penetrate a few millimeters into the brain tissue (Fenstermacher et al., 1974; Groothuis et al., 1999; Morrison et al., 2001). However, high-molecular-weighted or large-sized therapeutic agents (e.g. unmetabolized proteins, gene-carrying vectors) suffer a sharp loss of concentration beyond the CSF-tissue interface (Fenstermacher et al., 1974; Morrison et al., 2001; Muldoon et al., 1995). As a result, intravascular, intrathecal, and intraventricular injections have not been very successful in the clinical setting of the treatment of brain disorders. Another approach that may enhance the distribution of nanoparticles in brain tissue is convection-enhanced delivery (CED).

Unlike diffusion, which relies on a concentration gradient, CED relies on the bulk flow to carry therapeutic agents through the extracellular space. CED is not restricted by BBB and can achieve a relatively homogeneous concentration distribution of the infused compounds in a relatively large volume of distribution (Bobo et al., 1994; Broaddus et al., 1998; Chen et al., 1999; Laske et al., 1997; Morrison et al., 1994; Neeves et al., 2006). Furthermore, by delivering the complete dose at the target site, smaller quantities may be administered than required for systemic dosing, thus reducing systemic exposure and toxicity. This method of delivery is also able to carry nanoparticles significantly farther than using diffusion alone.

On the theoretical side, a large amount of work has been carried out to analyze the fluid mechanics and mass transfers involved in CED (Basser 1992; Baxter et al., 1989; Morrison et al., 1994; Netti et al., 1997; Netti et al., 2003). The distribution of small molecules, which are treated as tracers in the fluid, is relatively well-understood from these previous studies. The given assumption is that the hydrodynamic interactions between the small molecules and the carrying fluid are negligible. However, this assumption is no longer valid when applied to nanoparticles. Previous CED experiments have shown that the distribution and transport of nanoparicles in the brain is different from small molecules. In this chapter, we present a simple mathematical model to describe the transport behavior of nanoparticles in CED. This model explicitly takes the hydrodynamic interactions between the nanoparticles, the carrying fluid, and the brain tissue into account. Using this model, we are able to show how the volume of distribution is dependent on the sizes and surface properties of the infused nanoparticles.

5.2 Mathematical Model

We assume, for simplicity and mathematical tractability, that the region of brain tissue

under investigation is a homogenous, isotropic, rigid, and porous medium. We also ignore the size distribution of the infused nanoparticles.

Mass conservation for the fluid phase is written as

$$\frac{\partial}{\partial t}\left(\phi - nV_p\right) + \underline{\nabla} \cdot \left[\left(\phi - nV_p\right)\underline{v_f}\right] = 0 \quad (5.1)$$

where ϕ is the porosity, n is the nanoparticle number density, V_p is the volume per nanoparticle, and v_f is the fluid velocity.

Mass conservation for the nanoparticle phase is written as

$$R\frac{\partial n}{\partial t} + \underline{\nabla} \cdot \left(n\underline{v_p}\right) = 0 \quad (5.2)$$

where R is the retardation factor (Morrison et al., 1994), and v_p is the nanoparticle velocity. R takes non-hydrodynamic-interactions (e.g. fluid exchange between the intracellular space and the extracellular space, linear bindings) into account.

Momentum conservation for the fluid phase is written as

$$\rho_f\left(\frac{\partial}{\partial t} + \underline{v_f} \cdot \underline{\nabla}\right)\underline{v_f} = -\underline{\nabla}p - \frac{\left(\phi - nV_p\right)\mu}{\kappa}\underline{v_f} - \frac{\left(\phi - nV_p\right)\mu n V_p}{\kappa_p}\left(\underline{v_f} - \underline{v_p}\right) \quad (5.3)$$

where ρ_f is the density of the fluid, p is the pressure, μ is the viscosity of the fluid, κ is the Darcy permeability of the medium, and κ_p is the analog of κ for the nanoparticle phase. κ_p depends on the size and geometry of the nanoparticle.

Momentum conservation for the nanoparticle phase is written as

$$\rho_p V_p\left(\frac{\partial}{\partial t} + \underline{v_p} \cdot \underline{\nabla}\right)\underline{v_p} = -\mu f\left(\underline{v_p} - G\underline{v_f}\right) \quad (5.4)$$

where ρ_p is the density of the nanoparticle, f is the drag constant, and G is the lag coefficient(Anderson et al., 1974). In general, f depends on the size and geometry of the nanoparticle. G depends on the size and geometry of the nanoparticle as well as the pore size and

geometry of the medium. Equations (5.1)-(5.4) have explicitly included terms representing hydrodynamic interactions between the nanoparticles, the carrying fluid, and the porous medium.

To get an analytical solution, we introduce two approximations: inertia-free approximation and dilute-suspension approximation. The first approximation allows us to set ρ_f and ρ_p to be zero and the second approximation allows us to set nV_p to be zero. Equations (5.1)-(5.4) are simplified to

$$\underline{\nabla} \cdot \underline{v_f} = 0 \quad (5.5)$$

$$R\frac{\partial n}{\partial t} + \underline{\nabla} \cdot \left(n\underline{v_p} \right) = 0 \quad (5.6)$$

$$\underline{\nabla} p = -\frac{\phi \mu}{\kappa} \underline{v_f} \quad (5.7)$$

$$\underline{v_p} = G\underline{v_f} \quad (5.8)$$

The fluid mechanics part and the mass transfer part of the problem get decoupled thanks to the above-mentioned approximations. The fluid mechanics part can be determined by solving equations (5.5), (5.7), and (5.8) simultaneously. The mass transfer part can be determined by solving equation (5.6) with the solution of the fluid mechanics part. Note that there are no time derivatives in equations (5.5), (5.7) and (5.8). Therefore the solutions for p, v_f and v_p will be steady-state if the boundary conditions are time-independent. We examine two kinds of time-independent boundary conditions in detail (Basser 1992).

① Infusion from a constant pressure source

In this case, it is assumed that fluid is infused into the porous medium through a spherical cavity of radius b which is maintained at a constant pressure P_0.

Since the boundary condition is time-independent, equation (5.5) can be simplified to

$$\frac{1}{r^2}\frac{d}{dr}\left(r^2 v_{fr}\right) = 0 \quad (5.9)$$

Integrating once, we get

$$v_{fr} = \frac{A}{r^2} \quad (5.10)$$

where A is an unknown constant. With v_{fr} given by equation (5.10), the r component of equation (5.7) can be integrated,

$$p = \frac{\phi\mu}{\kappa}\cdot\frac{A}{r} + B \quad (5.11)$$

where B is an unknown constant.

One of the boundary conditions for p is that p should vanish at infinity. Therefore

$$p = \frac{\phi\mu}{\kappa}\cdot\frac{A}{r} \quad (5.12)$$

The other boundary condition, $p = P_0$ at $r = b$, sets the integration constant A to be

$$A = \frac{\kappa b P_0}{\phi\mu} \quad (5.13)$$

Therefore

$$v_{fr} = \frac{\kappa b P_0}{\phi\mu r^2} \quad (5.14)$$

Equation (5.8) tells us that

$$v_{pr} = \frac{G\kappa b P_0}{\phi\mu r^2} \quad (5.15)$$

Plug equation (5.15) into equation (5.6),

$$\frac{\partial n}{\partial t} + \frac{G\kappa b P_0}{R\phi\mu r^2}\cdot\frac{\partial n}{\partial r} = 0 \quad (5.16)$$

The initial and boundary conditions for n are

At $t = 0$, $n = 0$; at $r = b$, $n = n_0$; at $r \to \infty$, $n = 0$.

The solution is

$$n = \begin{cases} n_0 \quad \text{if } b \le r \le \left(\dfrac{3G\kappa b P_0 t}{R\phi\mu} + b^3 \right)^{\frac{1}{3}} \\ 0 \quad \text{if } r > \left(\dfrac{3G\kappa b P_0 t}{R\phi\mu} + b^3 \right)^{\frac{1}{3}} \end{cases} \quad (5.17)$$

② Infusion from a constant flow source

In this case, it is assumed that fluid is infused from a constant flow source Q_0.

Again, we have equation (5.10), with the integration constant A to be determined by the following boundary condition,

$$Q_0 = \phi \iint_{r=b} \underline{v_f} \cdot \underline{dS} \quad (5.18)$$

Note that equation (5.18) is consistent with our dilute-suspension approximation.

A is found to be

$$A = \frac{Q_0}{4\pi\phi} \quad (5.19)$$

Therefore

$$v_{fr} = \frac{Q_0}{4\pi\phi r^2} \quad (5.20)$$

Equation (5.8) tells us that

$$v_{pr} = \frac{GQ_0}{4\pi\phi r^2} \quad (5.21)$$

Plug equation (5.21) into equation (5.6),

$$\frac{\partial n}{\partial t} + \frac{GQ_0}{4\pi R\phi r^2} \cdot \frac{\partial n}{\partial r} = 0 \quad (5.22)$$

The initial and boundary conditions for n are

At $t = 0$, $n = 0$; at $r = b$, $n = n_0$; at $r \to \infty$, $n = 0$.

The solution is

$$n = \begin{cases} n_0 \quad \text{if } b \le r \le \left(\dfrac{3GQ_0 t}{4\pi R\phi} + b^3 \right)^{\frac{1}{3}} \\ 0 \quad \text{if } r > \left(\dfrac{3GQ_0 t}{4\pi R\phi} + b^3 \right)^{\frac{1}{3}} \end{cases} \quad (5.23)$$

It can be shown that the two kinds of boundary conditions discussed above are equivalent to each other with $P_0 = \mu Q_0 / 4\pi\kappa b$.

5.3 Results and Discussion

Since constant flow rate infusion is equivalent to constant pressure infusion, we only discuss constant flow rate infusion. According to equation (5.23), the nanoparticle number density profile at any given time is step-like. There is a clear boundary beyond which the nanoparticle number density is zero and within which the distribution is uniform. The moving wave front has an explicit expression as

$\left(\dfrac{3GQ_0 t}{4\pi R\phi} + b^3 \right)^{\frac{1}{3}}$ and the corresponding volume of distribution V_d is $\dfrac{4}{3}\pi \left(\dfrac{3GQ_0 t}{4\pi R\phi} + b^3 \right)$.

In typical convection enhanced delivery experiments, b is very small and can be neglected. V_d is simplified to $\dfrac{GQ_0 t}{R\phi}$. If we define the volume of infusion V_i as $Q_0 t$, then

$$V_d = \frac{G}{R\phi} V_i \quad (5.24)$$

This equation indicates that the volume of distribution V_d is directly proportional to the lag coefficient G and inversely proportional to the retardation factor R. If the particles have

unrestricted mobility, i.e. the particles are small enough to behave as tracers in the fluid, then both G and R are unity. $V_d = V_i / \phi$, which is a well-known relation for free-moving small molecules. If the particles are subject to linear bindings, then $R = 1 + k_{b1} B_0 / k_{b2}$, where B_0 is the concentration of binding sites and k_{b1} / k_{b2} is the affinity constant on an extracellular space basis (Morrison et al., 1994). In this case, R is greater than one and the wave front of the particle distribution is retarded. The value of R reflects surface properties of the particles and non-hydrodynamic interactions between the particles and the medium. We further assume that R has a functional dependence on the particle radius a (assuming spherical shape) by $R = 1 + c_s a^2$, where c_s is a constant. This means that we assume that the retardation effect R-1 is proportional to the surface area of the particle. The proportionality constant c_s depends on the surface properties of both the particles and the medium. The lag coefficients have been studied in detail for several situations (Happel et al., 1973). For a sphere with radius a moving in the center of a circular cylindrical tube with radius a_t, the lag coefficient G is given by $1 - 2a^2 / 3a_t^2$. It is interesting to notice that a sphere whose radius is as large as that of the tube could still have a non-zero lag coefficient of 1/3. In the context of our theory, G is given by $1 - 2a^2 / 3R_0^2$, where R_0 is the equivalent radius of the micro-channel in the porous medium. Plugging the expressions for the retardation factor R and the lag coefficient G into equation (5.24), we get

$$V_d = \frac{1 - \dfrac{2a^2}{3R_0^2}}{1 + c_s a^2} \cdot \frac{V_i}{\phi} \quad (5.25)$$

This equation indicates that the volume of distribution V_d has a complicated functional dependence on the particle radius a.

We compare our mathematical model with some experimental results conducted on brain tissues. Chen et al. (2005) investigated the influence of sizes and surface properties of infused

nanoparticles on their distributions within the brain by convection enhanced delivery. It was found that surface properties as well as sizes could significantly alter nanoparticle distributions. A prominent example is that bovine serum albumin (BSA) coating on the infused nanoparticles can greatly enhance the distribution by preventing hydrophobic interactions between the particles and the extracellular matrix. The fact that BSA, a 7-nm-diameter macromolecule, can be freely distributed in the extracellular space is reflected in the satisfaction of the relation $V_d = V_i / \phi$. These facts indicate that BSA is an ideal coating and, to a first approximation, nanoparticles coated with BSA can be assumed to have unity retardation factors (i.e. no surface interactions). Setting c_s to be zero in equation (5.25), we have

$$V_d = \left(1 - \frac{2a^2}{3R_0^2}\right) \cdot \frac{V_i}{\phi} \quad (5.26)$$

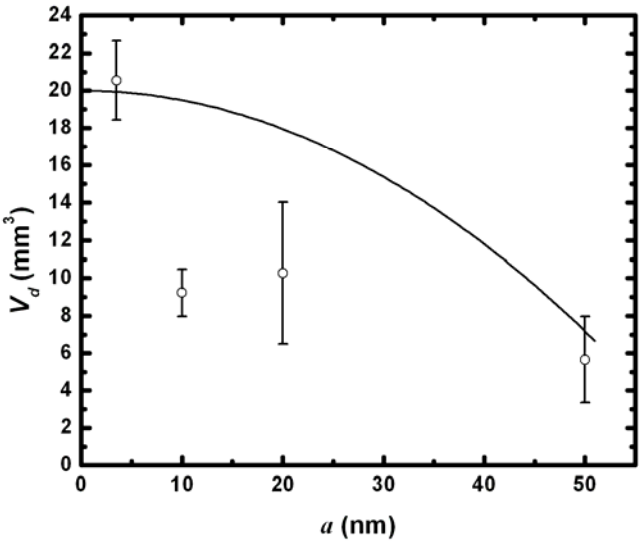

Figure 5.1: Plot of volume of distribution V_d as a function of nanoparticle radius a using equation (5.26). Nanoparicles are coated with BSA.

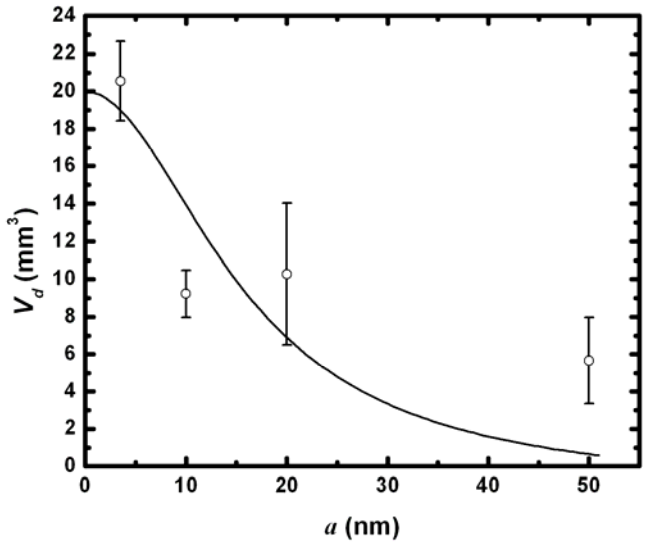

Figure 5.2: Plot of volume of distribution V_d as a function of nanoparticle radius a using equation (5.25). Nanoparicles are coated with BSA.

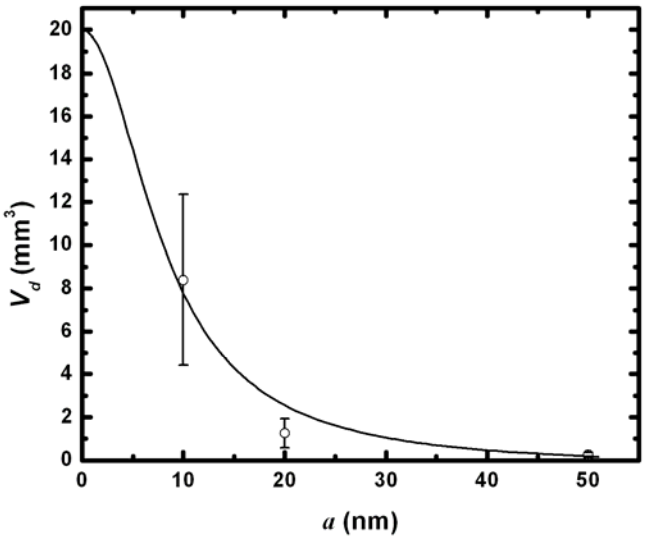

Figure 5.3: Plot of volume of distribution V_d as a function of nanoparticle radius a using equation (5.25). Nanoparicles are not coated with BSA.

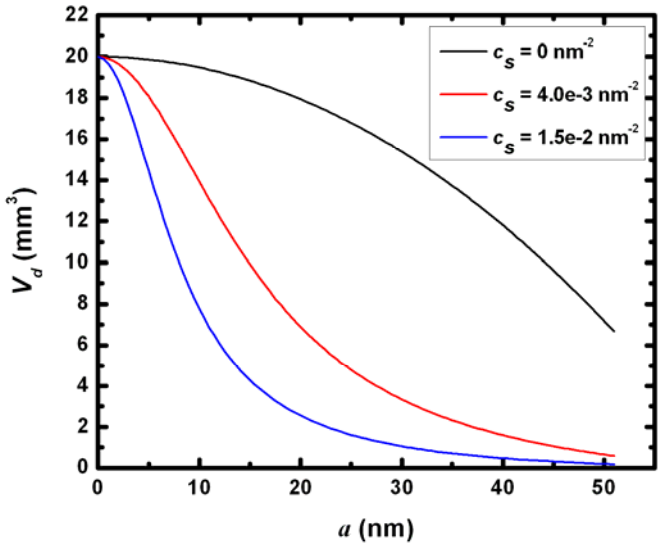

Figure 5.4: Plot of volume of distribution V_d as a function of nanoparticle radius a using equation (5.25) with three different c_s values.

Equation (5.26) is applicable to BSA coated nanoparticles. This equation indicates that the volume of distribution V_d has a quadratic dependence on the nanoparticle radius a. The porosity ϕ is taken to be 0.2. R_0 was estimated to be 38-64 nm by previous experiments (Throne et al., 2006) and is set to be 51 nm in the following calculations. Figure 5.1 shows the correlation between particle size and volume of distribution of nanoparticles with BSA coating. Dots represent experimental data while lines represent predictions from equation (5.26). Note that there are no free fitting parameters involved in the predictions from equation (5.26). Thus, it is not surprising that the results only show limited success. If we assume that there are still residual surface interactions even after coating the nanoparticles with BSA, we need to use equation (5.25) with a non-zero c_s. Figure 5.2 shows the correlation by introducing the free fitting parameter c_s appearing in equation (5.25). We get $c_s = 4.0\times10^{-3}$ nm^{-2} for nanoparticles with BSA

coating. The general trend exhibited by the experimental data is able to be reproduced in Figure 5.2. For nanoparticles without BSA coating, surface interactions are significant and the retardation factors are not unity. Figure 5.3 shows fitting of the experimental data to equation (5.25). We get $c_s = 1.5\times10^{-2}$ nm^{-2} for nanoparticles without BSA coating. Again, the general trend exhibited by the experimental data is able to be reproduced. The value of c_s for nanoparticles with BSA coating is four times larger than nanoparticles without BSA coating. For comparison, Figure 5.4 plots three curves generated from equation (5.25) with $c_s = 0$, 4.0×10^{-3}, and 1.5×10^{-2} nm^{-2}, respectively. The three curves converge as the nanoparticle radius approaches zero. As we can see, both the surface properties and sizes of the nanoparticles can significantly affect their volumes of distribution.

CHAPTER 6

MODELING OF CEREBRAL MICROHEMORRHAGE

6.1 Introduction

It is estimated that 780,000 strokes occur in the United States every year. Stroke is the leading cause of adult disability in the United States and is the number two cause of death (Feigin et al., 2005). There are two types of strokes: ischemic and hemorrhagic. Thirteen percent of stroke cases are hemorrhagic. Cerebral hemorrhages account for 30–60% of hospital admissions for stroke (Yadav et al., 2007). A cerebral hemorrhage is an intra-axial hemorrhage; that is, it occurs within the brain tissue rather than outside of it. It has a high mortality rate. Besides, recent evidence has suggested a link between microhemorrhage and cognitive decline in humans (Haller et al., 2010).

The physiological impacts due to microhemorrhages have been studied in animal models using pigs, rabbits, dogs, cats, and rodents. The bleed is usually created in the striatum, but other regions have been targeted. The most commonly used methods are intraparenchymal infusion of either autologous blood (Bullock et al., 1984) or bacterial collagenase (Rosenberg et al., 1990). Both have achieved successes in identifying injury mechanisms and evaluating potential treatments (MacLellan et al., 2010). Spontaneous hemorrhagic strokes in hypertensive mice have also been studied (Iida et al., 2005) and it is found that the type and locations of stroke are reasonably similar to those observed in patients with hypertension. These microhemorrhages in animal models are difficult to control and often result in large regions of pathology, making it hard to observe the hemorrhage dynamics and the physiology immediately after the injury.

A modern non-invasive, non-ionizing technique to visualize detailed brain structures is magnetic resonance imaging (MRI) (Filler, 2010). MRI techniques have been providing new insights into the pathophysiology and diagnosis of cerebral hemorrhage. Gradient-echo (GE) or T2*-weighted MRI is highly sensitive in the detection of old and recent cerebral hemorrhage (Fazekas et al., 1999; Offenbacher et al., 1996). GE MRI is capable of detecting millimeter-sized paramagnetic blood products in brain parenchyma (Atlas et al., 1988). With this technique, the number of visible hemorrhagic brain lesions has been considerably increased.

Recent developments in optical techniques have enabled the application of an injury to a single segment of arteriole, capillary, or venule (Nishimura et al., 2007). A tightly-focused femtosecond laser pulse is used to disrupt the endothelial cells that line a specifically targeted vessel. The technique allows any blood vessel in the top 0.5 mm of the cortex of a rodent to be selectively lesioned. This method along with two-photon excited fluorescence (2PEF) allows the observation of the pathophysiology after the microvascular injury with high temporal and spatial resolutions.

In this chapter, we present mathematical models, derived from both fundamental considerations and empirical correlations, to describe the statics and the dynamics in cerebral microhemorrhage and compare the models with the experimental data.

6.2 Mathematical Model

To better understand the mathematical models introduced below, we first give a short description of the experimental procedures used to collect the data. Adult mice were used in the experiments to characterize hemorrhage dynamics and tissue compression. Before laser ablation and imaging, mice were anesthetized on isoflurane and were intravenously injected with Texas-

Red dextran fluorescent dye to label the blood plasma. Microhemorrhages were induced by focusing femtosecond laser pulses on the wall of the targeted penetrating arterioles (PA). 2PEF movies of the microhemorrhage process were captured. During the microhemorrhage, red blood cells (RBCs) and plasma exit the lumen of the targeted PA. The RBCs are visualized as dark patches in a sea of fluorescently-labeled plasma. Our goal is to develop mathematical models to describe the statics and dynamics of microhemorrhage. Unfortunately, we have not yet found a unified theoretical approach to deal with both the statics and the dynamics. In the following, a poroelastic model is used to describe the statics and a semi-empirical model is used to describe the dynamics.

6.2.1 Microhemorrhage Statics

We treat brain tissue as a fluid-saturated poroelastic network (Basser, P., 1992; Edelman, I.Y., 1999; Netti et al., 1997).

Stress-strain relations for the fluid phase is written as

$$\underline{\underline{\sigma_f}} = -p_f \underline{\underline{I}} \quad (6.1)$$

where p_f is the pressure in the fluid phase, and $\underline{\underline{I}}$ is the unit tensor.

Stress-strain relations for the solid phase is written as

$$\underline{\underline{\sigma_s}} = 2G\underline{\underline{\varepsilon_s}} + \lambda\left(Tr\underline{\underline{\varepsilon_s}}\right)\underline{\underline{I}} \quad (6.2)$$

where G and λ are Lame constants for the solid phase.

The strain tensor $\underline{\underline{\varepsilon_s}}$ is the symmetric part of the gradient of the displacement vector $\underline{u_s}$ of the solid phase,

$$\underline{\underline{\varepsilon_s}} = \frac{1}{2}\left[\underline{\nabla u_s} + \left(\underline{\nabla u_s}\right)^T \right] \quad (6.3)$$

where T is the transpose operation.

At mechanical equilibrium, the divergence of the total stress is zero,

$$\underline{\nabla} \cdot \left\{ (1-\phi)\left[2G\underline{\underline{\varepsilon_s}} + \lambda\left(Tr\underline{\underline{\varepsilon_s}}\right)\underline{\underline{I}} \right] - \phi p_f \underline{\underline{I}} \right\} = \underline{0} \quad (6.4)$$

where ϕ is the porosity.

Substituting equation (6.1) into equation (6.4), we obtain Navier's equation,

$$\underline{\nabla} p_f = \frac{1-\phi}{\phi}\left[G\nabla^2 \underline{u_s} + (G+\lambda)\underline{\nabla}\left(\underline{\nabla} \cdot \underline{u_s}\right) \right] \quad (6.5)$$

At mechanical equilibrium, we also have $\underline{\nabla} p_f = \underline{0}$. Thus

$$G\nabla^2 \underline{u_s} + (G+\lambda)\underline{\nabla}\left(\underline{\nabla} \cdot \underline{u_s}\right) = \underline{0} \quad (6.6)$$

Assuming spherical symmetry, the r component of equation (6.6) is written as

$$G\left[\frac{1}{r^2}\frac{d}{dr}\left(r^2 \frac{du_{sr}}{dr} \right) - \frac{2u_{sr}}{r^2} \right] + (G+\lambda)\frac{d}{dr}\left(\frac{1}{r^2}\frac{d}{dr}\left(r^2 u_{sr} \right) \right) = 0 \quad (6.7)$$

After some straightforward algebra, equation (6.7) is simplified to

$$\frac{d}{dr}\left(\frac{1}{r^2}\frac{d}{dr}\left(r^2 u_{sr} \right) \right) = 0 \quad (6.8)$$

Integrating equation (6.8) twice, we get

$$u_{sr} = \frac{Ar}{3} + \frac{B}{r^2} \quad (6.9)$$

where A and B are unknown integration constants.

We know that as r approaches infinity, u_{sr} should be finite. This means $A = 0$. Equation (6.9) is simplified to

$$u_{sr} = \frac{B}{r^2} \quad (6.10)$$

To figure out B, we need to apply the boundary condition at $r = a_{RBC}$, where a_{RBC} is the steady state radius of the cavity filled with RBCs after the microvascular injury.

$$\left[\left(2G+\lambda\right)\frac{du_{sr}}{dr}+\lambda\frac{2u_{sr}}{r}\right]\Bigg|_{r=a_{RBC}} = -\tau_c \quad (6.11)$$

where τ_c is the contact stress at the boundary between the surrounding tissue and the RBC core. This boundary condition leads to

$$B = \frac{a_{RBC}{}^3\tau_c}{4G} \quad (6.12)$$

The final expression for u_{sr} as a function of r is

$$u_{sr} = \frac{a_{RBC}{}^3\tau_c}{4Gr^2} \quad (6.13)$$

or

$$\frac{u_{sr}}{a_{RBC}} = \frac{\tau_c}{4G}\Bigg/\left(\frac{r}{a_{RBC}}\right)^2 \quad (6.14)$$

When equation (6.14) is fitted with experimental data, τ_c can be extracted.

6.2.2 Microhemorrhage Dynamics

Let us take a look at a very thin layer of solid materials right at the boundary between the RBC core and the surrounding tissue. Assume the mass of such a thin slice is m. When the cavity expands, two forces in opposite directions are exerted upon m. The force pointing outward is the stress exerted by the closely packed RBCs in the cavity. The more RBCs present in the cavity, the larger this force is. Thus we assume that at any given moment this force is proportional to the radius of the RBC cavity $a_{RBC}(t)$ with a proportionality constant of k_R. The force pointing inward is the stress exerted by the surrounding tissue. We can think the surrounding tissue as a reservoir

for stress releasing and treat the inward-pointing force as a constant F_t. With these two forces, we can write down the equation of motion for m along the radial direction,

$$m\frac{d^2 a_{RBC}(t)}{dt^2} = k_R a_{RBC}(t) - F_t \quad (6.15)$$

The general solution is

$$a_{RBC}(t) = \frac{F_s}{k_R} + Ce^{\sqrt{\frac{k_R}{m}}t} + De^{-\sqrt{\frac{k_R}{m}}t} \quad (6.16)$$

where C and D are unknown integration constants.

As t goes to infinity (steady state), R should be finite. This means $C = 0$.

$$a_{RBC}(t) = \frac{F_s}{k_R} + De^{-\sqrt{\frac{k_R}{m}}t} \quad (6.17)$$

$a_{RBC}(0) = 0$ gives $D = -\frac{F_t}{k_R}$.

Thus

$$a_{RBC}(t) = \frac{F_t}{k_R}\left(1 - e^{-\sqrt{\frac{k_R}{m}}t}\right) \quad (6.18)$$

Equation (6.18) can be written as

$$a_{RBC}(t) = a_{RBC}\left(1 - e^{-\frac{t}{\tau}}\right) \quad (6.19)$$

where a_{RBC} and τ are constants independent of time.

When equation (6.19) is fitted with experimental data, a_{RBC} and τ can be extracted.

To derive an expression for $a_{plasma}(t)$, the distance from the center to the edge of the plasma perfusion, we assume that the infusion of plasma to the surrounding tissue is of constant volumetric flow rate Q. Mass conservation requires that

$$\frac{4}{3}\pi\left[a_{plasma}^{3}(t)-a_{RBC}^{3}(t)\right]\cdot\phi=Q\cdot t \quad (6.20)$$

When equation (6.20) is fitted with experimental data, Q can be extracted.

6.3 Results and Discussion

The extravasated RBCs are mainly responsible for displacing nearby cellular structures. From experimental measurement and image analysis, the magnitude and direction of dendrite displacement vectors after a microhemorrhage can be obtained. The distribution of the displacement vectors confirms the spherical symmetry assumption and the $1/r^2$ decay of the compression. From the compression magnitudes averaged over all mice, we are able to extract the contact stress between the RBC core and the surrounding tissue by fitting the data to equation (6.14) (Figure 6.1).

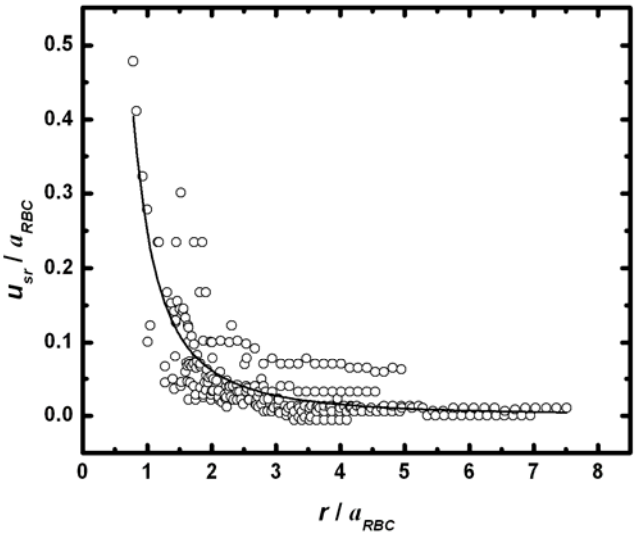

Figure 6.1: Distribution of the displacement magnitude. Dots represent the experimental data and solid line represents the fitted curve.

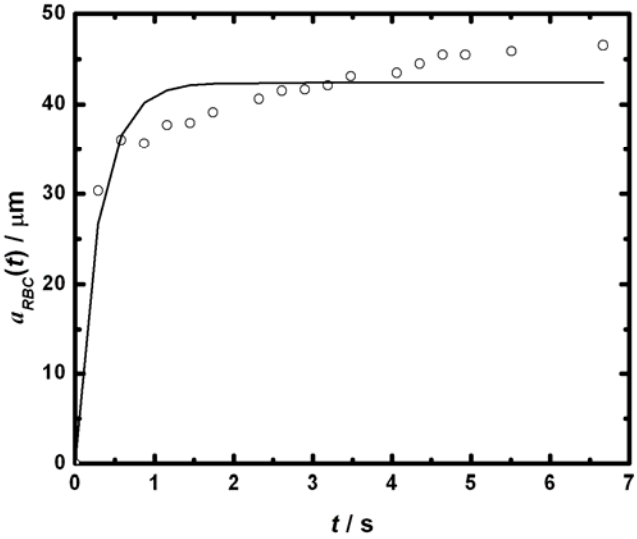

Figure 6.2: Relaxation dynamics of the RBC core. Dots represent the experimental data and solid line represents the fitted curve.

Table 6.1: τ and a_{RBC} fitted by equation (6.19).

Mouse number	τ / s	a_{RBC} / μm
1	0.25	48
2	1.5	39
3	0.43	35
4	0.36	44
5	0.64	72
6	0.50	72
7	0.30	56
8	1.2	21
9	1.9	23
10	1.3	53
11	0.33	29
12	0.71	29

Table 6.2: Q fitted by equation (6.20).

Mouse number	Q / (μL/min)
1	8.4×10^{-4}
2	3.3×10^{-4}
3	1.3×10^{-3}
4	6.9×10^{-4}
5	N/A
6	1.4×10^{-2}
7	7.3×10^{-2}
8	4.9×10^{-5}
9	N/A
10	6.6×10^{-3}
11	1.3×10^{-3}
12	1.3×10^{-3}

With a G value of 2 kPa (Basser, 1992), the contact stress at the interface is calculated to be ca. 2 kPa. This is significantly smaller than the arteriole intraluminal pressure, which has been found to be 8 kPa (Driessen et al., 1982). Although this value was measured in rat mesentery, which may differ from that in mice brain, it has been observed experimentally that almost all of the capillary segments are preserved post-hemorrhagically in the vicinity of the injury. This indicates that the compressive stress due to a microhemorrhage is not high enough to produce a disaster of capillary collapse, which may lead to ischemia, cellular dysfunction, or death.

Immediately after laser ablation, the RBCs and the plasma flush out into the extracellular

matrix and form a small cavity in no more than several seconds. The RBCs inside the cavity serve as a support for the cavity against adjacent tissue. The plasma perfuses through the interstitial space and penetrates into the surrounding tissue. Equation (6.19) is used to extract the relaxation time constant τ (Table 6.1). There is a great variation in τ, ranging from 0.2 s to 2 s. It seems that there are no correlations between τ and a_{RBC}. The average τ value from all mice is 0.8 s. Figure 6.2 shows typical relaxation dynamics of the RBC core. Equation (6.20) is used to extract the plasma perfusion flow rate Q (Table 6.2). There is a great variation in Q, with the highest value being three orders of magnitude larger than the lowest value. It seems that there are no correlations of Q with either τ or a_{RBC}.

As we can see, the mathematical model developed here to describe the microhemorrhage dynamics is rather simple and heuristic. It is highly desirable that we have a unified theory to describe both the statics and the dynamics. As in the model for the statics, we have made several attempts to develop a model for the dynamics based on the theory of fluid-saturated poroelastic network. Unfortunately, those attempts were not successful. We encountered a major difficulty in the mathematical derivations. The boundary between the RBC core and the surrounding tissue is moving all the time. A moving boundary, seemingly not problematic, often requires the help of complicated computer algorithms. We hope that our heuristic model for the dynamics could at least provide some useful information for the biomedical community.

CHAPTER 7

DESIGN AND FABRICATION OF MICROFLUIDIC PROBES WITH INTEGRATED PRESSURE SENSORS FOR CONVECTION ENHANCED DRUG DELIVERY

7.1 Introduction

Convection-enhanced delivery (CED) has proven to be a promising new technique for treating neurological disorders. Many compounds have been delivered in both animal and human experiments using CED. For example, small molecules (Bobo et al., 1994; Groothuis et al., 1999; Lonser et al., 1999), proteins (Laske et al., 1997; Lieberman et al., 1995; Lonser et al., 2002), growth factors (Hamilton et al., 2001; Yang et al., 2002), and nucleotides (Groothuis et al., 2000) have been examined in animals. Chemotherapy drugs (Lidar et al., 2004; Mardor et al., 2001), proteins (Kunwar et al., 2007; Sampson et al., 2003; Weber et al., 2003), and viral vectors (Ren et al., 2003; Worgall et al., 2008) have been examined in human clinical trials. In CED, a small catheter or needle is inserted into an afflicted region and drug-containing solutions are directly infused into that region at a specified flow rate. This technique circumvents the blood brain barrier (BBB). Compared to systemic delivery, higher local concentrations of therapeutic agents can be achieved with fewer side effects. Because many drugs delivered directly to the brain are subject to rapid clearance from the extracellular space (Haller et al., 1998), drugs delivered by diffusion from polymeric implants or bolus injections are only able to penetrate a small distance into the tissue. Unlike diffusion, which relies on a concentration gradient, CED relies on the bulk flow to carry compounds through the extracellular space. As a result, drugs can penetrate into the tissue that is much further from the delivery site.

In most prior studies on CED, stainless steel needles were often used and ranged from 20 to 32 gauge in size. Flow rates were controlled with an external syringe pump and ranged from 0.1-10 μL/min. Operation with known flow rates has the benefit of better control of the delivered dose. At flow rates greater than 1 μL/min, backflow of infused solution up to the outside of the needle shaft has been reported (Chen et al., 1999). This is an eminent and long-existing problem associated with CED. Brain tissue is a poroelastic medium. Since there is usually no contact stress between the infusion needle and the tissue at the infusion point, the adjacent tissue is free to move away from the needle during infusion. This movement of the tissue is the cause of reflux of infused solution along the needle-tissue interface and the phenomena is called backflow. This is the cause of many treatment induced complications in CED. Backflow leads to poor control over the fate of infused drugs which often end up in healthy tissue. The separation between the needle and the adjacent tissue that allows backflow to happen can be controlled by adjusting the flow rate and the size of the needle (Morrison et al., 1999). Another problem associated with CED is that it is possible that the outlet of needle is partially or fully occluded after it is inserted into the brain. It has been suggested that a needle with fluid outlets along its side, rather than at its tip, could avoid or alleviate the occlusion problem (Chen et al., 2004).

Microfabricated probes offer several potential advantages over traditional needles used in CED. A microfabricated probe can be made small to minimize tissue damage (Zahn et al., 2000), reduce backflow (Neeves et al., 2006), yet rigid enough to penetrate deep into tissue. The fluid outlet can be located away from the penetrating edge of the probe to avoid occlusion of the channel. Furthermore, microfabrication offers the possibility of integrating electrical, mechanical, and chemical sensors with the fluid delivery system (Chen et al., 1997; Retterer et al., 2004; Zahn et al., 2000).

For CED, an integrated pressure sensor is desirable since pressure drops are often good

indicators of serious backflow problems or other failures. Capacitive pressure sensors fabricated by multilayer parylene/photoresist techniques have been demonstrated on whole silicon wafers (Shih et al., 2003). The goal of this chapter is to describe the design and fabrication of a microfluidic probe with a capacitive pressure sensor integrated at its tip. Such a device should be able to monitor the tip pressure rather than an upstream pressure because, more often than not, it is desirable that the pressure reading only reflects flow through the tissue rather than flow through the syringe, needle, and tissue.

7.2 Experimental Design

The microfluidic probe consists of three parts: an insertable microprobe, a handle, and a protrusion to be connected to external tubing (Neeves et al., 2006).

Figure 7.1 shows a schematic of the device (not in scale). Red lines represent the profile of the probe, green lines represent the profile of the microfluidic channel, and yellow lines represent the profile of the electrodes. Figure 7.2 shows another schematic of the device (in scale). Figure 7.3 shows a zoom-in view of the probe tip (in scale). The pressure sensing functionality is realized by creating a two-plate configuration of a capacitor (Figure 7.4). The upper electrode is sandwiched between two partially suspended parylene layers and the bottom electrode is fixed on the substrate. The microfluidic channel is on top of the upper electrode. When the local pressure in the microfluidic channel changes, the capacitance between the two electrodes will change. With proper device calibration, this capacitance change can be

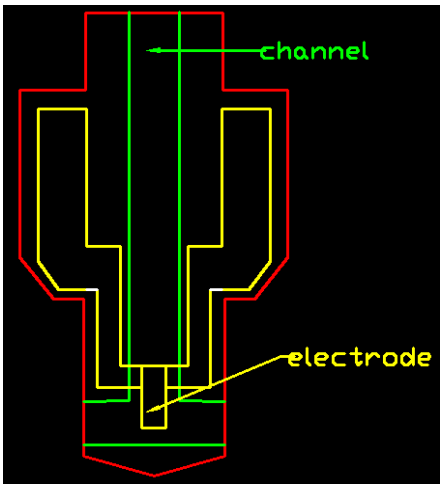

Figure 7.1: Schematic of the probe (not in scale). Red lines represent the profile of the probe, green lines represent the profile of the microfluidic channel, and yellow lines represent the profile of the electrodes.

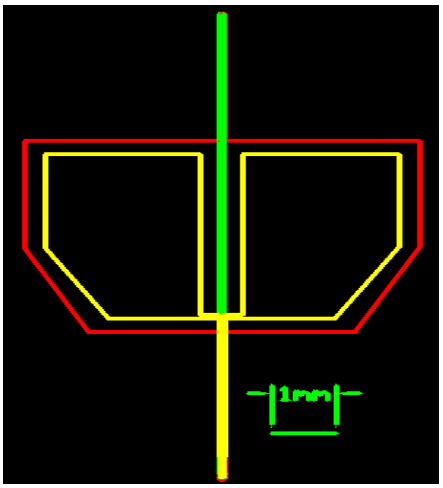

Figure 7.2: Schematic of the probe (in scale). Red lines represent the profile of the probe, green lines represent the profile of the microfluidic channel, and yellow lines represent the profile of the electrodes.

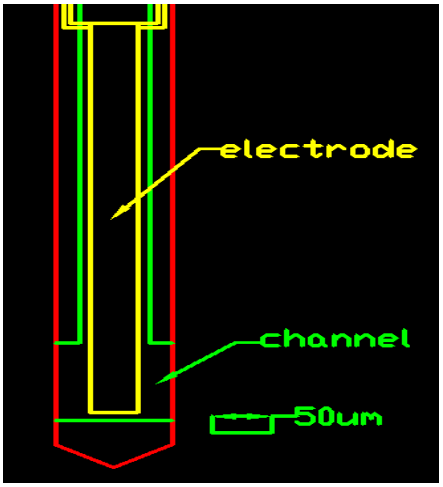

Figure 7.3: Zoom-in view of the probe tip (in scale).

used to calculate the corresponding pressure change. The air gap (the cavity between the two electrodes) is unsealed to maintain a constant atmospheric reference pressure. Other parts of the electrodes are designed for transductions of the electrical signals from the sensing areas to the bonding pads. The bonding pads (the big yellow polygonal parts of the electrodes, see Figure 7.4) will be connected to a commercially available capacitance meter.

The fabrication process is described as follows (Figure 7.4): To start the fabrication, a silicon dioxide etch mask is deposited using plasma enhanced chemical vapor deposition (PECVD) on the backside of a double-sided, polished silicon wafer with a thickness of 300 μm. The backside of the wafer is then etched with deep reactive ion etching (DRIE) to a depth of 200 μm to define the insert and protrusion thickness. A 2 μm silicon dioxide layer is then deposited on the back side of the wafer using PECVD. This layer acts as an etch stop when the front side of the wafer is etched using DRIE in a subsequent step. To form a base layer and promote adhesion, a 1 μm thick layer of photo-sensitive polyimide is spun, patterned, and cured on the front side of the wafer. Next, a 10 nm layer of Cr and a 300 nm layer of Au is electron

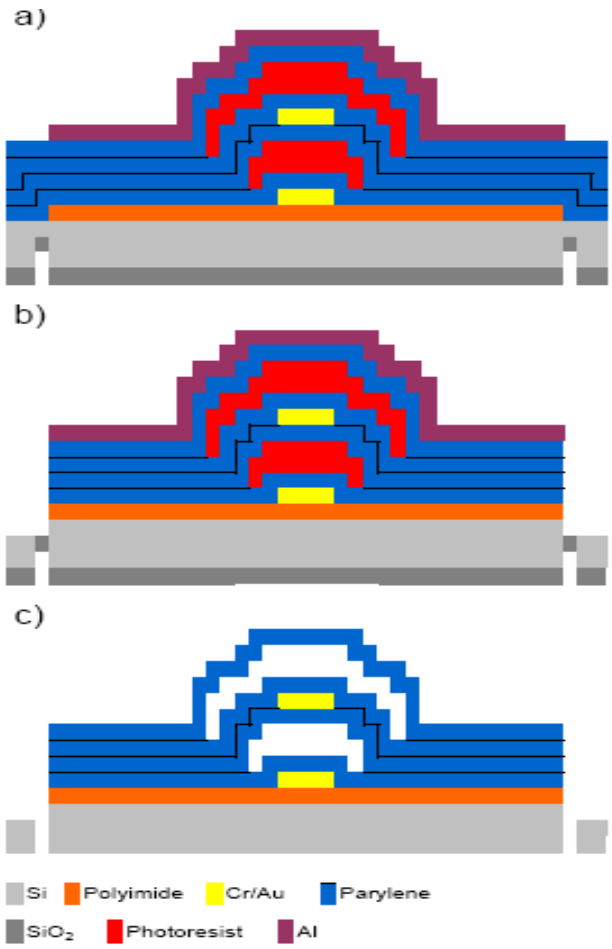

Figure 7.4: Summary of fabrication process. (a) Backside oxide deposition and patterning, backside DRIE, backside oxide deposition for etch stop, polyimide deposition and patterning, Cr/Au deposition and patterning ,parylene deposition sacrificial photoresist spinning and patterning, parylene deposition, Cr/Au deposition and patterning, parylene deposition, sacrificial photoresist spinning and patterning, parylene deposition, Al deposition and patterning. (b) Patterning of parylene by oxygen plasma, DRIE of front side silicon. (c) Dissolution of Al, dissolution of oxide, release of sacrificial photoresist.

beam evaporated and patterned in the shape of the bottom electrodes. The Cr layer acts as an adhesion layer for Au. A layer of parylene is then deposited to a thickness of 1 μm. Sacrificial photoresist is spun on top of the parylene to form a layer of height 4 μm. This sacrificial layer

defines the capacitive air gap in the pressure sensor. After another 1 μm parylene layer, a second Cr/Au layer (10 nm / 150 nm) is deposited and patterned to produce the top electrodes of the pressure sensor and the parallel plate configuration. A third 1 μm layer of parylene is then deposited and a 10 μm sacrificial photoresist layer is deposited and patterned to define the microfluidic channel above the pressure sensor. A final 1 μm layer of parylene is then deposited. Next, a 150 nm thick Al etch mask is electron beam evaporated. This mask is patterned using wet etching. An oxygen reactive ion etching (RIE) is then used to etch through the parylene to the silicon wafer. This etching step defines the device body and opens the ends of the air gaps and the microfluidic channels. The silicon is etched down to the oxide etch stop using DRIE to define the insert and protrusion geometry. The oxide etch stop and Al mask are simultaneously removed in buffered oxide etch. Finally, the photoresist is removed from the air gaps and the microfluidic channels in an acetone bath.

7.3 Results and Discussion

Fabrication of the as-designed device has not been successfully completed. There are several difficulties and problems arising in the actual fabrication trials. First, the adhesion of parylene to the substrate is problematic. Prior to parylene deposition, the substrate needs to be treated by mild oxygen plasma and dehydrated either on a hot plate or in a convection oven. The as-deposited parylene film is able to adhere well on the substrate. Yet the bond is weak and the film tends to peel off in subsequent processing steps, especially those steps involving wet chemicals. Second, the patterning of the upper electrodes is problematic. The bottom electrodes have been successfully patterned using lift-off techniques. Due to the presence of the first sacrificial photoresist layer which is intended to form the air gap upon dissolution, part of the

connections between the top electrodes and the bonding pads resides on the tilted part of the parylene layer covering the sidewall of the sacrificial photoresist. As a result, the top electrodes have to be patterned by wet etching instead of lift-off. It is difficult to control the etching of the Cr layer due to its thickness. Third, the environment in which parylene is deposited is problematic. The fabrication process was carried out in the Cornell NanoScale Science & Technology Facility (CNF). Its parylene deposition system is located in a normal laboratory rather than in a cleanroom. Dust particles falling onto the surface of the wafer are of serious problems. They are hard to get rid of and they introduce an exponentially-growing number of defects in later processing steps. There are a total of 4 layers of parylene to be deposited. Each time the wafer has to be exposed to a non-cleanroom environment. And there are quite many processing steps between and after parylene depositions. This introduces lots of defects on the surface of the wafer. Before devices can be successfully fabricated, all these problems need to be resolved.

CHAPTER 8

MICROMACHINED DISSOLVED OXYGEN SENSOR BASED ON SOLID POLYMER ELECTROLYTE

8.1 Introduction

Dissolved oxygen sensors are important for measuring the oxygen content in body fluids and tissues (Baumgartl et al., 1983; Althoff et al., 1985) and can be used as basic devices for integrated biosensor applications (Nanjo et al., 1974; Mascini et al., 1986; McKean et al., 1988). Dissolved oxygen sensors presently available on the market are relatively large devices that are difficult to use in some biological and biomedical applications. The devices often require labor-intensive manufacturing and assembly owing to the complicated and delicate structures embedded in them. Microfabrication technology such as photolithography provides the possibility of easy and cost effective production of smaller devices while improving the usability and robustness of these devices.

Miniaturization has been an important trend in the fabrication of sensors for the past four decades. For the specific case of dissolved oxygen sensors based on electrochemical methods, the immediate benefits from miniaturization are little oxygen consumption and enhanced spatial resolution. One of the earliest versions of miniaturized dissolved oxygen sensors was fabricated from glass micropipettes. For example, in the work by Whalen et al. (1967), a glass capillary tube was drawn out in a pipette puller and filled almost to the tip with molten metal. The metal in the recess was subsequently plated with gold and the recess filled with collodion. The sharp microelectrode had a long, tapering point, with a tip of 1-2 μm. The sharp tip could be utilized to

impale cells in intracellular oxygen level measurements. These types of microsensors had to be manually fabricated and assembled one by one. In the past three decades, owing to the progress in semiconductor and micromachining techniques, various types of miniature oxygen sensors have been proposed (Koudelda, 1986; Suzuki, et al., 1988, 1990, 1991, 1993, 1998, 2000, 2001; Wu et al., 2005; Jobst et al., 1993; Yang et al., 1997). The majority of these sensors were Clark-type. The Clark-type sensor operates by electrochemically reducing the dissolved oxygen in solution and measuring the electrical current to determine the oxygen level. The main advantage of the Clark-type design is that all the electrodes required for operation are contained within an inert gas permeable membrane. This membrane allows the device to be used in delicate biological media such as blood. Isolating the electrodes from the media improves the accuracy of the measurement, since it eliminates other electroactive species from giving additional reduction current signals. In the three-electrode configuration, the construction of the working, reference, and counter electrodes could be easily integrated by micromachining techniques. It was also possible to incorporate on-chip microstructures, on-chip electronic circuits, and other chemical microsensors (e.g. glucose sensors) into the fabrication process. Clark-type oxygen sensors require a compartment filled by aqueous electrolyte between the membrane and the electrode. This requirement has dramatically complicated the fabrication procedure, decreased the robustness of the device, and lead to the need for rehydration in long term storage. Hydrogel and solid polymer electrolyte have been shown to be able to replace the aqueous-electrolyte-filled compartment. Among these methods, the PCM approach is especially attractive due to the simplicity and scalability of the fabrication and packaging procedures (McLaughlin et al., 2002). However, there are some common shortcomings from an industrial and medical point of view in most of the previous work on miniature oxygen sensors constructed by micromachining techniques: First, the fabrication procedures are lengthy and time-consuming, making these

devices inamicable for large-volume production and thus not disposable. Second, the materials used for the working, reference, and counter electrodes in these devices are different. This means that the thin films used as the working, reference, and counter electrodes have to be deposited and patterned one by one, which greatly complicates the processing procedures. Third, none of them is well transferable for clinical applications. The functional parts of these sensors are small, but the whole sensors are big and therefore non-implantable. In this paper, we describe an extremely simple monolithic procedure for fabricating and packaging disposable, dissolved, PCM-based oxygen sensors that are suitable for medical applications. We test these devices in PBS and BBS and evaluate their performances in terms of long term stability, reliability, hysteresis, linearity, sensitivity, and device-to-device variation, with a focus on medical usefulness.

8.2 Experimental Methods

8.2.1 Preparation of Microelectrode Probes

Microelectrode probes were fabricated using standard micromachining techniques. A schematic of the electrode fabrication process is presented in Figure 8.1. To start the fabrication, a 500 nm insulation layer of silicon dioxide was deposited on a 4-inch silicon wafer (500 μm thick, single side polished, <100> crystal orientation) by plasma enhanced chemical vapor deposition (PECVD) (GSI single wafer PECVD, GSI Group Sciences) The lift-off technique was used to define the electrode geometry (Figure 8.2 and 8.3). The geometry and arrangement of the three electrodes are similar to those in ref. 15. Layers of 30 nm of Ti and 130 nm of Pt were electron beam evaporated (CHA Mark 50 e-Beam Evaporator) on the substrate to form the

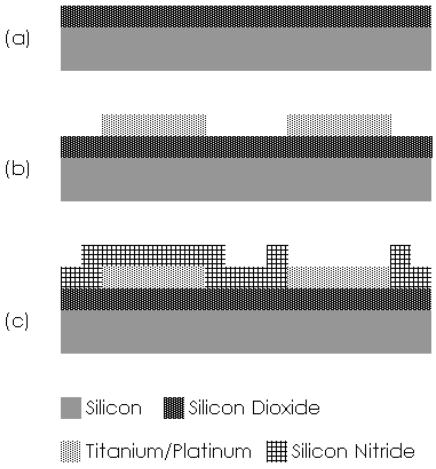

electrodes.

Figure 8.1: Summary of photolithographic processes. (a) Deposition of silicon dioxide insulation layer, (b) Deposition and patterning of platinum metallization layer, (c) Deposition and patterning of silicon nitride capping layer.

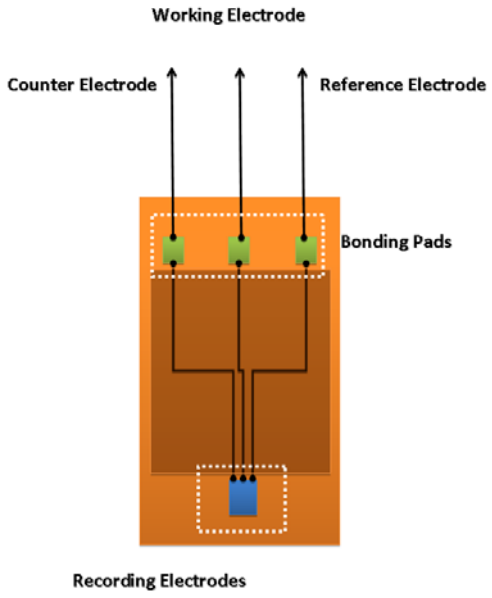

Figure 8.2: Schematic illustration of the device planar structure (not in scale).

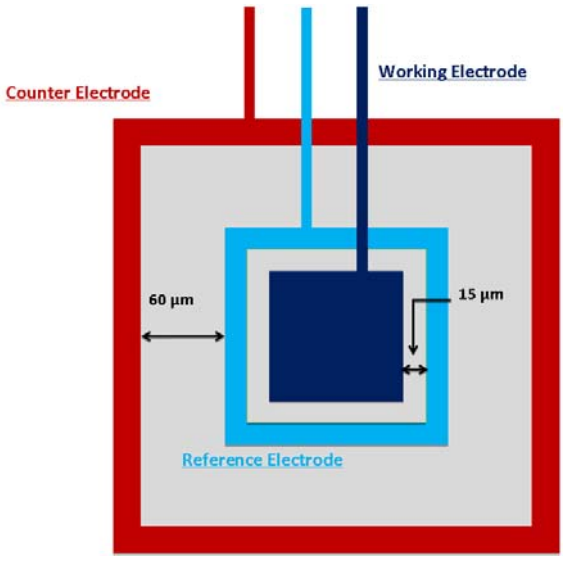

Figure 8.3: Schematic illustration of the electrode configuration (not in scale).

Wafers were then coated with a 400 nm capping layer of low stress silicon nitride by PECVD. The recording areas and the bonding pads were defined by selectively etching the silicon nitride layer using reactive ions (Oxford 81 Etcher, Oxford PlasmaLab 80+ RIE System). Wafers were diced into 1.1 mm×7.3 mm chips (Kulicke & Soffa 7100 Dicing Saw). For each chip, bonding pads were connected to insulated fine wires by silver conductive epoxy (MG Chemicals) and then insulated from the environment with regular epoxy (Epoxy 907, Miller-Stephenson). The exposed area of the working electrode was designed to be ca. 0.43 mm^2. The areas of the working, reference, and counter electrodes are maintained in the ratios 1:0.2:0.44. The gap between the working electrode and the reference electrode is 15 µm and the gap between the reference electrode and the counter electrode is 60 µm.

8.2.2 PCM Coating

After fabrication and packaging, the microprobes were immersed sequentially in isopropyl alcohol, dilute sulfuric acid, and deionized water, each for 10 min, and then dried by a nitrogen gun. At this point, the microprobe was ready for deposition of the PCM. The PCM is a mixture of 5 wt.% solution of Nafion^{TM}, a perfluorinated ion-exchange resin (hydrogen ion form), in a mixture of lower aliphatic alcohols and water (Aldrich, Milwaukee, WI, USA) and polyvinylpyrrolidone (PVP-360) (Sigma, St. Louis, MO, USA) with 3 wt.% 2,6-bis(azidobenzylidene)-4-methylcyclohexanone (Aldrich) in a ratio of 4:1. The Nafion^{TM} component provides ionic (proton) conductivity while the PVP-360 improves adhesion of the PCM to the substrate.

For better adhesion, the device was dipped in a mixture of Silane 174A (Sigma) and ethanol in a ratio of 1:50 for 5 min and allowed to dry at 60 ℃ for 5 min. Next, the PCM was applied by either drop casting or dipping coating. In dipping coating, the device was dipped in the PCM solution for 5 min. In drop casting, 0.4 μL of PCM solution was applied to the surface of the device (area uncovered by epoxy, dimension 1.1 mm×1.5 mm) via a micropipette. Finally, the device was allowed to dry at 60 ℃ for at least 24 h.

8.2.3 PCM Surface Morphology and Film Thickness Characterization

Atomic force microscopy (AFM) was utilized to characterize the surface of the PCM. AFM was conducted on a Veeco Dimension 3100 Ambient AFM system employing an Olympus cantilever. Potential step chronoamperometry (PSC) was performed to estimate the thickness of

the PCM film. All electrochemical experiments in this work were carried out on a CHI600D electrochemical work station. The settings of the electrochemical recording system were such that cathodic currents were defined to be positive and anodic to be negative.

8.2.4 Evaluation of Sensor Performances

We investigated the characteristics of the oxygen electrodes by immersing the device in either PBS (137 mM NaCl, 2.7 mM KCl, 10 mM Na_2HPO_4, 10 mM KH_2PO_4, pH 7.4, EMD Chemicals, Inc.) or BBS (Rockland), allowing them to equilibrate, and monitoring their response by CV or LSV techniques. We reduced the oxygen concentration in the solution by means of purging the solution with pure nitrogen (high purity, Airgas). The output of the oxygen electrode was calibrated with a commercial dissolved oxygen meter (InO2, Innovative Instruments, Inc.). Sodium lactate was purchased from Sigma-Aldrich.

8.3 Results and Discussion

The physical dimensions of the device have been designed to be small enough for medical implantation purposes but large enough to minimize internal electrical resistance. Micromachining techniques offer a unique opportunity for creating large amounts of identical devices from a single processing batch in a cost effective manner. In our design, a total of 287 devices can be obtained from a single 4-inch silicon wafer. The monolithic procedure in thin film Pt electrode fabrication has greatly reduced the processing steps involved. Pt is a common material of choice for the working and the counter electrode in oxygen reduction. Pt has also been shown to be able to serve as the reference electrode under certain conditions (Kasem,

2008). For oxygen reduction, we have found that Pt can be used as the reference electrode for sensing purposes. A single layer of PCM coating has also dramatically reduced processing steps and time. In this work, the PCM coating serves the dual purposes of acting as the ionic conductive electrolyte and the interfering molecule blocking membrane. The drop-casting or dip-coating approach makes the processing very inexpensive.

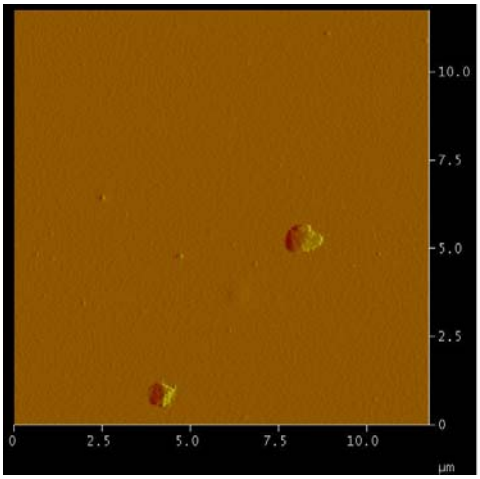

Figure 8.4: AFM image of the surface of the PCM. The dimensions of the image are 12 µm by 12 µm.

Only the PCM film prepared by drop-casting was investigated in detail. Although dip-coating procedures are easier and faster to carry out and the devices do, to some extent, work well in terms of oxygen sensing, we have found that dip-coating processed devices are not as robust as drop-casting processed ones and this method may lead to early device failure in repetitive operations. When the chips with Silane 174A adhesion layers are dipped in the PCM coating solution, Silane 174A may be partially stripped, which will lead to inferior adhesion and earlier device failure. On the other hand, due to the extreme simplicity of dipping-coating procedure, it is desirable to pursue adhesion layer enhancement treatment in the future to make such devices more reliable.

Figure 8.4 shows the AFM image taken on a 12 μm×12 μm site area of the PCM surface. Most area of the surface appears to be smooth and pin-hole free. According to the image statistics, the mean roughness of the PCM surface is ca. 4 nm. The surface tension of the coating

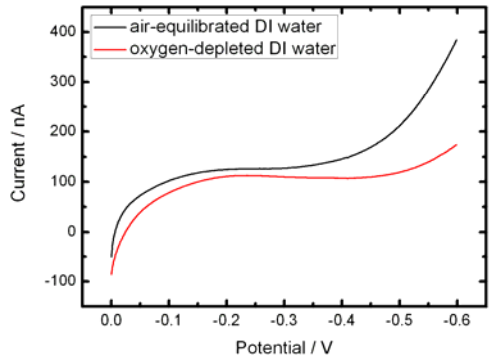

Figure 8.5: Linear sweep voltammograms obtained in air-equilibrated DI water and oxygen-depleted DI water.

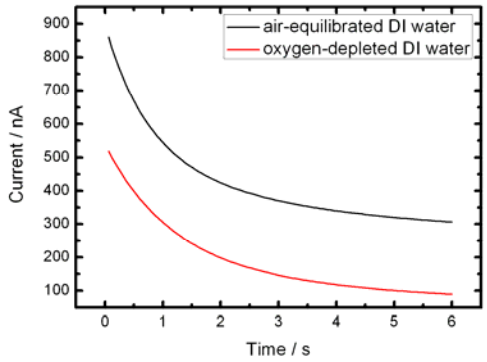

Figure 8.6: Current-time curves obtained in air-equilibrated DI water and oxygen-depleted DI water.

solution leads to a smooth surface morphology upon drying. The needle or bump-like surface structures can be attributed to defects (e.g. tiny dust particles).

The PCM coating should be thick enough to prevent interfering species (e.g. proteins) from reaching the Pt surface but also thin enough to minimize oxygen diffusion resistance. The thickness of the PCM film is difficult to be measured accurately. We choose to estimate this parameter in two different ways. Based on the non-volatile content of the PCM coating solution and the measurement of the solution-covered geometric area, we estimate that the thickness of the PCM film is 6.7±0.7 μm (The variance in film thickness is estimated based on the variance of the solution dispensing apparatus). A second way to estimate the film thickness is based on PSC technique. Prior to measurement, the electrodes were electrochemically stabilized in air-equilibrated DI water by CV from 0 V to -0.6 V at 2 V/s for 5 min and then at 0.06 V/s for 1 h. LSV measurements were subsequently carried out from 0 V to -0.6 V at 0.06 V/s for air-equilibrated DI water and oxygen-depleted DI water (Figure 8.5). The difference between the two curves is attributed to oxygen reduction. In PSC measurements, the potential was stepped from 0 V to -0.6 V instantaneously and the current was recorded with time (Figure 8.6). In order to single out the faradaic current corresponding to oxygen reduction, we subtract the current recorded in oxygen-depleted DI water from air-equilibrated DI water. The background current recorded in the absence of oxygen represents double-layer charging effects and other faradaic processes occurring on the electrode surface. The background-subtracted current is fitted according to equation (1.4) and (1.10) in McLaughlin et al. (2002). In this way, the thickness of the PCM film is estimated to be 5.0±1.4 μm (n=10). Since the film thickness determines the mass transfer resistance to oxygen diffusion, the dynamical response of the device can be affected by variation in film thickness. From the film thickness and the oxygen diffusion coefficient in the film, the diffusion time constant of the device is estimated to be ca. 0.15 s. According to PSC measurements, there is a 28% relative variation in film thickness. One possible method to reduce device-to-device variation is to use a controlled stencil placed on top

of the electrode to carry out the PCM coating step. Alternatively, thin film coating techniques other than drop-casting can be explored as replacements.

The device can be operated in two distinct ways to detect oxygen concentrations in the

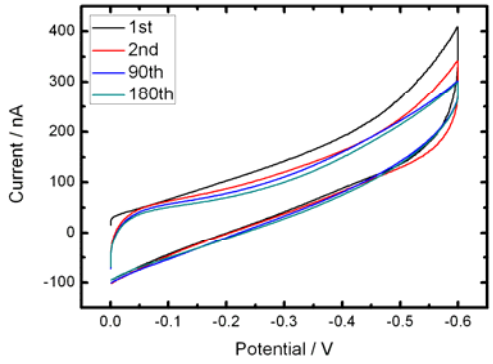

Figure 8.7: Cyclic voltammograms obtained in PBS during electrochemical stabilization.

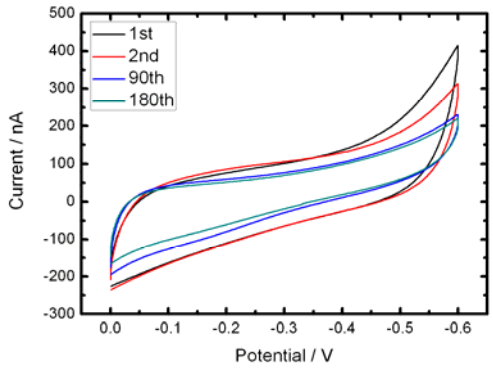

Figure 8.8: Cyclic voltammograms obtained in BBS during electrochemical stabilization.

solution (Bard et al., 2001). In the first way, LSV is utilized to quantify the oxygen level: for a given sweep rate, the current sampled at a given potential should be proportional to the oxygen concentration. In the second way, PSC is utilized to quantify the oxygen level: for a given potential step, the current sampled at a given time should be proportional to the oxygen

concentration. These theoretical relations are valid in both the mass transfer controlled regime and the kinetics controlled regime. Operation in the mass transfer controlled regime has the advantage of yielding larger signals. In principle, LSV and PSC techniques are equivalent to each other. Many commercial dissolved oxygen sensors are based on PSC technique. In practice, we have found that, for PCM-based dissolved oxygen sensors, LSV technique is a better choice in terms of enhancing single-device repeatability and reducing device-to-device variations (Similar observations were reported in McLaughlin et al. (2002)).

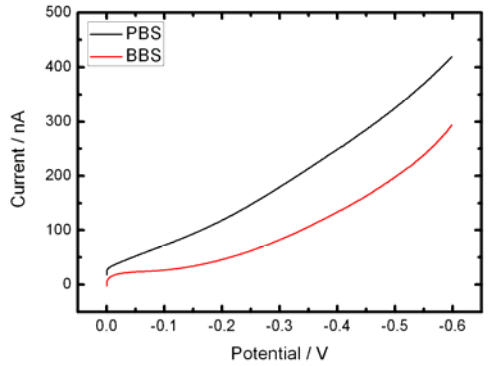

Figure 8.9: Linear sweep voltammograms obtained in PBS and BBS.

Prior to measurements, the electrodes were electrochemically stabilized in air-equilibrated PBS or BBS by CV from 0 V to -0.6 V at 2 V/s for 5 min and then at 0.06 V/s for 1 h. In Figure 8.7 and 8.8, some cycles in the cyclic voltammograms at 0.06 V/s for 1 h are shown. The electrochemical activity of the electrode can reach the steady state faster and diminishes less in PBS compared to in BBS. The cathodic current includes oxygen reduction at the Pt surface, double layer charging, and other parasitic reactions.

After the electrochemical stabilization procedure, the electrodes were left in quiescence in the solution for 3 min. Then LSV curves were recorded from 0 V to -0.6 V at 0.06 V/s (Figure 8.9). Notice that these curves are not identical to those in the last cycle of CV in the

corresponding medium. This is due to the mass transfer complications involved in CV techniques. The initial potential was chosen where there is almost no oxygen reduction. The final potential was chosen where oxygen reduction is supposed to happen at its mass transfer limiting

Table 8.1: Current values at -0.6 V in LSV measurements.

Current values (nA)	0	3 min	6 min	9 min	30 min	1 h	12 h	Coefficient of variation
PCM coated electrode in PBS	419	426	434	433	519	547	532	0.12
PCM coated electrode in BBS	294	291	285	282	308	297	325	0.05
Bare electrode in PBS	624	538	544	590	865	1098	686	0.29
Bare electrode in BBS	364	357	351	347	413	366	764	0.36

rate. Below -0.6 V (especially -0.7 V and below), hydrogen evolution will occur and the gas bubbles will destroy the PCM coating. The scan rate was chosen such that the data acquisition time is 10 s, neither too short for double-layer charging current to dominate nor too long as unnecessary for engineering purposes. In general, the LSV response of the device depends on the medium, i.e. the LSV curves obtained in DI water, PBS, and BBS are different. One of the well-adopted structural models for Nafion describes its microscopic structure as clusters interconnected by narrow channels (about 1 nm in diameter) which determine the transport properties of ions and water (Gierke et al., 1982). The chemical species present in the aqueous medium (e.g. ions, proteins) can affect the molecular structures of the film by either diffusing into the channels or adsorbing onto the surface. These processes are associated with the changes

in the CV behaviors during the electrochemical stabilization. The electrochemical stabilization process settles the film down to equilibrium or quasi-equilibrium with the medium and makes the device become more consistent and show less long term drifting.

After the first LSV curve was recorded, more LSV curves were taken subsequently at the time points of 3 min, 6 min, 9 min, 30 min, 1 h, and 12 h. The current values at -0.6 V are used to quantify the electrochemical activity of the electrodes. For comparison, bare Pt electrodes were also examined following identical experimental procedures (including electrochemical stabilization). Data are shown in Table 8.1. Both the short term and long term performances of the PCM coated electrodes are better than those of the bare Pt electrodes. It is unexpected that results obtained for PCM coated electrodes in BBS are better than those obtained in PBS, which could be observed irrespective of the devices used, the batch of the PBS prepared, the batch of the BBS purchased, etc.

From now on, we will focus on device performance evaluation in BBS which is more clinically relevant in long term implantations. Device-to-device variation was examined by LSV techniques and results are quantified by the current values at -0.6 V. For PCM coated electrodes, the current values at -0.6 V are 247±65 nA (n=10). For bare Pt electrodes, the current values at -0.6 V are 346±78 nA (n=10). Compared to PCM coated electrodes, the bare Pt electrodes have a slightly smaller coefficient of variation (0.23 versus 0.26). However, when long term device reliability is placed as the most important consideration, PCM coated electrodes should be used. Therefore, from now on we will focus on PCM coated electrodes. Notice that if the current at -0.6 V is assumed to be the diffusion limited cathodic current, then a relative variation of 26% in this current will roughly translate into a relative variation of 26% in the PCM thickness, which is consistent with film thickness characterization results in the previous discussion.

One requirement for an implanted dissolved oxygen sensor is that it should be insensitive

to agitation caused by body fluid convection or patient movement. In our experiments, the device was immersed in air-equilibrated BBS contained in a beaker. A magnetic stirrer was used to generate forced convection in the solution. The rotation speed of the stir bar was varied from 0 to the possible maximum. LSV measurements were carried out and the current values at -0.6 V are used to quantify the results. The statistics on measurements with all different rotation speeds gives a mean value of 271 nA, a standard deviation of 12 nA, and a coefficient of variation of 0.04. This variation is acceptable if we take into account that the readings from a single device in long term tests in air-equilibrated BBS have a coefficient of variation of 0.05 (see Table 8.1). The insensitiveness of the device operation to stirring implies that the oxygen mass transfer resistance is dominated by diffusion through the PCM film.

These micromachined dissolved oxygen sensors were designed and intended for long term implantation use. One important target application is post-operative tissue microenvironment (e.g. oxygen level) monitoring in free tissue transfers. The oxygen concentrations to be monitored in this and most of other medical situations range from 0% atm to 21% atm (x% atm corresponds to the oxygen concentration in a solution in equilibrium with a gas phase of x% atm pure oxygen). For example, in the aforementioned application, 21% atm oxygen level indicates the normal condition with well-established blood flow. Near 0% atm oxygen level indicates the occurrence of ischemia. For any reliable sensor, any measurement should be independent of the measurement history of the sensor. In the case of a dissolved oxygen sensor, the reading should depend on the oxygen level in the solution being monitored, but not on the oxygen level in the solution previously monitored. We prepared oxygen-depleted BBS by purging nitrogen into the solution. The device was alternatively immersed in air-equilibrated BBS and oxygen-depleted BBS. LSV measurements were carried out and the current values at -0.6 V are used to quantify the results. The statistics (Figure 8.10) has shown

that the values obtained in air-equilibrated BBS are consistent with each other and the values obtained oxygen-depleted BBS are consistent with each other, regardless of the measurement history. The offset currents at the zero oxygen concentration level are primarily caused by device

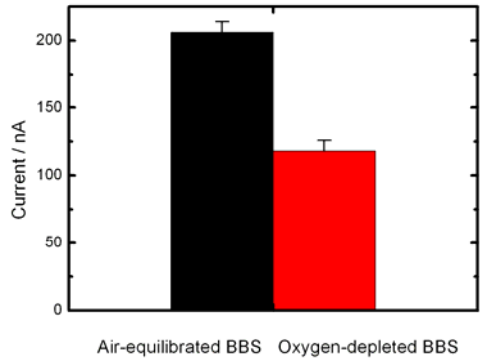

Figure 8.10: Current values at -0.6 V obtained in air-equilibrated/oxygen-depleted BBS.

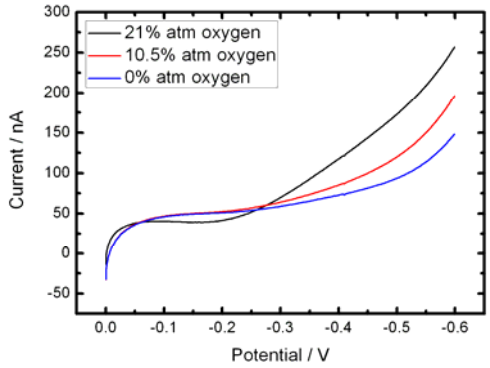

Figure 8.11: Linear sweep voltammograms obtained in BBS with three different oxygen concentration levels.

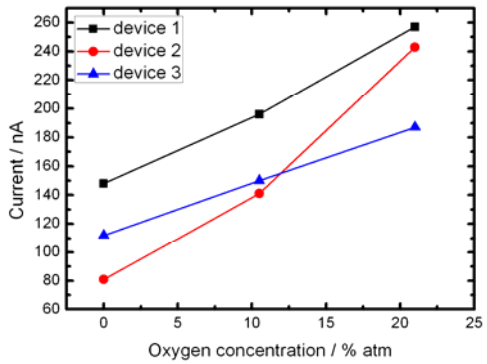

Figure 8.12: Current values from 3 devices at -0.6 V obtained in BBS with three different oxygen concentration levels.

capacitance and faradaic side-reactions. The currents obtained in air-equilibrated BBS are significantly different from those obtained in oxygen-depleted BBS ($p<0.0001$). These results indicate that the device has the potential to be used in low-level oxygen monitoring. We have also observed that, for PCM-based dissolved oxygen sensors, measurements based on PSC technique have much larger hysteresis in terms of response to oxygen concentration change.

The next measurement is to evaluate device linearity and sensitivity. Measurements were carried out on 10 devices at 3 different oxygen levels (Figure 8.11). Figure 8.12 shows the data for 3 of the devices. For each device, the current/oxygen-concentration has a linear relationship as expected. The Pearson product-moment correlation coefficient is calculated for each device and the average is found to be 0.996. One problem reflected in Figure 8.12 is device-to-device variation. Since single device has shown good linearity, we propose that a two-point calibration will be sufficient for each device prior to use. The sensitivity is determined to be 4.7±1.8 nA/(% atm oxygen). Another important parameter of a sensor is its resolution. As we have discussed, the readings of a single device have approximately 5% fluctuations in long term tests. The average reading taken from 10 devices in air-equilibrated BBS is 247 nA (see previous

discussion). The average sensitivity is 4.7 nA/(% atm oxygen). Thus, the resolution of the device is roughly equal to 5%×(247nA)/(4.7nA/(% atm oxygen)) = 2.6 % atm oxygen.

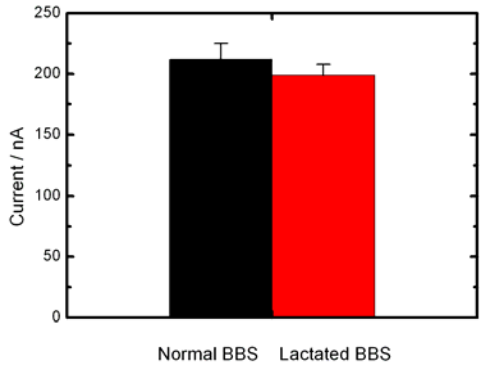

Figure 8.13: Current values at -0.6 V obtained in normal/lactated BBS.

The potential values of these devices for in vivo use were further examined by looking at their in vitro performances in simulated body environment. One important shortcoming of experimentation in out-of-body BBS is the lack of physiological responses. For example, when ischemia occurs (near zero oxygen concentration), the contents of the local body fluid change slightly and unknown small electroactive molecules might be produced and accumulate transiently in the body fluid. Despite the fact that these molecules should only be present at very low concentrations, it is possible that they can interfere with the oxygen sensing process by one way or another. It is well-known that lactate is the most abundantly produced molecules during ischemia. As a preliminary study, we compared the responses of the device in air-equilibrated BBS and lactated air-equilibrated BBS. Specifically, BBS containing 10 mM sodium lactate was prepared by adding sodium lactate to the medium. The device was alternatively immersed in normal BBS and lactated BBS and was thoroughly rinsed by DI water when transferred from lactated BBS to normal BBS. LSV measurements were carried out and the current values at -0.6

V are used to quantify the results. The statistics reveal that there is no significant difference between measurements obtained in the two media ($p>0.05$) (Figure 8.13).

APPENDIX A

SOME MATHEMATICAL DETAILS REGARDING CHAPTER 3

Denote the eigenvalue of matrix (3.19) as z. For any given z, we can obtain two solutions with two k values with opposite signs. A parity operation which takes x into $-x$ can transform one solution into the other. Therefore, the two k values with opposite signs give physically equivalent solutions (mirror solutions with respect to the origin). Matrix (3.19) is a 2×2 matrix and has two eigenvalues. Thus there are at most two physically different solutions. To prove that there is at least one physically allowed solution, we begin with the characteristic equation of matrix (3.19) (which the eigenvalue z must satisfy),

$$z^2-\left\{\omega^2\rho_{f0}\beta_f+\frac{\omega^2\rho_s}{K_v}+i\left[\omega\phi_0\Phi_0\beta_f+\frac{\omega\phi_0\Phi_0}{K_v\left(1-\phi_0\right)}\right]\right\}z+\omega^2\rho_{f0}\beta_f\left[\frac{\omega^2\rho_s}{K_v}+\frac{i\omega\phi_0\Phi_0}{K_v\left(1-\phi_0\right)}\right]=0 \quad \text{(A1)}$$

Denote the two roots by z_1 and z_2 and apply Viete's formulas to equation (A1),

$$z_1+z_2=\omega^2\rho_{f0}\beta_f+\frac{\omega^2\rho_s}{K_v}+i\left[\omega\phi_0\Phi_0\beta_f+\frac{\omega\phi_0\Phi_0}{K_v\left(1-\phi_0\right)}\right] \quad \text{(A2)}$$

This implies that $\operatorname{Im}z_1+\operatorname{Im}z_2=\operatorname{Im}\left(z_1+z_2\right)=\omega\phi_0\Phi_0\beta_f+\frac{\omega\phi_0\Phi_0}{K_v\left(1-\phi_0\right)}>0$.

Therefore, either $\mathrm{Im}z_1$ or $\mathrm{Im}z_2$ has to be greater than zero. Without loss of generality, we assume $\mathrm{Im}z_1>0$. Then $k_1=z_1^{1/2}$ is a complex number falling into the 1st quadrant of the complex plane and represents a wave propagating along and decaying in the $+x$ direction ($k_1=-z_1^{1/2}$ is a complex number falling into the 3rd quadrant of the complex plane and represents a wave propagating along and decaying in the $-x$ direction, which is the mirror solution of $k_1=z_1^{1/2}$).

APPENDIX B

SOME MATHEMATICAL DETAILS REGARDING CHAPTER 4

In this appendix, we present a detailed derivation of the third term on the right hand side of equation (4.3), which is a source term representing drug transport across the capillary walls. Establish a Cartesian coordinate system such that the x direction is perpendicular to the capillary wall and is pointing from the inside of the vessel to the outside of the vessel. Since we are dealing with a local problem, we can assume translational invariance in the y and z direction and reduce the problem to 1-D. Assume the inner surface of the capillary wall is located at $x = 0$ and the outer surface at $x = L$. The capillary wall is modeled as a rigid porous medium. Darcy's law, when applied across the capillary wall, is written as

$$v_p = L_p\left(p_0 - p_i\right) \quad \text{(B1)}$$

where v_p is the fluid velocity across the capillary wall.

Mass conservation in the capillary wall is written as

$$\frac{\partial c_p}{\partial t} + \frac{\partial}{\partial x}\left(-D_p\frac{\partial c_p}{\partial x} + \left(1-\sigma\right)c_p v_p\right) = 0 \quad \text{(B2)}$$

where c_p is the drug concentration within the capillary wall, and D_p is the drug diffusion coefficient within the capillary wall.

Since mass transfer across the capillary wall is very slow, we apply the quasi-steady-state approximation and reduce equation (B2) to

$$\frac{\partial}{\partial x}\left(-D_p\frac{\partial c_p}{\partial x} + \left(1-\sigma\right)c_p v_p\right) = 0 \quad \text{(B3)}$$

The solution of equation (B3) subject to the boundary conditions of $c_p\big|_{x=0} = c_0$ and $c_p\big|_{x=L} = c$ is

$$c_p = \frac{c_0 e^{Pe_{mv}} - c}{e^{Pe_{mv}} - 1} - \frac{c_0 - c}{e^{Pe_{mv}} - 1} e^{Pe_{mv}\frac{x}{L}} \quad \text{(B4)}$$

where $Pe_{mv} = \dfrac{(1-\sigma) v_p L}{D_p}$ and by definition $D_p = pL$. Using equation (B1), we have

$Pe_{mv} = \dfrac{L_p (p_0 - p_i)(1-\sigma)}{p}$, which is identical to equation (4.4).

Under the quasi-steady-state approximation, the drug flux J_p across a single capillary wall is independent of x and is given by

$$J_p = -D_p \frac{\partial c_p}{\partial x} + (1-\sigma) c_p v_p = \frac{L_p (p_0 - p_i)(1-\sigma)\left(c_0 e^{Pe_{mv}} - c\right)}{e^{Pe_{mv}} - 1} \quad \text{(B5)}$$

Therefore the drug source term in equation (4.3) representing drug transport across the capillary walls per unit tissue volume should be sJ_p.

REFERENCES

Anderson, J.L., Quinn, J.A., 1974. Restricted transport in small pores. Biophys. J. 14, 130-150.

Althoff, M., Acker, H., 1985. The influence of carotid body stimulation on oxygen tension and microcirculation of various organs of the cat. Znt. J. Microcirc: Clin. Exp 4, 379-395.

Atlas, S.W., Mark, A.S., Grossman, R.I., Gomori, J.M., 1988. Intracranial hemorrhage: gradient-echo MR imaging at 1.5 T. Comparison with spin-echo imaging and clinical applications. Radiology 168, 803-807.

Bard, A.J., Faulkner, L.R., 2001. Electrochemical Methods. John Wiley & Sons, Inc., New Jersey.

Basser, P., 1992. Interstitial pressure, volume, and flow during infusion into brain tissue. Microvasc. Res. 44, 143-165.

Baumgartl, H., Lubbers, D.W., 1983. Microcoaxial needle sensor for polarographic measurement of local O_2 pressure in the cellular range of living tissue. Its construction and properties. 'Polarographic Oxygen Sensors', ed. Gnaiger, Forstner, Chap. 1.4. Springer Verlag, Berlin, 37-65.

Baxter, L.T., Jain, R.K., 1989. Transport of fluid and macromolecules in tumors: I. role of interstitial pressure and convection. Microvasc. Res. 37, 77-104.

Bear, J., 1972. Dynamics of fluids in porous media. American Elsevier Publishing Company, Inc..

Bilston, L.E., Fletcher, D.F., Brodbelt, A.R., Stoodley, M.A., 2003. Arterial pulsation-driven cerebrospinal fluid flow in the perivascular space: a computational model. Comput. Meth. Biomech. Biomed. Eng. 6 (4), 235-241.

Biot, M., 1956a. Theory of propagation of elastic waves in a fluid-saturated porous solid. I. Low

frequency range. J. Acoust. Soc. Am. 28, 168-178.

Biot, M., 1956b. Theory of propagation of elastic waves in a fluid-saturated porous solid. II. Higher frequency range. J. Acoust. Soc. Am. 28, 179-191.

Bloomfield, I.G., 1998. Effects of proteins, blood cells and glucose on the viscosity of cerebrospinal fluid. Pediatric Neurosurg. 28 (5), 246-251.

Bobo, R.H., Laske, D.W., Akbasak, A., Morrison, P.F., Dedrick, R.L., Oldfield, E.H., 1994. Convection-enhanced delivery of macromolecules in the brain. PNAS 91, 2076-2080.

Brinkman, H.C., 1947. A calculation of the viscous force exerted by a flowing fluid on a dense swarm of particles. Appl. Sci. Res. A1, 27-34.

Broaddus, W.C., Prabhu, S.S., Gillies, G.T., Neal, J., Conrad, W.S., Chen, Z.J., 1998. Distribution and stability of antisense phosphorothioate oligonucleotides in rodent brain following direct intraparenchymal controlled-rate infusion. J. Neurosurg. 88, 734–742.

Bullock, R., Mendelow, A.D., Teasdale, G.M., Graham, D.I., 1984. Intracranial hemorrhage induced at arterial pressure in the rat. Neurol. Res. 6, 184-188.

Chen, J.K., Wise, K.D., Hetke, J.F., Bledsoe, S.C., 1997. A multichannel neural probe for selective chemical delivery at the cellular level. IEEE Trans. Biomed. Eng. 44 (8), 760–769.

Chen, M.Y., Lonser, R.R., Morrison, P.F.,, Governale, L.S., Olfield, E.H., 1999. Variables affecting convection-enhanced delivery to the striatum: a systematic examination of rate of infusion, cannula size, infusate concentration, and tissue-cannula sealing time. J. Neurosurg. 90, 315-320.

Chen, Z., Gillies, G.T., Broaddus, W.C., Prabhu, S.S., Fillmore, H., Mitchell, R.M., Corwin, F.D., Fatouros, P.P., 2004. A realistic brain tissue phantom for intraparenchymal infusion studies. J. Neurosurg. 101, 314–322.

Chen, M.Y., Hoffer, A., Morrison, P.F., Hamilton, J.F., Hughes, J., Schlageter, K.S., Lee, J., Kelly, B.R., Oldfield, E.H., 2005. Surface properties, more than size, limiting convective distribution of virus-sized particles and viruses in the central nervous system. J. Neurosurg. 103, 311-319.

Deen, W.M., 1998. Analysis of transport phenomena. Oxford University Press.

DiResta, G.R., Lee, J., Healey, J.H., Levchnko, A., Larson, S.M., Arbit, E., 2000. Artificial lymphatic system: a new approach to reduce interstitial hypertension and increase blood flow, pH and pO_2 in solid tumors. Ann. Biomed. Eng. 28, 543-555.

Driessen, G.K., Scheidt-Bleichert, H., Sobota, A., Inhoffen, W., Heidtmann, H., Haest, C.W., Kamp, D., Schmid-Schonbein, H., 1982. Capillary resistance to flow of hardened (diamide treated) red blood cells (RBC). Pflugers Arch. 392, 261-267.

Edelman, I., 1999. Wave dynamics of saturated porous media and evolutionary equations. Transport Porous Med. 34, 117–128.

Elwassif, M.M., Kong, Q., Vazquez, M. , Bikson, M., 2006. Bio-heat transfer model of deep brain stimulation-induced temperature changes. J. Neural Eng. 3, 306-315.

Fazekas, F., Kleinert, R., Roob, G., Kleinert, G., Kapeller, P., Schmidt, R., Hartung, H.P., 1999. Histopathologic analysis of foci of signal loss on gradient-echo T2*-weighted MR images in patients with spontaneous intracerebral hemorrhage: evidence of microangiopathy-related microbleeds. AJNR Am. J. Heuroradiol. 20, 637-642.

Feigin, V.L., 2005. Stroke epidemiology in the developing world. Lancet 365, 2160-2161.

Fenstermacher, J.D., Patlak, C.S., Blasberg, R.G., 1974. Transport of material between brain extracellular fluid, brain cells and blood. Fed. Proc. 33, 2070–2074.

Filler, A.G., 2010. The history, development, and impact of computed imaging in neurological diagnosis and neurosurgery: CT, MRI, DTI. Internet J. Neurosurg. 7, 1-1.

Fine, R., Millero, F., 1973. Compressibility of water as a function of temperature and pressure. J. Chem. Phys. 59, 5529-5536.

Foley, C.P., 2009. Neural drug delivery: novel microfluidic delivery devices and studies of transport phenomena. PhD. Dissertation, Cornell University.

Fung, Y., 1981. Biomechanics. Springer.

Gierke, T.D., Hsu, W.S., 1982. The cluster-network model of ion clustering in perfluorosulfonated membranes. 'Perflnorinated lonomer Membranes', ed. Eisenberg A, Yeager HL, ACS Symp. Ser. 180, American Chemical Society, Washington, DC, 283-307.

Gladdish, S., Dulka, M., Winston, B., James, C., Christopher, J., Chakravarthi, R., 2005. Repeatability of non-invasive measurement of intracerebral pulse wave velocity using transcranial Doppler. Clinical Science 108, 433–439.

Groothuis, D.R., Ward, S., Itskovich, A.C., Dobrescu, C., Allen, C.V., Dills, C., 1999. Comparison of 14C-sucrose delivery to the brain by intravenous, intraventricular, and convection-enhanced intracerebral infusion. J. Neurosurg. 90, 321–331.

Groothuis, D.R., Benalcazar, H., Allen, C.V., Wise, R.M., Dills, C., Dobrescu, C., Rothholtz, V., Levy, R.M., 2000. Comparison of cytosine arabinoside delivery to rat brain by intravenous, intrathecal, intraventricular and intraparenchymal routes of administration. Brain Res. 856(1-2), 281–290.

Groothuis, D.R., Vavra, M.W., Schlageter, K.E., Wang, E.W-Y., Itskovich, A.C., Hertzler, S., Allen, C.V., Lipton, H.L., 2007. Efflux of drugs and solutes from brain: the interactive roles of diffusional transcapillary transport, bulk flow and capillary transporters. J. Cereb. Blood Flow Metab. 27, 43–56.

Guerin, C., Olivi, A., Weingart, J.D., Lawson, H.C., Brem, H., 2004. Recent advances in brain

tumor therapy: local intracerebral drug delivery by polymers. Invest. New Drugs 22, 27-37.

Hadaczek, P., Yamashita, Y., Mirek, H., Tamas, L., Bohn, M. C., Noble, C., Park, J. W., Bankiewicz, K., 2006. The 'perivascular pump' driven by arterial pulsation is a powerful mechanism for the distribution of therapeutic molecules within the brain. Molecular Therapy 14 (1), 69-78.

Haller, M.F., Saltzman, W.M., 1998. Localized delivery of proteins in the brain: can transport be customized? Pharm. Res. 15(3), 377–385.

Haller, S., Bartsch, A., Nguyen, D., Rodriguez, C., Emch, J., Gold, G., Lovglad, K.O., Giannakopoulos, P., 2010. Cerebral microhemorrhage and iron deposition in mild cognitive impairment: susceptibility-weighted MR imaging assessment. Radiology 257, 764-773.

Hamilton, J.F., Morrison, P.F., Chen, M.Y., Harvey-White, J., Pernaute, R.S., Phillips, H., Oldfield, E., Bankiewicz, K.S., 2001. Heparin coinfusion during convection-enhanced delivery (CED) increases the distribution of the glial-derived neurotrophic factor (GDNF) ligand family in rat striatum and enhances the pharmacological activity of neurturin. Exp. Neurol. 168(1), 155–161.

Happel, J., 1973. Low Reynolds number hydrodynamics. Noordhoff International Publishing.

Hoeks, A.P.G., Brands, P.J., Willigers, J.M., Reneman, R.S., 1999. Non-invasive measurement of mechanical properties of arteries in health and disease. P. I. Mech. Eng. 213 (Part H), 195-202.

Huynh, G.H., Ozawa, T., Deen, D.F., Tihan, T., Szoka Jr., F.C., 2007. Retro-convection enhanced delivery to increase blood to brain transfer of macromolecules. Brain Res. 1128, 181-190.

Ichimura, T., Fraser, P.A., Cserr, H.F., 1991. Distribution of extracellular tracers in perivascular spaces of the rat brain. Brain Res. 545, 103-113.

Iida, S., baumbach, G.L., Lavoie, J.L., Faraci, F.M., Sigmund, C.D., Heistad, D.D., 2005. Spontaneous stroke in a genetic model of hypertension in mice. Stroke 36, 1253-1258.

Jaffrin, M.Y., Shapiro, A.H., 1971. Peristaltic pumping. Annu. Rev. Fluid Mech. 3, 13-37.

Jobst, G., Urban, G., Jachimowicz, A., Kohl, F., Tilado, O., 1993. Thin-film Clark-type oxygen sensor based on novel polymer membrane systems for in vivo and biosensor applications. Biosens Bioelectron 8, 123-128.

Kasem, K.K., Jones, S., 2008. Platinum as a reference electrode in electrochemical measurements. Platinum Metals Review 52, 100-106.

Koudelka, M., 1986. Performance characteristics of a planar Clark-type oxygen electrode. Sens. Actuators 9, 249-258.

Kunwar, S., Prados, M.D., Chang, S.M., Berger, M.S., Lang, F.F., Piepmeier, J.M., Sampson, J.H., Ram, Z., Gutin, P.H., Gibbons, R.D., Aldape, K.D., Croteau, D.J., Sherman, J.W., Puri, R.K., Group, C.B.I.S., 2007. Direct intracerebral delivery of cintredekin besudotox (IL13-PE38QQR) in recurrent malignant glioma: a report by the Cintredekin Besudotox Intraparenchymal Study Group. J. Clin. Oncol. 25(7), 837–844.

Laske, D.W., Morrison, P.F., Lieberman, D.M., Corthesy, M.E., Reynolds, J.C., Stewart-Henney, P.A., 1997. Chronic interstitial infusion of protein to primate brain: determination of drug distribution and clearance with single-photon emission computerized tomography imaging. J. Neurosurg. 87, 586–594.

Lewis Jr., G., Olbricht, W.L., Lewis Sr., G., 2007. Acoustic enhanced evans blue dye perfusion in neurological tissues. J. Acoust. Soc. Am. 122, 3007-3014.

Lewis Jr., G., Wang, P., Lewis Sr., G., Olbricht, W.L., 2009. Ultrasound enhanced drug delivery

to soft animal tissues. AIP. Conf. Proc. 1113, 403-407.

Lidar, Z., Mardor, Y., Jonas, T., Pfeffer, R., Faibel, M., Nass, D., Hadani, M., Ram, Z., 2004. Convection-enhanced delivery of paclitaxel for the treatment of recurrent malignant glioma: a phase I/II clinical study. J. Neurosurg. 100(3), 472–479.

Lieberman, D.M., Laske, D.W., Morrison, P.F., Bankiewicz, K.S., Oldfield, E.H., 1995. Convection-enhanced distribution of large molecules in gray matter during interstitial drug infusion. J. Neurosurg. 82(6), 1021–1029.

Lightfoot, E.N., 1973. Transport phenomena and living systems. Wiley, New York.

Lippert, S.A., Rang, E.M., Grimm, M.J., 2004. The high frequency properties of brain tissue. J. Biorheol 41, 681-691.

Lonser, R.R., Corthesy, M.E., Morrison, P.F., Gogate, N., Oldfield, E.H., 1999. Convection-enhanced selective excitotoxic ablation of the neurons of the globus pallidus internus for treatment of parkinsonism in nonhuman primates. J. Neurosurg. 91(2), 294–302.

Lonser, R.R., Walbridge, S., Garmestani, K., Butman, J.A., Walters, H.A., Vortmeyer, A.O., Morrison, P.F., Brechbiel, M.W., Oldfield, E.H., 2002. Successful and safe perfusion of the primate brainstem: in vivo magnetic resonance imaging of macromolecular distribution during infusion. J. Neurosurg. 97(4), 905–913.

MacLellan, C.L., Silasi, G., Auriat, A.M., Colbourne, F., 2010. Rodent models of intracerebral hemorrhage. Stroke 41, S95-S98.

Mannes, A.J., Caudle, R.M., O'Connell, B.C., Iadarola, M.J., 1998. Adenoviral gene transfer to spinal-cord neurons: intrathecal vs. intraparenchymal administration. Brain Res. 793, 1–6.

Mardor, Y., Roth, Y., Lidar, Z., Jonas, T., Pfeffer, R., Maier, S.E., Faibel, M., Nass, D., Hadani, M., Orenstein, A., Cohen, J.S., Ram, Z., 2001. Monitoring response to convection-

enhanced Taxol delivery in brain tumor patients using diffusion-weighted magnetic resonance imaging. Cancer Res. 61(13), 4971–4973.

Mascini, M., Memoli, A., 1986. Comparison of microbial sensors based on amperometric and potentiometric electrodes. Anal. Chim. Acta. 182, 113-122.

McKean, B.D., Gough, D.A., 1988. A telemetryinstallation system for chronically implanted glucose and oxygen sensors. IEEE Trans. Biomed. Eng. 35(7), 526-532.

McLaughlin, G.W., Braden, K., Franc, B., Kovacs, G.T.A., 2002. Microfabricated solid-state dissolved oxygen sensor. Sens. Actuators B 83, 138-148.

Mishra, M., Rao, A.R., 2004. Peristaltic transport in a channel with a porous peripheral layer: model of a flow in gastrointestinal tract. J. Biomech. 38, 779-789.

Morrison, P.F., Laske, D.W., Bobo, H., Oldfield, E.H, Dedrick, R.L., 1994. Highflow microinfusion: tissue penetration and pharmacodynamics. Am. J. Physiol. Regul. Integr. Comp. Physiol. 266, R292-R305.

Morrison, P.F., Chen, M.Y., Chadwick, R.S., Lonser, R.R., Oldfield, E.H., 1999. Focal delivery during direct infusion to brain: role of flow rate, catheter diameter, and tissue mechanics. Am. J. Physiol. Regul. Integr. Comp. Physiol. 277 (4), R1218–R1229.

Morrison, P., 2001. Distribution models of drug kinetics. In: Atkinson, A.J.J., Daniels, C.E., Dedrick, R.L. (Eds.), Principles of Clinical Pharmacology. Academic Press, San Diego, pp. 93–112.

Muldoon, L.L., Nilaver, G., Kroll, R.A., Pagel, M.A., Breakefield, X.O., Chiocca, E.A., 1995. Comparison of intracerebral inoculation and osmotic blood-brain barrier disruption for delivery of adenovirus, herpesvirus, and iron oxide particles to normal rat brain. Am. J. Pathol. 147, 1840–1851.

Nanjo, M., Giulbault, G.G., 1974. Enzyme electrodes for L-amino acids and glucose. Anal. Chim. Acta 73, 367-373.

Neeves, K.B., Lo, C.T., Foley, C.P., Saltzman, W.M., Olbricht, W.L., 2006. Fabrication and characterization of microfluidic probes for convection enhanced drug delivery. J. Control Release 111, 252–262.

Neeves, K.B., Sawyer, A.J., Foley, C.P., Saltzman, W.M., Olbricht, W.L., 2007. Dilation and degradation of the brain extracellular matrix enhances penetration of infused polymer nanoparticles. Brain Res. 1180, 121-132.

Netti, P.A., Baxter, L.T., Boucher, Y., Skalak, R., Jain, R.K., 1997. Macro- and microscopic fluid transport in living tissues: application to solid tumors. AIChE J. 43, 818-834.

Netti, P.A., Travascio, F., Jain, R.K., 2003. Coupled macromolecular transport and gel mechanics: poroviscoelastic approach. AIChE J. 43, 1580-1596.

Nield, D., Bejan, A., 1998. Convection in Porous Media. Springer.

Nozomi, N., Schaffer, C.B., Friedman, B.,Lyden, P.D., Kleinfeld, D., 2007. Penetrating arterioles are a bottleneck in the perfusion of neocortex. PNAS USA 104, 365-370.

Offenbacher, H., Fazekas, F., Schmidt, R., Koch, M., Fazekas, G., Kapeller, P., 1974. MR of cerebral abnormalities concomitant with primary intracerebral hematomas. AJNR Am. J. Neurodadiol. 17, 573-578.

Oldendorf, W.H., 1974. Lipid solubility and drug penetration of the blood brain barrier. Proc. Soc. Exp. Biol. Med. 147, 813–815.

Provost, A.M., Schwarz, W.H., 1994. A theoretical study of viscous effects in peristaltic pumping. J. Fluid Mech. 279, 177-195.

Rapoport, S.I., 2000. Osmotic opening of the blood–brain barrier: principles, mechanism, and therapeutic applications. Cell. Mol. Neurobiol. 20, 217-230.

Ren, H., Boulikas, T., Lundstrom, K., Soling, A., Warnke, P.C., Rainov, N.G., 2003. Immunogene therapy of recurrent glioblastoma multiforme with a liposomally encapsulated replication-incompetent Semliki Forest virus vector carrying the human interleukin-12 gene—a phase I/II clinical protocol. J. Neurooncol. 64, 147–154.

Rosenberg, G.A., Mun-Bryce, S., Wesley, M., Kornfeld, M., 1990. Collagenase-induced intracerebral hemorrhage in rats. Stroke 21, 801-807.

Retterer, S.T., Smith, K.L., Bjornsson, C.S., Neeves, K.B., Spence, A.J., Turner, J.N., Shain, W., Isaacson, M.S., 2004. Model neural prostheses with integrated microfluidics: a potential intervention strategy for controlling reactive cell and tissue responses. IEEE Trans. Biomed. Eng. 51 (11), 2063–2073.

Saltzman, W.M., Radomsky, M.L., 1991. Drugs released from polymers: diffusion and elimination in brain tissue. Chem. Eng. Sci. 46, 2429-2444.

Sampson, J.H., Akabani, G., Archer, G.E., Bigner, D.D., Berger, M.S., Friedman, A.H., Friedman, H.S., Herndon, J.E., Kunwar, S., Marcus, S., McLendon, R.E., Paolino, A., Penne, K., Provenzale, J., Quinn, J., Reardon, D.A., Rich, J., Stenzel, T., Tourt-Uhlig, S., Wikstrand, C., Wong, T., Williams, R., Yuan, F., Zalutsky, M.R., Pastan, I., 2003. Progress report of a Phase I study of the intracerebral microinfusion of a recombinant chimeric protein composed of transforming growth factor (TGF)-alpha and a mutated form of the Pseudomonas exotoxin termed PE-38 (TP-38) for the treatment of malignant brain tumors. J. Neurooncol. 65(1), 27–35.

Sarntinoranont, M., Banerjee, R.K., Lonser, R.R., Morrison, P.F., 2003. A computational model of direct interstitial infusion of macromolecules into the spinal cord. Ann Biomed Eng 31, 448–461.

Sarntinoranont, M., Chen, X., Zhao, J., Mareci, T.H., 2006. Computational model of interstitial

transport in the spinal cord using diffusion tensor imaging. Ann Biomed Eng 34, 1304-1321.

Schley, D., Carare-Nnadi, R., Please, C.P., Perry, V.H., Weller, R.O., 2006. Mechanisms to explain the reverse perivascular transport of solutes out of the brain. J. Theor Biol 238, 962–974.

Shapiro, A.H., Jaffrin, M.Y., Weinberg, S.L., 1969. Peristaltic pumping with long wavelengths at low Reynolds number. J. Fluid Mech. 37 (4), 799-825.

Shih, J., Xie, J., Tai, Y., 2003. Surface micromachined and integrated capacitive sensors for microfluidic applications. In Proceedings of the 12th International Conference on Solid-State Sensors, Actuators, and Microsystems. Boston, USA, 388-391.

Smith, J.H., Humphrey, J.A.C., 2007. Interstitial transport and transvascular fluid exchange during infusion into brain and tumor tissue. Microvasc Res 73, 58-73.

Suzuki, H., Arakawa, H., Karube, I., 2001. Fabrication of a sensing module using micromachined bioelectrodes. Biosens. Bioelectron. 16, 725-733.

Suzuki, H., Hirakawa, T., Sasaki, S., Karube, I., 2000. An integrated module for sensing pO_2, pCO_2, and pH. Anal. Chim. Acta 405, 57-65.

Suzuki, H., Hirakawa, T., Watanabe, I., Kikuchi, Y., 2001. Determination of blood pO_2 using a micomachined Clark-type oxygen electrode. Anal. Chim. Acta 431, 249-259.

Suzuki, H., Kojima, N., Sugama, A., Takei, F., 1990. Development of a miniature Clark-type oxygen electrode using semiconductor techniques and its improvement for practical applications. Sens. Actuators B 2, 185-190.

Suzuki, H., Kojima, N., Sugama, A., Takei, F., Ikegami, K., 1990. Disposable oxygen electrodes fabricated by semiconductor techniques and their application to bioelectrodes. Sens. Actuators B 1, 528-532.

Suzuki, H., Ozawa, H., Sasaki, S., Karube, I., 1998. A novel thin-film Ag/AgCl anode structure for microfabricated Clark-type oxygen electrodes. Sens. Actuators B 54, 140-147.

Suzuki, H., Sugama, A., Kojima, N., 1993. Micromachined Clark oxygen electrode. Sensor Actuat B 10, 91-98.

Suzuki, H., Sugama, A., Kojima, N., Takei, F., Ikegami, K., 1991. A miniature Clark-type oxygen electrode using a polyelectrolyte and its application as a glucose sensor. Biosens Bioelectron 6, 395-400.

Suzuki, H., Sugama, A., Kojima, N., 1990. Miniature Clark-type oxygen electrode with a three-electrode configuration. Sens. Actuators B 2, 297-303.

Suzuki, H., Tamiya, E., Karube, I., 1988. Fabrication of an oxygen electrode using semiconductor technology. Anal. Chem. 60, 1078-1080.

Thorne, R., Nicholson, C., 2006. In vivo diffusion analysis with quantum dots and dextrans predicts the width of brain extracellular space. Proc. Natl. Acad. Sci. 103, 5567-5572

Worgall, S., Sondhi, D., Hackett, N.R., Kosofsky, B., Kekatpure, M.V., Neyzi, N., Dyke, J.P., Ballon, D., Heier, L., Greenwald, B.M., Christos, P., Mazumdar, M., Souweidane, M.M., Kaplitt, M.G., Crystal, R.G., 2008. Treatment of late infantile neuronal ceroid lipofuscinosis by CNS administration of a serotype 2 adeno-associated virus expressing CLN2 cDNA. Hum. Gene Ther. 19(5), 463–474.

Weber, F., Asher, A., Bucholz, R., Berger, M., Prados, M., Chang, S., Bruce, J., Hall, W., Rainov, N.G., Westphal, M., Warnick, R.E., Rand, R.W., Floeth, F., Rommel, F., Pan, H., Hingorani, V. N., Puri, R.K., 2003. Safety, tolerability, and tumor response of IL4-Pseudomonas exotoxin (NBI-3001) in patients with recurrent malignant glioma. J. Neurooncol. 64(1-2), 125–137.

Whalen, W.J., Riley, J., Nair, P., 1967. A microelectrode for measuring intracellular pO_2. J.

Appl. Physiol. 23, 798-801.

Wu, C.C., Yasukawa, T., Shiku, H., Matsue, T., 2005. Fabrication of miniature Clark oxygen sensor integrated with microstructure. Sensor Actuat B 110, 342-349.

Yadav, Y.R., Mukerji, G., Shenoy, R., Bassoor, A., Jain, R., Nelson, A., 2007. Endoscopic management of hypertensive intraventricular hemorrhage with obstructive hydrocephalus. BMC Neurology 7, 1-9.

Yang, W., Barth, R.F., Adams, D.M., Ciesielski, M.J., Fenstermaker, R.A., Shukla, S., Tjarks, W., Caligiuri, M.A. Convection-enhanced delivery of boronated epidermal growth factor for molecular targeting of EGF receptor-positive gliomas. Cancer Res. 62(22), 6552–6558.

Yang, Z., Sasaki, S., Karube, I., Suzuki, H., 1997. Fabrication of oxygen electrode arrays and their incorporation into electrodes for measuring biochemical oxygen demand. Anal. Chim. Acta 357, 41-49.

Zahn, J.D., Talbot, N.H., Liepmann, D., Pisano, A.P., 2000. Microfabricated polysilicon microneedles for minimally invasive biomedical devices. Biomed. Microdevices 2 (4), 295–303.

Zwillinger, D., 1997. Handbook of differential equations. Academic Press.